Master's thesis

NTNU
Norwegian University of Science and Technology
Faculty of Engineering
Department of Marine Technology

Hermann Tomasgaard

Evaluation of three different foil-strut junction designs for a hydrofoil vessel

Master's thesis in Marine Technology
Supervisor: Professor Sverre Steen
Co-supervisor: Jarle Vinje Kramer
June 2023

NTNU
Norwegian University of
Science and Technology

Hermann Tomasgaard

Evaluation of three different foil-strut junction designs for a hydrofoil vessel

Master's thesis in Marine Technology
Supervisor: Professor Sverre Steen
Co-supervisor: Jarle Vinje Kramer
June 2023

Norwegian University of Science and Technology
Faculty of Engineering
Department of Marine Technology

NTNU
Norwegian University of
Science and Technology

NTNU Trondheim
Norwegian University of Science and Technology
Department of Marine Technology

MASTER THESIS IN MARINE TECHNOLOGY

SPRING 2023

FOR

Hermann Sogn Tomasgaard

Evaluation of three different foil-strut junction designs for a hydrofoil vessel

Hydrofoil vessels are again attractive for high-speed ships, due to their potential for superior seakeeping and low drag. A critical component of the foil system of a foil boat is the junction between the vertical strut, penetrating the free water surface, and the horizontal hydrofoil. Challenges are related to drag, caused by partial flow separation, caused by the merging of the boundary layers of strut and foil, ventilation of the foil by the strut, as well as cavitation.

The master will be performed in co-operation with Lift Ocean.

The three designs to be evaluated in the project will be made by Lift Ocean, in discussion with the candidate

RANS CFD is an increasingly attractive tool for evaluating the hydrodynamic characteristics, also of foil systems. Thus, it is initially selected as the main tool for the evaluation in this work.

The goal of the master thesis is to evaluate the hydrodynamic performance of the three foil-strut-junction designs, considering the drag and cavitation inception as the primary performance indices.

Since the occurrence of flow separation is a critical aspect of the hydrodynamic performance in this case, selection of turbulence model is expected to be important. Thus, a thorough investigation, leading up to choice of turbulence model for the evaluations, is expected.

In order to ensure the correctness of the simulations, a CFD study should include a validation study. A comprehensive validation study is expected as part pf this project, under the limitation of available existing validation data, as no new experiments are expected as part of this project.

In the thesis the candidate shall present his personal contribution to the resolution of problem within the scope of the thesis work.

Theories and conclusions shall be based on mathematical derivations and/or logic reasoning identifying the various steps in the deduction.

The thesis work shall be based on the current state of knowledge in the field of study. The current state of knowledge shall be established through a thorough literature study, the results of this study shall be written into the thesis. The candidate should utilize the existing possibilities for obtaining relevant literature.

The thesis shall be organized in a rational manner to give a clear exposition of results, assessments, and conclusions. The text should be brief and to the point, with a clear language. Telegraphic language should be avoided.

NTNU Trondheim
Norwegian University of Science and Technology
Department of Marine Technology

The thesis shall contain the following elements: A text defining the scope, preface, list of contents, summary, main body of thesis, conclusions with recommendations for further work, list of symbols and acronyms, reference and (optional) appendices. All figures, tables and equations shall be numerated.

The supervisor may require that the candidate, in an early stage of the work, present a written plan for the completion of the work. The plan shall include a budget for the use of laboratory or other resources that will be charged to the department. Overruns shall be reported to the supervisor.

The original contribution of the candidate and material taken from other sources shall be clearly defined. Work from other sources shall be properly referenced using an acknowledged referencing system.

The thesis shall be submitted electronically (pdf) in Inspera:

- Signed by the candidate
- The text defining the scope (this text) (signed by the supervisor) included

Supervisor : Professor Sverre Steen
Advisors : Jarle Vinje Kramer
Start : 15.01.2023
Deadline : 09.06.2023

Trondheim, 15.01.2023

Sverre Steen
Supervisor

Abstract

The strut-hydrofoil junctions play a significant role in contributing to the total drag of hydrofoil systems, particularly due to the interference caused by the meeting boundary layers in the corner. To minimise this interference drag, the design of the junction is of great importance. Therefore, the objective of this study is to evaluate three different designs of the strut-hydrofoil junction through the use of Computational Fluid Dynamics (CFD) simulations in OpenFOAM. The junction designs under analysis include a straight T-junction, a fillet with a rounded corner, and a bulb surrounding the corner.

As part of the study, a thorough validation process is conducted by comparing the simulation results with available experimental data. However, due to the limited experimental data specific to strut-hydrofoil junctions, two cases from the aeronautical industry are selected for validation: a 2D NACA 0012 foil profile and a wing body junction. The simulation results for the 2D NACA 0012 foil profile show acceptable accuracy in terms of lift and drag, with deviations from experimental data typically below 5 percent. Larger discrepancies are seen for the wing body junction where the simulations capture the mean flow features reasonably well, but they struggle to accurately represent the details of the vortex and boundary layer thickness in the corner.

The fillet design demonstrates the highest lift-to-drag ratio. The bulb design exhibits the lowest pressure drag but the highest viscous drag, while the straight T-junction has the highest pressure drag. When considering the likelihood of cavitation inception, the bulb design reduces the minimum pressure coefficient.

There are limitations observed in the CFD simulations of the strut-hydrofoil junctions. Some of the discrepancies identified between the experimental data and CFD results in the validation study are likely to be applicable to the strut-hydrofoil designs as well. The overestimation of corner separation is expected to have a more significant impact on the results of the straight T-junction design compared to the fillet and bulb designs.

In conclusion, despite the mentioned limitations, notable distinctions are observed among the various strut-hydrofoil designs. Consequently, these CFD simulations are regarded as a potential tool for analysing such configurations with a reasonable level of accuracy, while avoiding excessively complex computations. This is particularly applicable to designs where the merging boundary layers do not exert significant effects.

Sammendrag

Selve sammenkoblingen mellom "strut" og "foil" i "hydrofoilen" har stor betydning for den totale motstanden til hydrofoil-systemer. Dette hovedsakelig på grunn av inteferensmotstand som forårsakes av det møtende grensesjiktet i hjørnet. For å minimere denne motstanden får da utformingen av dette hjørnet stor betydning. Formålet med dette studiet er derfor å evaluere tre ulike design av "strut-hydrofoil"- overganger ved hjelp av CFD simuleringer i OpenFOAM. Designene som analyseres er rett hjørne, avrundet hjørne med fillet, og til slutt, en "bulb" som omslutter hjørnet.

Som en del av studiet blir også en grundig valideringsprosess gjennomført. Simulerte resultater sammenlignes med tilgjenglige eksperimentelle data. På grunn av begrenset tilfang av eksperimentelle data spesifike for strut-hydrofoil overganger er to forsøk fra luftfartsindustrien valgt for sammenligning og validering: 2D NACA 0012 vingeprofil og vinge-vegg-overgang. Simuleringene for 2D NACA 0012 vinge profil viser akspetable resultater for løft og motstand, med avvik fra eksperimentelle data på maksimalt 5 prosent. Det er større avvik for vinge-vegg-overgangen der simuleringene relativt godt fanger opp gjennomsnittlige strømningsegenskaper, men feiler m.h.p. detaljer som virvler, og tykkelse på grensesjiktet i hjørnet.

"Fillet"-designet gir det høyeste løft til motstandsforholdet. "Bulb"-designet har lavest trykkmotstand, men høyest viskøs motstand, mens det rette hjørnet har høyest trykkmotstand. Når man vurderer sannsynligheten for kavitasjon, øker bulb designet trykkoeffisienten.

Det er klare begrensninger knyttet til CFD-simuleringene av strut-hydrofoil sammenkoblingene utført i dette studet. Noen av avvikene som identifisert i valideringsstudiet gjelder sannsynligvis også for strut-hydrofoil simuleringene. Overestimeringen av hjørneseparasjon forventes å ha større innvirkning på resultatene for designet med rett hjørne enn for designene med fillet og bulb.

Konklusjonen fra dette studiet viser tydelig at det er klare forskjeller mellom de ulike strut-hydrofoil-designene, til tross for nevnte begrensninger. CFD simuleringer, tilsvarende som gjort her, kan derfor betraktes som et godt egnet, potensielt verktøy for å analysere slike konfigurasjoner med rimelig god nøyaktighet.

Preface

This master's thesis represents the final component of the Master of Science program in Marine Technology, specialising in hydrodynamics, at the Norwegian University of Science and Technology (NTNU). The research was conducted from the fall of 2022 through the spring of 2023, which is one semester longer than usual. This extension was necessary due to the integration of an Olympic campaign in sailing alongside the thesis work. However, officially the master thesis was not taken out before 15. January 2023.

The topic of this thesis was chosen based on interests developed throughout the course of the studies, as well as insights gained during the sailing campaign.

An unpublished preparation project was carried out during the spring of 2022, with some familiarisation with OpenFOAM as well as a thorough literature study of the intended topic for the Master thesis. Large parts of the literature study and theory in this master thesis is based on this work.

None of the sections in this thesis is written by ChatGPT or similar artificial intelligence (AI). However, it is used as inspiration for reformulation of some sentences and sections, in a similar manner to the use of Grammarly (a language specific AI) or other conventional tools for improving the language.

Oslo, 11th June 2023

Hermann Tomasgaard

Acknowledgements

I would like to express my deepest gratitude to the following people who have supported me through the completion of this master's thesis.

First and foremost, would I like express a sincere thanks to my supervisor, Professor Sverre Steen, for his exceptional knowledge and keen attention to detail. I also need to express a thank you for making it possible for me to combine the master thesis with a top sport campaign.

I would also like to extend my heartfelt thanks to my advisor Jarle Vinje Kramer. His clear and thorough explanation of CFD simulations, both in our meetings and through his published articles, have been of utmost importance in shaping this thesis. His guidance has been invaluable.

Additionally I would like to thank Petter Mørland Pedersen, Paolo Motta and Anastasia Zubova in Lift Ocean. Petter for giving me the opportunity to work with Lift Ocean, Paolo for providing me with the strut-hydrofoil designs and Anastasia for very encouraging and good advise regarding CFD analysis.

I would like to acknowledge the department of Marine Technology for providing me we computational resources in order to perform the CFD simulations.

Finally I would like to extend my gratitude to my family and friends for unwavering support and understanding.

Table of Contents

List of Figures

List of Tables

Nomenclature

Abbreviations

2D	Two-dimensional
3D	Three-dimensional
BL	Boundary Layer
CFD	Computational Fluid Dynamics
DNS	Direct Numerical Simulation
EBRSM	Elliptic Blending Reynolds Stress Model
EVM	Linear Eddy-Viscosity Models
IDDES	Improved Delayed Detached Eddy Simulation
LES	Large Eddy Simulation
NLEVM	Non-Linear Eddy-Viscosity Models
NS	Navier-Stokes
NTNU	Norwegian University of Science and Technology
RSM	Reynolds Stress Model

Greek symbols

δ_{ij}	Kronecker delta	$[-]$
μ	Dynamic viscosity	$[\mathrm{kg\,m^{-1}\,s^{-1}}]$
ν	Kinematic viscosity	$[\mathrm{m^2\,s^{-1}}]$
ν_T	Turbulent viscosity	$[\mathrm{m^2\,s^{-1}}]$
ω	Turbulence frequency	$[\mathrm{s^{-1}}]$
ω_m	System rotation vector	

ϕ_{ij}^{*}	Pressure-strain tensor from EBRSM	$[\mathrm{m^2\,s^{-3}}]$
ϕ_{ij}^{h}	Homogeneous pressure-strain tensor	$[\mathrm{m^2\,s^{-3}}]$
ϕ_{ij}^{w}	Near wall pressure-strain tensor	$[\mathrm{m^2\,s^{-3}}]$
ρ	Density	$[\mathrm{kg\,m^{-3}}]$
σ_i	Cavitation number	$[-]$
τ_w	Wall shear stress	$[\mathrm{kg\,s^{-2}\,m^{-1}}]$
ε	Rate of dissipation of turbulent kinetic energy	$[\mathrm{m^2\,s^{-3}}]$
ε_{ij}^{h}	Homogeneous dissipation rate tensor	$[\mathrm{m^2\,s^{-3}}]$
ε_{ij}^{w}	Near wall dissipation rate tensor	$[\mathrm{m^2\,s^{-3}}]$
ε_{ij}	Dissipation tensor	$[\mathrm{m^2\,s^{-3}}]$

Latin symbols

$\mathcal{D}_{ij}^{t}$	Turbulent diffusion tensor from EBRSM	$[\mathrm{m^2\,s^{-3}}]$
$\mathcal{P}_{ij}$	Rate of production of Reynolds stress	$[\mathrm{m^2\,s^{-3}}]$
$\mathcal{R}_{ij}$	Pressure rate of strain tensor	$[\mathrm{m^2\,s^{-3}}]$
$\overline{S_{ij}}$	Mean rate-of-strain tensor	$[\mathrm{m\,s^{-2}}]$
$\overline{U}$	Mean velocity in x-direction	$[\mathrm{m\,s^{-1}}]$
$\overline{V}$	Mean velocity in y-direction	$[\mathrm{m\,s^{-1}}]$
$\overline{W}$	Mean velocity in z-direction	$[\mathrm{m\,s^{-1}}]$
a_{ij}	Anisotropic Reynolds stresses	$[\mathrm{m^2\,s^{-2}}]$
c	Chord length	$[\mathrm{m}]$
C_D	Drag coefficient	$[-]$
C_L	Lift coefficient	$[-]$
C_p	Pressure coefficient	$[-]$
F_D	Drag force	$[\mathrm{N}]$
F_L	Lift force	$[\mathrm{N}]$
g	Gravity acceleration	$[\mathrm{m\,s^{-2}}]$
k	Turbulent kinetic energy	$[\mathrm{m^2\,s^{-2}}]$
p	Pressure	$[\mathrm{N\,m^{-2}}]$

p_a	Atmospheric pressure	$[\mathrm{N\,m^{-2}}]$
p_v	Vapor pressure	$[\mathrm{N\,m^{-2}}]$
s	Span	$[\mathrm{m}]$
T_{kij}	Reynolds stress flux	$[\mathrm{m\,s^{-3}}]$
u	Velocity in x-direction	$[\mathrm{m\,s^{-1}}]$
u'	Fluctuating velocity in x-direction	$[\mathrm{m\,s^{-1}}]$
U^+	Non-dimensional velocity	$[-]$
u_τ	Reference velocity based on wall shear stress	$[\mathrm{m\,s^{-1}}]$
v	Velocity in y-direction	$[\mathrm{m\,s^{-1}}]$
v'	Fluctuating velocity in y-direction	$[\mathrm{m\,s^{-1}}]$
w	Velocity in z-direction	$[\mathrm{m\,s^{-1}}]$
w'	Fluctuating velocity in z-direction	$[\mathrm{m\,s^{-1}}]$
W_{ij}	Rotation rate tensor	
y^+	Non-dimensional wall normal distance	$[-]$

Chapter 1

Introduction

1.1 Background and Motivation

Engine driven vessels for commercial and leisure use have, since the invention of engines relied mainly on fossil fuels as energy source. Fossil fuels, be it in solid, liquid or gasified form, offer extremely high gravimetric and volumetric energy densities and thus make possible high cargo load and or long range without refuelling (Mestemaker et al., 2019).

The needed significant reduction in emission of greenhouse gasses means that also the maritime sector needs to move away from fossil fuels. Unfortunately, this change can not be achieved without a significant penalty in weight and or volume of the carried fuel for the same amount of energy. Hence the only option for keeping the same range between refuelling, with same weight and volume of fuel, is reducing the fuel consumption per nautical mile. The low drag of hydrofoil vessels in foilborne condition, shown in Figure 1.1, is therefore of great interest as a solution to the range problems with new fuels. Hydrofoil vessels in general have good seakeeping characteristics, create small wash, and small speed loss due to incident waves (Faltinsen, 2005). These good characteristics have given hydrofoils a large upturn in popularity in the recent years on everything from foiling windsurfing to larger foiling vessels. Because of the current popularity of using hydrofoils, it can seem like a recent development inside the marine industry. However, this is not the case as the first hydrofoil vessel was built in 1906 (Sheahan, 2022) and the use of foiling passenger ships were fairly common in the 90s. Still, the development of using hydrofoil had a downturn because of complexity. Today, with the further development of hydrofoils and the increasing shortage of energy, the hydrofoil vessel technology might be more mature as a solution to vessel design.

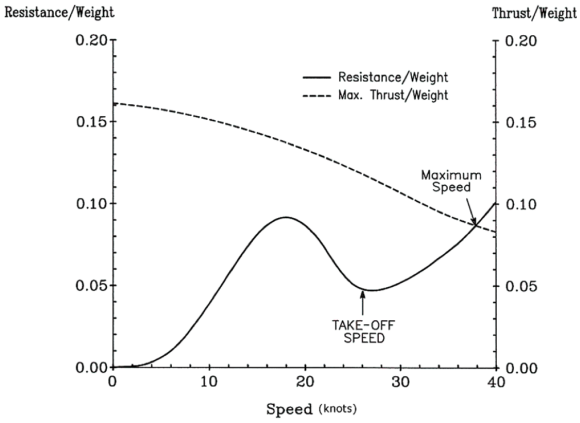

Figure 1.1: Resistance of monohull hydrofoil vessel relative to speed (Faltinsen, 2005)

This thesis is made as a cooperation with the company Lift Ocean whom specialises in delivering hydrofoil systems enabling boat manufacturers to deliver low and zero-emission solutions (LiftOcean, 2022). The design of their hydrofoil system is of paramount importance to achieve low drag without cavitation and ventilation problems. One of the critical parts of the design is the junction between the vertical strut piercing the water surface and the horizontal hydrofoil. One of these junction can be seen in the aft foil of Lift Oceans prototype foiling vessel which is shown in Figure 1.2.

Figure 1.2: Lift Ocean concept foiling boat (LiftOcean, 2022)

The importance of the junction design arises from the meeting boundary layers between the strut and the hydrofoil. Merging boundary layers can cause partial flow separation leading to interference drag. The interference drag of a straight T-junction, shown in Figure 1.3, is as great as a piece of strut having a length "b" equal to 10 times the strut chord (Hoerner, 1965). An example of the importance of the design in this prospect is presented in Figure 1.4 where it can be seen how a fillet of the junction will influence the interference drag. Furthermore, the junction design can influence cavitation problems close the the junction and ventilation issues.

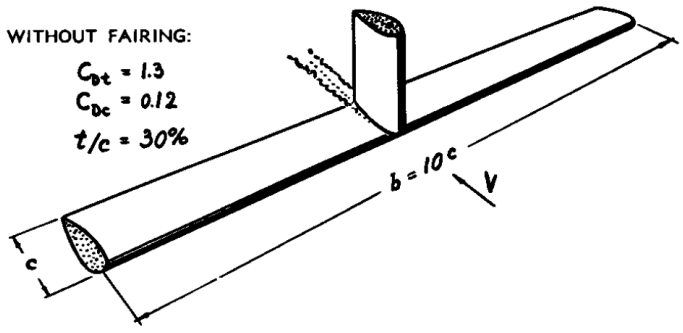

Figure 1.3: Demonstration of the magnitude of interference drag originating at the junction of two struts. The interference drag is as great as the original drag of the larger piece of strut (Hoerner, 1965)

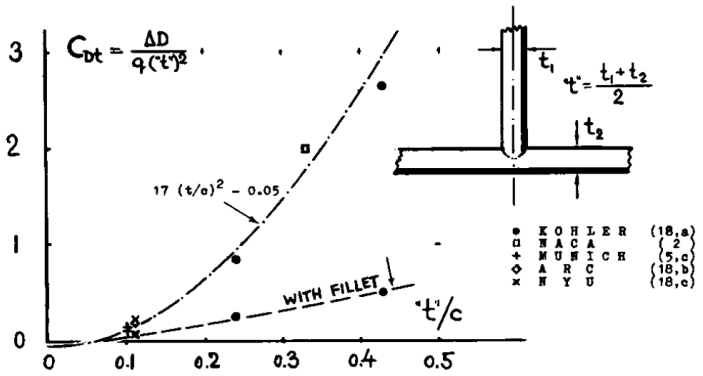

Figure 1.4: Interference drag coefficient (on area t^2) of wing- and strut section; with and without fillets (Hoerner, 1965)

1.2 Objective

Based on the importance of the foil junction design described above, the main objective of the present study is to evaluate designs of the junction between the strut and the hydrofoil with CFD simulations. This objective can be further divided into two parts. Firstly, it aims to establish CFD simulations that strike a balance between accuracy and computational complexity for analysing strut-hydrofoil junctions. Secondly, the established computational setup is to be utilised for evaluating three different strut-hydrofoil designs.

1.3 Scope and Limitations

The scope of this study is a result of a compromise between academic interest and the practical needs of Lift Ocean. Lift Ocean's objective in this thesis was to explore the feasibility of integrating CFD simulations into their design process for analysing the junction design.

To achieve the desired balance between accuracy and complexity in the CFD simulations, an in-depth investigation of appropriate turbulence models is conducted, along with a comprehensive validation study. The validation study involves comparing the CFD simulations with existing experimental data to identify limitations and determine the expected accuracy of the simulations when conducted on strut-hydrofoil junctions.

The three specific strut-hydrofoil designs are: straight T-junction, fillet in the corner junction, and bulb surrounding the corner. These designs are generic to serve as representative cases to gain insight into how different junction shapes influence hydrofoil drag and cavitation. The analysis focuses on evaluating hydrodynamic performance and the likelihood of cavitation inception at a speed of 25 knots, as specified by Lift Ocean.

Considering the computational limitations for Lift Ocean's future use of the numerical setup, the thesis confines the simulations to Reynolds Averaged Navier-Stokes (RANS) simulations. More computationally demanding simulations, such as Large Eddy simulations (LES), are beyond the scope of this thesis. Experimental testing and analysis of the foil designs are also not included due to challenges associated with scaling effects. As the lift and drag of hydrofoils strongly depend on the Reynolds number, scaling down the foil size would require higher fluid velocities than the full scale speed of 25 knots, which are not feasible in available laboratories. Moreover, achieving a sufficiently high Reynolds number and the associated costs of experimental testing and model construction present additional challenges.

1.4 Outline of the Thesis

The thesis consists of six chapters. In addition to the introduction in *Chapter 1*, the chapters can be summarised as follows:

Chapter 2 gives an overview of the theory and literature relevant for the analysis of the strut-hydrofoil junctions.

Chapter 3 introduces the numerical tools that have been used, and explains the methodology behind the analyses carried out.

Chapter 4 gives an uncertainty analysis as well as validation of results by comparing with experimental results.

Chapter 5 presents results from the CFD simulations of the three strut-hydrofoil designs; Straight T-junction, fillet and bulb with discussion of the results.

Chapter 6 gives conclusions from the results, and presents recommendations for further work.

Chapter 2

Theory and Literature

2.1 Foil Theory

2.1.1 Foil Geometry

In Figure 2.1 are some of the most important names and symbols for the geometry of a foil shown. The leading edge is the front of the foil while the trailing edge is the end. The chord length (c) is the length from the leading edge to the trailing edge. When looking at the foil from the side Figure 2.1a it can be seen how the chamber describes the distance between the Nose-tail line and the camber line. From Figure 2.1b it can also be seen that the span (s) is the distance between the tips of the foil and how the chord length may vary along the span of the foil. This variation can be described by the taper ratio according to Equation 2.1. Another parameter which may be used to describe a foil is the aspect ratio which is calculated according to Equation 2.2.

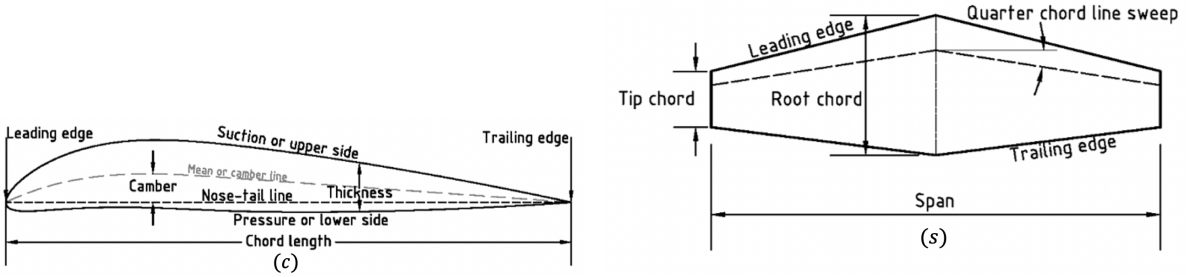

(a) Foil geometry from the side

(b) Foil geometry from the top

Figure 2.1: Foil geometry (Faltinsen, 2005)

$$Taper\ ratio = \frac{Tip\ chord}{Root\ chord} \tag{2.1}$$

$$Aspect\ ratio = \frac{Span^2}{Projected\ foil\ area} \tag{2.2}$$

2.1.2 Lift and Drag

A fluid flowing around a foil profile will create two kinds of stresses which act on it's surface; the wall shear and the pressure stresses. The shear stress acts tangential to the surface and is caused by the frictional forces from the fluids viscosity. The pressure stress acts perpendicular to the surface and arises as a consequence of how the pressure is distributed around the foil profile.

Lift is the resultant of the shear and pressure stresses acting perpendicular to the undisturbed flow which gives Equation 2.3. Where F_L is the lift force, A is the area, P the pressure, τ_w wall shear stress and θ the angle of the force relative to the lift direction. For streamlined bodies like foil profiles the shear stresses will mostly act in the direction of the flow and hence won't contribute significantly to the lift force. Thus they may, for most cases, be neglected.

$$F_L = \int_A (-P \sin\theta - \tau_w \cos\theta) dA \tag{2.3}$$

Pressure stresses are caused by the difference in pressure distribution from the lower and upper sides of the foil section. The pressure difference arises from the fluid velocity being accelerated on the suction side and decelerated on the pressure side of the foil. Bernoulli's principle explains the connection between fluid velocity and the pressure. The difference in fluid velocity from the upper and lower sides of the foil profile can be explained based on the concept of circulation. The flow around a foil is then seen as the superposition of an idealised irrational flow and circulatory flow. By imposing the Kutta condition, flow above and below the foil being parallel when leaving the trailing edge, the circulation generated can be calculated. This circulation will then accelerate the flow at one side of the foil and decelerate it on the other side.

The lift force is commonly expressed non-dimensional as the lift coefficient shown in Equation 2.4. Where C_L is the lift coefficient, ρ density, U free stream velocity and A the area.

$$C_L = \frac{F_L}{0.5\rho U^2 A} \tag{2.4}$$

The lift coefficient of a foil will be dependent on several factors. Enlisted are the factors described by Faltinsen (2005):

- Angle of attack α of the incident flow
- Flap angle δ
- Camber

- Thickness-to-chord ratio
- Aspect ratio
- Ratio between foil submergence, h, and maximum chord length, c
- Submergence Froude number $Fn_h = \frac{U}{(gh)^{0.5}}$
- Interaction from upstream foils
- Cavitation number
- Reynolds number

Drag is the resultant of the shear and pressure stresses acting in the direction of the flow. These stresses may similarly to Equation 2.3 be integrated over the surface in accordance with Equation 2.5.

$$F_D = \int_A (-P\cos\theta + \tau_w \sin\theta) dA \tag{2.5}$$

The drag force can be divided into a viscous and an inviscid part. The viscous part will be due to friction on the foil surface, viscous pressure drag and possible flow separation. For foils and struts will interference drag be an important component. The inviscid drag will be zero for a 2-dimensional foil in a steady flow and infinite fluid. For a 3-dimensional foil will the tip vortexes induce an invicid drag. The tip vortexes are created as a bi-product of the pressure difference between the suction and pressure side. The flow near the tips tends to curl around the tips, being forced from the high pressure region toward the low pressure region (John D. Anderson, 2017). The drag can, similarly to the lift be described through a non dimensional coefficient shown in Equation 2.6.

$$C_D = \frac{F_D}{0.5\rho U^2 A} \tag{2.6}$$

Interference Drag

Junctions between two different parts of a body, e.i. a foil and a strut will usually present a higher combined drag D_{1+2} than the sum of the drag from each individual component $D_1 + D_2$. This difference is the interference drag $\Delta D = D_{1+2} - (D_1 + D_2)$ (Hoerner, 1965). When boundary layers of different thickness meet will vertices be generated at the intersection. A simple case of this phenomenon is the drag of a wing joining a plane wall, similar to a wing body junction, where both the boundary layer of the wing and the wall will join each other at the corner. Subjected to the pressure gradient along the rear end of the foil, the boundary layers are further retarded; and an additional pressure drag (i.e., interference drag) arises (Hoerner, 1965). This drag will not depend on the wing span and a drag coefficient is hence fitted based on the chord area c^2 or thickness area t^2. Hoerner (1965) has made an interpolation of the interference drag

results for a wing flat plate valid for $\delta/c = 10\%$, with delta being the boundary layer thickness at the wall. The plot of these results can be seen in Figure 2.2. The interpolation function of the results is shown in Equation 2.7 with q being the dynamic pressure.

$$C_{Dt} = \frac{\Delta D}{qt^2} = 0.75\left(\frac{t}{c}\right) - \frac{0.0003}{\left(\frac{t}{c}\right)^2} \tag{2.7}$$

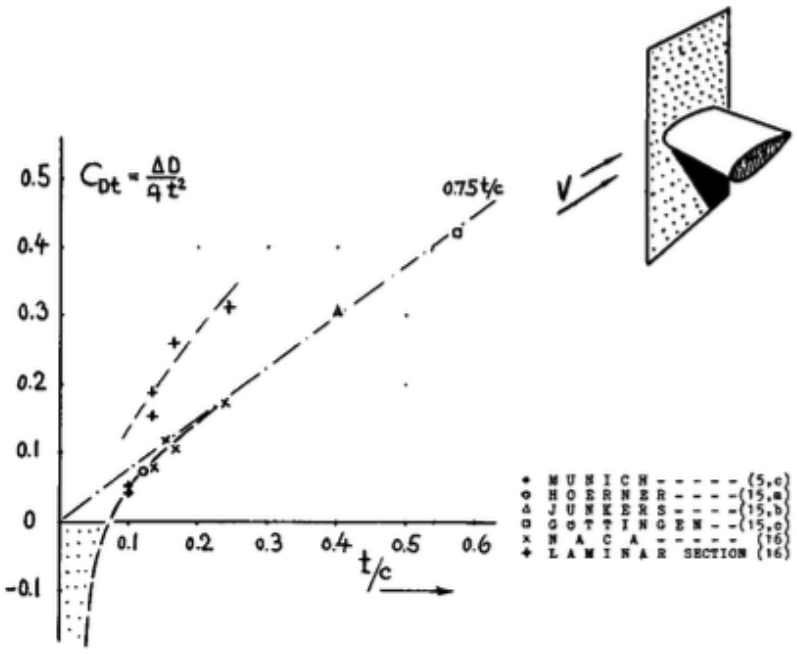

Figure 2.2: Interference drag at the junctions of wing with a plane wall (Hoerner, 1965)

When combining two foils in a T-junction at a place of positive pressure gradient the combined pressure gradients of the two foils are retarding the boundary layer (Hoerner, 1965). Experimental results of such profiles are shown in Figure 1.4. Interpolation of the results gives Equation 2.8.

$$C_{Dt} = \frac{\Delta D}{qt^2} = 17\left(\frac{t}{c}\right)^2 - 0.05 \tag{2.8}$$

There are several methods for reducing the interference drag in the corner of a T-junction. One method is by fairing of the corner. Examples of the influence of a fairing in the corner on the interference drag is shown in Figure 2.3. Different fairing shapes will greatly influence the effect on the interference drag of the fairing. Examples of how fairing shapes influence the interference drag from Hoerner (1965) are shown in Figure 2.4.

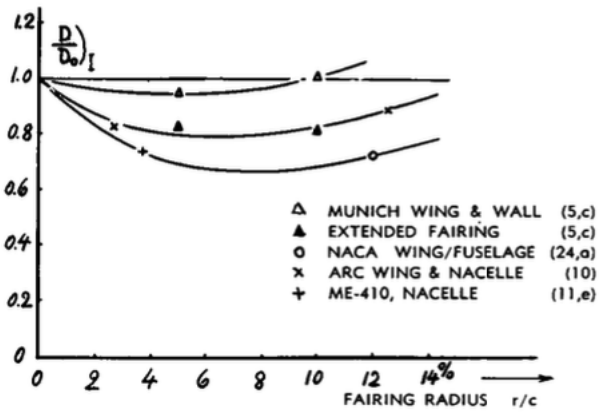

Figure 2.3: Interference drag in corners between wings or tail surfaces and walls, fuselages or nacelles, as a function of the fairing radius (Hoerner, 1965)

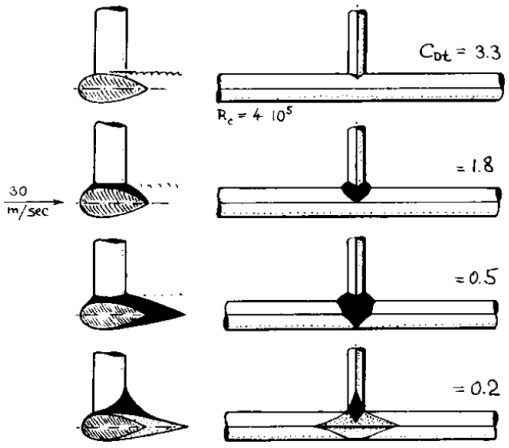

Figure 2.4: Influence of various fairings on the interference drag originating from the junction of two struts having t/c = 43.5 % each (Hoerner, 1965)

2.1.3 Cavitation for Hydrofoils

Cavitation occurs when the total pressure in the water is equal to or lower than the vapor pressure p_v leading to small vapor filled cavities in the liquid. When the pressure again rises above the vapor pressure the vapor filled cavities will implode. This may cause structural damage to the material of the foil. Cavitation can also cause significant reduction in the lift and increase in the drag, as well as noise and vibrations. For a hydrofoil section is the suction side, where the pressure is low, a high risk place for cavitation. Junctions with meeting boundary layers can possibly increase the risk of cavitation on the suction side close to the junction even more. This will be strongly dependent of the design of the junction.

The pressure can be expressed through the non-dimensional pressure coefficient C_p with Equation 2.9. Where ρ is the density, U is the free stream velocity and p the total pressure. The total pressure is calculated in accordance with Equation 2.10 where p_a is the atmospheric pressure,

h the submergence of the foil relative to the free surface and U_L the local flow velocity. With the conditions for cavitation $p < p_v$ will cavitation be dependent on the submergence of the foil, free stream velocity and the local flow velocity. The vapor pressure will be dependent on the temperature of the water and the salt concentration.

$$C_p = \frac{p - p_0}{0.5\rho U^2} \tag{2.9}$$

$$p = p_a + \rho g h + \frac{\rho}{2} U^2 \left(1 - \left(\frac{U_L}{U}\right)^2\right) \tag{2.10}$$

A minimum pressure coefficient, before cavitation occurs can be defined as:

$$C_{Pmin} = \frac{p_v - p_0}{0.5\rho U^2} \tag{2.11}$$

Then a cavitation number can be defined as shown in Equation 2.12, and a requirement for cavitation not to occur as in Equation 2.13.

$$\sigma_i = -C_{Pmin} \tag{2.12}$$

$$-C_p < \sigma_i \tag{2.13}$$

2.2 Mathematical Description of Computation Fluid Dynamics

2.2.1 Navier-Stokes Equations

Navier-Stokes equations govern the motions of incompressible fluids. They are partial differential equations which mathematically express the momentum balance and conservation of mass. If the total derivative is defined according to Equation 2.14. Where u, v and w are the fluid velocity in the x, y and z direction, respectively.

$$\frac{D}{Dt} = \frac{\partial}{\partial t} + u\frac{\partial}{\partial x} + v\frac{\partial}{\partial y} + w\frac{\partial}{\partial z} \tag{2.14}$$

The Navier-stokes equations can then be written as Equation 2.15. Where ρ is the density of the fluid and g the gravity.

$$\begin{aligned}\frac{Du}{Dt} &= \frac{-1}{\rho} + g_x + \nu\nabla^2 u \\ \frac{Dv}{Dt} &= \frac{-1}{\rho} + g_y + \nu\nabla^2 v \\ \frac{Dw}{Dt} &= \frac{-1}{\rho} + g_z + \nu\nabla^2 w\end{aligned} \tag{2.15}$$

With the incompressible continuity equation in the form of Equation 2.16.

$$\frac{\partial u}{\partial x} + \frac{\partial v}{\partial y} + \frac{\partial w}{\partial z} = 0 \tag{2.16}$$

2.2.2 Turbulence

In fluid dynamics, turbulence is characterised by chaotic changes in flow velocity, illustrated in Figure 2.5. It arises from the interaction between different scales of motion within the fluid, and occurs when the fluid flow becomes unstable and transitions from smooth, laminar flow to a turbulent state. In laminar flow, the fluid moves in orderly layers or streamlines, while in turbulent flow, these streamlines become highly disordered and exhibit random fluctuations.

The Navier-Stokes equations can be used directly for solving the turbulent flow problem (DNS), but the calculations are extremely demanding and time-consuming. This is because turbulent flows contain a large variety of fluid motions. Solving these equations on a grid requires a grid size small enough to resolve even the smallest motions, but also a domain large enough to cover the largest motions. A less computationally demanding, but still time consuming, simulation method is Large Eddy simulations (LES). In LES simulations, the larger 3-dimensional unsteady turbulent motions are directly represented, whereas the effects of the smaller scale motions are modelled (Pope, 2000). Even less computationally demanding are the Reynolds-Averaged Navier-Stokes (RANS) simulations which will be further explained in the next section.

2.2.3 Reynolds-Averaged Navier-Stokes Equations

In order to reduce the computational power needed in the calculations of the turbulent Navier-Stokes equations a Reynolds averaging of the Navier-Stokes equations can be used. Instead of focusing on the instantaneous velocity at a point in the flow the focus will instead lie on the time average velocity and the deviation from this time average. Thus the velocity components and pressure are split into a mean and a fluctuating part according to Equation 2.17. The mean and fluctuating part is visualised in Figure 2.5.

$$\begin{aligned}u &= \overline{U} + u'(t) \\ v &= \overline{V} + v'(t) \\ w &= \overline{W} + w'(t) \\ p &= \overline{P} + p'(t)\end{aligned} \tag{2.17}$$

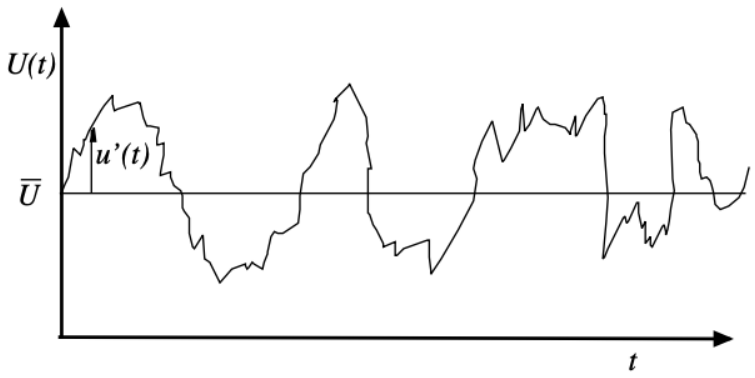

Figure 2.5: Mean and fluctuating part of the velocity (Dawson, 2021)

Substituting the velocity components split into a mean and fluctuating part in the continuity equation, Equation 2.16, gives the Reynolds-average continuity equation in tensor notation as

$$\frac{\partial \bar{u}_j}{\partial x_j} = 0 \tag{2.18}$$

Substituting the velocity and pressure components from Equation 2.17 into the Navier-stokes equations and taking the time average, gives the Reynolds-Averaged Navier-Stokes equations (RANS). The RANS equations in tensor notation are shown in Equation 2.19 (Tannehill et al., 1997).

$$\frac{\partial}{\partial t}(\rho \bar{u}_i) + \frac{\partial}{\partial x_j}(\rho \bar{u}_i \bar{u}_j) = -\frac{\partial \bar{p}}{\partial x_i} + \frac{\partial}{\partial x_j}(\bar{\tau}_{ij} - \rho \overline{u_i' u_j'}) \tag{2.19}$$

Where,

$$\bar{\tau}_{ij} = \mu(\frac{\partial \bar{u}_i}{\partial x_j} + \frac{\partial \bar{u}_j}{\partial x_i}) \tag{2.20}$$

Since the equations have been averaged, some information have been lost. Thus, there is now more unknowns than equations. The term $\bar{\tau}_{ij}$ is connected with the viscous stresses. The term $\rho \overline{u_i' u_j'}$ is the Reynolds stresses arising from the turbulent stresses. The Reynolds stresses are the new unknowns and can be further analysed with the help of turbulence models.

2.2.4 RANS Turbulence Modelling

The Reynolds stresses can be determined by a turbulence model. Two methods is turbulence models based on either the turbulent viscosity hypothesis or more directly from the modelled Reynolds stress transport equations. Models based on the turbulent viscosity hypothesis can

also be called Eddy Viscosity Models (EVM), and those based on Reynolds stress transport equations Reynolds stress models (RSM) or differential stress models (DSM).

Eddy viscosity models are based on the turbulent viscosity hypothesis and common examples of two such models are the $k-\varepsilon$ and the $k-\omega$ models. Both $k-\varepsilon$ and $k-\omega$ are two equation models which can be solved for the turbulence parameters k ε and k ω, respectively. Where k is the turbulent kinetic energy, ε the dissipation rate of turbulent kinetic energy and ω the turbulence frequency. The turbulent viscosity hypothesis, introduced by Boussinesq in 1877, is show in Equation 2.21. Where δ_{ij} is Kronecker delta and ν_T the turbulent viscosity. The equation is mathematically analogous to the stress-rate-of-strain relation for a Newtonian fluid (Pope, 2000).

$$\overline{u_i' u_j'} = \frac{2}{3} k \delta_{ij} - \nu_T \left(\frac{\partial \overline{U_i}}{\partial x_j} + \frac{\partial \overline{U_j}}{\partial x_i} \right) \tag{2.21}$$

With the anisotropic Reynolds stresses a_{ij} and mean rate-of-strain tensor $\overline{S_{ij}}$ defined according to Equation 2.22 and 2.23, respectively.

$$a_{ij} = \overline{u_i' u_j'} - \frac{2}{3} k \delta_{ij} \tag{2.22}$$

$$\overline{S_{ij}} = \frac{1}{2} \left(\frac{\partial \overline{U_i}}{\partial x_j} + \frac{\partial \overline{U_j}}{\partial x_i} \right) \tag{2.23}$$

The turbulent viscosity hypothesis can be written as Equation 2.24, which implies that the anisotropy tensor a_{ij} is aligned with the mean rate-of-strain tensor. Both a_{ij} and $\overline{S_{ij}}$ have 5 independent components which according to the turbulent viscosity hypothesis are related through the scalar coefficient ν_T. Even in simple shear flows is this found to not be true (Pope, 2000) and is then one of the shortcomings with the EVM models, creating problems with properly representing strongly 3-dimensional flows.

$$a_{ij} = -2\nu_T \overline{S_{ij}} \tag{2.24}$$

In Reynolds stress models are the transport equations solved for the individual Reynolds stresses $\overline{u_i' u_j'}$, hence the turbulent viscosity hypothesis is not needed. This eliminates one of the major shortcomings of the EVMs models. The transport equation for the Reynolds stress tensor is derived from the Navier-Stokes equation and is shown in Equation 2.25. Where T_{kij} is the Reynolds stress flux, $\mathcal{P}_{ij}$ is the production tensor of Reynolds stress, $\mathcal{R}_{ij}$ the pressure rate of strain tensor and ε_{ij} the dissipation tensor. Though the Reynolds stress models produce a stronger closure to the flow problem the models have not become widely used. This is because of more stability problems and being more computationally expensive than the Eddy viscosity models.

$$\frac{D\overline{u_i u_j}}{Dt} + \frac{\partial}{\partial x_k} T_{kij} = \mathcal{P}_{ij} + \mathcal{R}_{ij} - \varepsilon_{ij} \tag{2.25}$$

2.2.5 k-ω SST Turbulence Model

The $k-\omega$ SST model is among the most popular models and is a two-equation Eddy-viscosity model. Hence based on the turbulent viscosity hypothesis presented in Subsection 2.2.4. The model combines the standard $k-\varepsilon$ and $k-\omega$ models by rewriting both k and ϵ in terms of ω (T.S.Klein et al., 2015). The reason for combining both the models is that the best from each of them are used. The standard $k-\omega$ model is superior to the $k-\varepsilon$ model in the boundary layer, but has a common problem with being too sensitive to the inlet free-stream turbulence properties (Menter et al., 2003). Thus the $k-\omega$ SST model switches to a k-ε model in the free stream outside the boundary layer, and by that combining the best out of both models. The $k-\omega$ SST model is known for very good behaviour in adverse pressure gradient and separating flow compared with other EVM turbulence models. However, the model produces a bit too large turbulence levels in regions with large normal strain, like stagnation regions and regions with strong acceleration (Jamspali, 2022).

The $k-\omega$ SST turbulence model integrated in OpenFOAM is based on the 2003 $k-\omega$ SST model (Menter et al., 2003). The formulation of the SST model is given in Equation 2.26 and 2.27.

$$\frac{\partial(\rho k)}{\partial t} + \frac{\partial(\rho U_i k)}{\partial x_i} = \rho \tilde{P}_k - \beta^* \rho \omega k + \frac{\partial}{\partial x_i}\left[(\mu + \mu_t \sigma_k)\frac{\partial k}{\partial x_i}\right] \tag{2.26}$$

$$\frac{\partial(\rho \omega)}{\partial t} + \frac{\partial(\rho U_i \omega)}{\partial x_i} = \alpha \rho S^2 - \beta \rho \omega^2 + \frac{\partial}{\partial x_i}\left[(\mu + \mu_t \sigma_\omega)\frac{\partial \omega}{\partial x_i}\right] + 2\rho(1-F_1)\sigma_{\omega 2}\frac{1}{\omega}\frac{\partial k}{\partial x_i}\frac{\partial \omega}{\partial x_i} \tag{2.27}$$

Where k is the turbulent kinetic energy, ω the specific Eddy dissipation rate and $\tilde{P}_k$ the turbulent kinetic energy production rate. β, β^*, σ_k, σ_ω, and $\sigma_{\omega 2}$ are constants. These constants are linearly interpolated between the k-ε and the k-ω with $\phi = F_1\phi_\omega + (1-F_1)\phi_\epsilon$. Where ϕ is a general representation of the constants. F_1 is a blending function which changes between the $k-\epsilon$ and $k-\omega$ model by looking at the closeness to a wall. The blending function is defined by:

$$F_1 = \tanh\left(\left(\min\left[\max\left(\frac{\sqrt{k}}{\beta^*\omega y}, \frac{500\nu}{y^2\omega}\right), \frac{4\rho\sigma_{\omega 2}k}{CD_{k\omega}y^2}\right]\right)^4\right) \tag{2.28}$$

Where,

$$CD_{k\omega} = \max\left(2\rho\sigma_{\omega 2}\frac{1}{\omega}\frac{\partial k}{\partial x_i}\frac{\partial \omega}{\partial x_i}, 10^{-10}\right) \tag{2.29}$$

The turbulent Eddy viscosity is defined with a viscosity limiter according to Equation 2.30 in the SST model (F. R. Menter, 1994).

$$\nu_t = \frac{a_1 k}{\max(a_1\omega, SF_2)} \tag{2.30}$$

Where S is the invariant measure of the strain rate and F_2 another blending function defined as:

$$F_2 = \tanh\left[\left[\max\left(\frac{2\sqrt{k}}{\beta^*\omega y}, \frac{500\nu}{y^2\omega}\right)\right]^2\right] \tag{2.31}$$

2.2.6 Elliptic Blending Reynolds Stress Model

The Elliptic Blending Reynolds Stress Model (EBRSM) was first presented by Manceau and Hanjalić (2002). It is a Reynolds stress model and was created in order to make a more robust and industry friendly RST model than previous models. Several modifications to the original model has been made. The theory presented about the model here is in accordance with Manceau (2015) which is the version implemented in OpenFOAM.

$$\frac{D\overline{u_i u_j}}{Dt} = \mathcal{P}_{ij} + \phi^*_{ij} - \varepsilon_{ij} + \mathcal{D}^t_{ij} + \frac{\partial}{\partial x_k}\left(\nu\frac{\partial\overline{u_i u_j}}{\partial x_k}\right) \tag{2.32}$$

In Equation 2.32 is P_{ij} the production tensor, ϕ^*_{ij} the pressure-strain tensor, ε_{ij} the dissipation-rate tensor and $\mathcal{D}^t_{ij}$ the turbulent diffusion tensor. In the EBRSM is the pressure-strain and dissipation tensor modelled with a blending of the near wall model $\phi^w_{ij} - \varepsilon^w_{ij}$ and homogeneous model $\phi^h_{ij} - \varepsilon^h_{ij}$. Which gives rise to Equation 2.33.

$$\phi^*_{ij} - \varepsilon_{ij} = (1-\alpha^3)(\phi^w_{ij} - \varepsilon^w_{ij}) + \alpha^3(\phi^h_{ij} - \varepsilon^h_{ij}) \tag{2.33}$$

Where α is the blending parameter which is a solution to the elliptic equation $\alpha - L^2\nabla^2\alpha = 1$. At solid walls is $\alpha = 0$ while in the free stream is $\alpha = 1$. L is a length scale which can be defined as:

$$L = C_l \max\left(\frac{k^{\frac{3}{2}}}{\varepsilon}, C_\eta\frac{\nu^{\frac{3}{4}}}{\varepsilon^{\frac{1}{4}}}\right) \tag{2.34}$$

Where C_l and C_η are constants. In the outer region is the pressure-strain relationship defined in accordance with the quasi-linear SSG model from Speziale et al. (1991) which is shown in Equation 2.35.

$$\begin{aligned}\phi^h_{ij} = &-\left(C_1 + C^*_1\frac{\mathcal{P}}{\varepsilon}\right)\varepsilon a_{ij} + \left(C_3 - C^*_3\sqrt{a_{kl}a_{kl}}\right)kS_{ij} \\ &+ C_4 k\left(a_{ik}S_{jk} + a_{jk}S_{ik} - \frac{2}{3}a_{lm}S_{lm}\delta_{ij}\right) + C_5 k\left(a_{ik}W_{jk} + a_{jk}W_{ik}\right)\end{aligned} \tag{2.35}$$

Where $\mathcal{P}$ is the production of kinetic energy which is equal to $\mathcal{P} = P_{ii}/2$. While $a_{ij} = \overline{u_i u_j}/k - (2/3)\delta_{ij}$ is the anisotropy tensor, $S_{ij} = \frac{1}{2}(\frac{\partial U_i}{\partial x_j} + \frac{\partial U_j}{\partial x_i})$ is the strain-rate tensor and $W_{ij} = 1/2(\frac{\partial U_i}{\partial x_j} + \frac{\partial U_j}{\partial x_i}) + \epsilon_{mji}\omega_m$ is the rotation rate tensor with ω_m the system rotation vector. The terms C_1, C_1^*, C_3, C_3^*, C_4 and C_5 are constants related to the model.

Also in the outer region is the dissipation-rate tensor defined as:

$$\varepsilon_{ij}^h = \frac{2}{3}\varepsilon\delta_{ij} \tag{2.36}$$

For the near wall region is the pressure-strain and dissipation-rate defined according to

$$\phi_{ij}^w = -5\frac{\varepsilon}{k}\left(\overline{u_i u_k}n_j n_k + \overline{u_j u_k}n_i n_k - \frac{1}{2}\overline{u_k u_l}n_k n_l(n_i n_j + \delta_{ij})\right) \tag{2.37}$$

$$\varepsilon_{ij}^w = \frac{\overline{u_i u_j}}{k}\varepsilon \tag{2.38}$$

Where the wall normal direction can be computed directly from the elliptic blending parameter as:

$$n_k = \frac{\frac{\partial \alpha}{\partial x_k}}{\sqrt{\frac{\partial \alpha}{\partial x_l}\frac{\partial \alpha}{\partial x_l}}} \tag{2.39}$$

In Lardeau and Manceau (2014) was, together with simulation results with the EBRSM model a new method for generating initial conditions published. The method should overcome some issues with slow or non-convergence in the initial stages of the computation. The method is implemented in OpenFOAM through the `setTurbulenceFields` utility and the only user dependent input is the flow velocity. With this method the initial conditions of the turbulence parameters can then be calculated by defining a friction velocity $u_\tau = 0.05U_{ref}.$, Which then is used in Equation 2.40 and 2.41. Further explanation of the method implemented in OpenFOAM can be found in Lardeau and Manceau (2014).

$$k = \frac{u_\tau^2}{\sqrt{C_\mu}} \tag{2.40}$$

$$\varepsilon = \frac{u_\tau^4}{\kappa\nu d_{ref}^+} \tag{2.41}$$

2.2.7 Boundary Layer Treatment

Near walls the velocity profile will have a large gradient due to the no slip conditions. In order to properly capture the large velocity gradient are very small layers of cells in the near wall

region are needed for CFD simulations, illustrated in Figure 2.6. This fine grid resolution close to the wall increases the computational time and the aspect ratio of the cells close the the wall. The large aspect ratio may also induce stability issues.

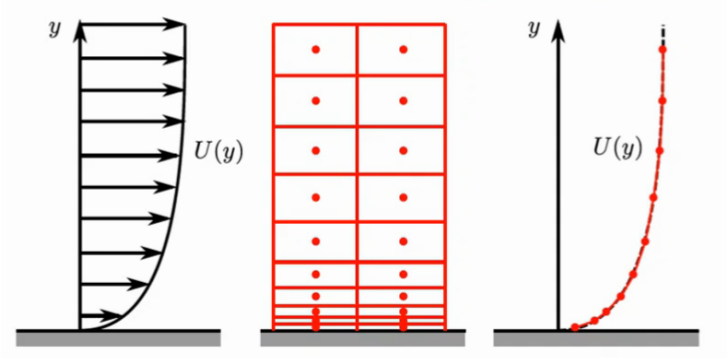

Figure 2.6: Velocity profile and grid resolution (Wimshurst, 2023)

Experiments of the flow profiles close to walls for wall bounded flows have shown self similarity which is used for the wall treatment in CFD. Self similarity means that flow profiles show similarity if the independent and dependent variables are appropriately scaled. The velocity and distance to the wall can be made non-dimensional by use of the reference velocity based on the wall shear stress u_τ. Where u_τ is defined as:

$$u_\tau = \sqrt{\frac{\tau_w}{\rho}} \tag{2.42}$$

The non-dimensional velocity and wall normal distance can then be defined according to Equation 2.43 and 2.44, respectively.

$$U^+ = \frac{U}{u_\tau} \tag{2.43}$$

$$y^+ = \frac{y u_\tau}{\nu} \tag{2.44}$$

A plot of the velocity profile in the boundary layer with the non-dimensional velocity and the wall normal distance gives the black line in Figure 2.7. The behaviour of the profile can be divided into three different sections; The viscous sub-layer ($y^+ < 5$), the buffer layer ($5 < y^+ < 30$) and the Log-law region ($y^+ > 30$). In the viscous sub-layer is the velocity profile linear with $u^+ = y^+$. For the log-law region the velocity profile will follow a log-law: $u^+ = \frac{1}{\kappa} ln(y^+) + B$. In the buffer layer is the velocity profile neither linear nor logarithmic, but a transition from the linear to the logarithmic region.

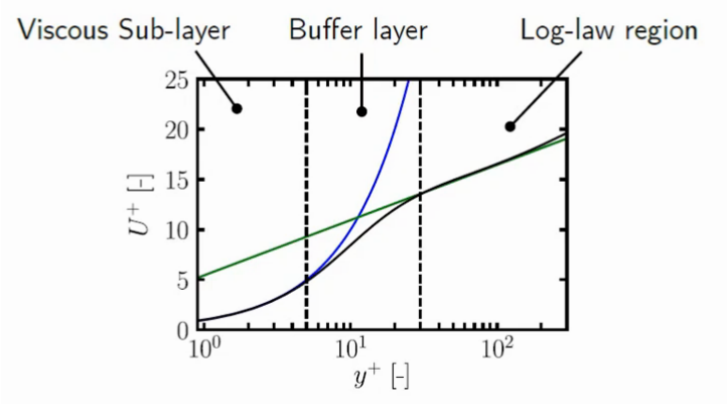

Figure 2.7: Velocity profile in the boundary layer (Wimshurst, 2023)

For CFD simulations there is different methods for simulating the flow in the boundary layer. One method is to resolve the boundary layer. The first cell will then need to be inside the viscous sub-layer, so $y^+ < 5$ and ideally $y^+ < 1$. An alternative method is to use wall functions to model the flow inside the log-law region. With this method the centre of the first cell can be positioned inside the log-law region, so $30 < y^+ < 300$. In Figure 2.8 is the different cell height and modelling approaches illustrated. The wall treatments available will also be dependent on the turbulence model used in the CFD simulations. The k-omega SST model may be used with both resolving the boundary layer and with wall functions.

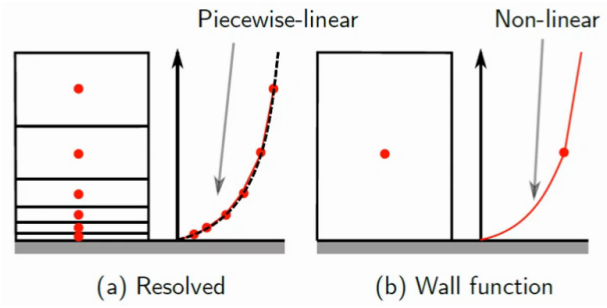

Figure 2.8: Different wall treatment for CFD simulations (Wimshurst, 2023)

2.2.8 Courant Number

The Courant number is of importance for stability in transient CFD simulations. The Courant number is calculated in OpenFOAM in accordance with Equation 2.45 (OpenFOAM, 2023a). Maximum Courant number which still ensure stability is dependent on whether an explicit or implicit time scheme is used. For an explicit time scheme is $Co < 1$ needed to ensure that a fluid particle does not move through a whole cell during one time step. For implicit time scheme can the Courant number be higher with stable solutions.

$$Co = \frac{1}{2} \cdot \Delta_t \cdot \frac{\sum_{faces} |\phi_i|}{V} \tag{2.45}$$

2.3 Literature Study

The documented research of experiments and CFD analysis of different hydrofoil junction designs are limited. As studies from the aeronautical industry is closely related, highly relevant and several published studies are available, the focus of this literature study will be on that. In the following literature study are research and scientific papers on the following topics presented; Experimental and computational results of a NACA 0012 foil profile, Stream wise corner flow, flow over wing body junction and simulations based on an elliptic blending Reynolds stress model.

The NACA 0012 experimental and computational results are included as a comparison for the validation study presented in Chapter 4. As mentioned in the introduction the hydrofoil junctions evaluated in this thesis will create meeting boundary layers, hence experimental data and CFD analysis of flows with meeting boundary layers are of interest. The stream wise corner flow, a very simple set up, is used to attain some generic knowledge about meeting boundary layers. A more closely related case to the flow over the hydrofoil junctions is the wing body junctions. For wing body junctions both experimental data and CFD analysis of the flows are studied. An assessment of performance of the different turbulence models in describing the flow close to the junction is summarised and will be further used in order to decide the appropriate turbulence model for simulations of the hydrofoil junction designs. For the wing body junction is also some research on different methods to suppress the secondary flows created by the meeting boundary layers presented. Finally, some research on the performance of the EBRSM turbulence model are presented. This is included because it is the most recent Reynolds stress model implemented in OpenFOAM and a promising step towards an appropriate turbulence model for simulations of the hydrofoil junction designs. The following section is to a large extent based on previous work from the project thesis delivered spring 2022.

2.3.1 Experimental and Computational Results for NACA 0012

Numerous experiments on NACA foils of different shapes and different flow conditions are published. The focus here is the NACA 0012 with a Reynolds number of 6 million. Different experimental data has been gathered by NASA. The results for lift and drag coefficient are presented in Figure 2.9 and the pressure coefficient at and angle of attack of 0 degrees in Figure 2.10. The data from Charles L. Ladson (1988) are the only experiment where some of them are tripped. The data are tripped in order to fix the transition to turbulence, which are done using either a 60, 80, 120 or 180 grit. The Charles L. Ladson (1988) tripped experiments appear to be the most appropriate for comparison with fully turbulent CFD simulations at $Re = 6 \cdot 10^6$ (NASA, 2022).

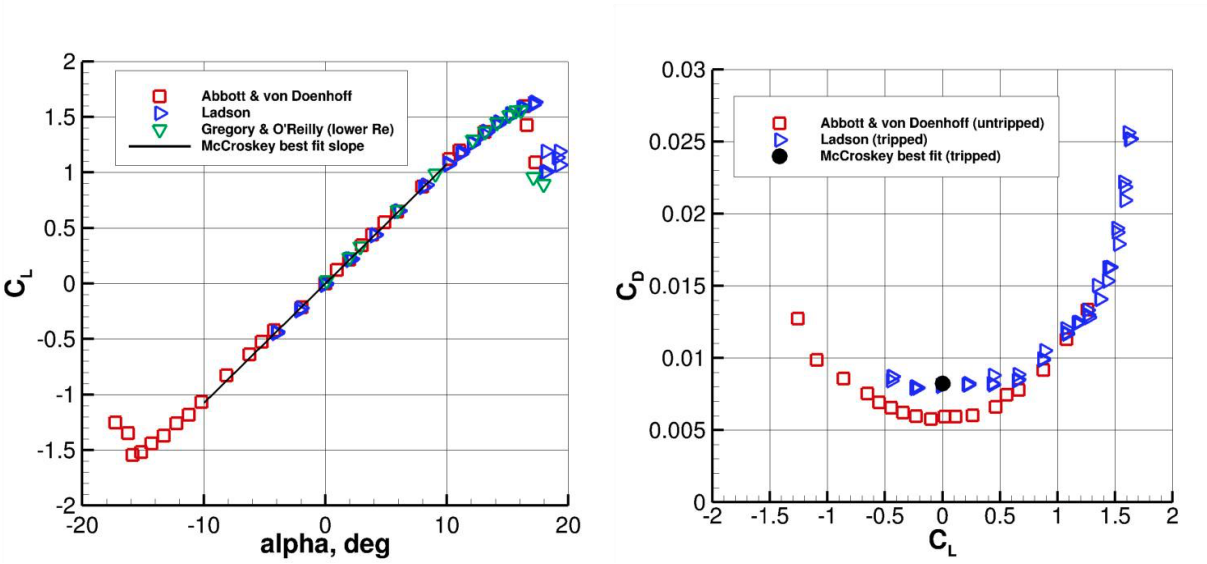

(a) C_L relative to α

(b) C_D relative to C_L

Figure 2.9: Experimental data for lift and drag coefficient of a NACA 0012 profile at different angles of attack α (NASA, 2022)

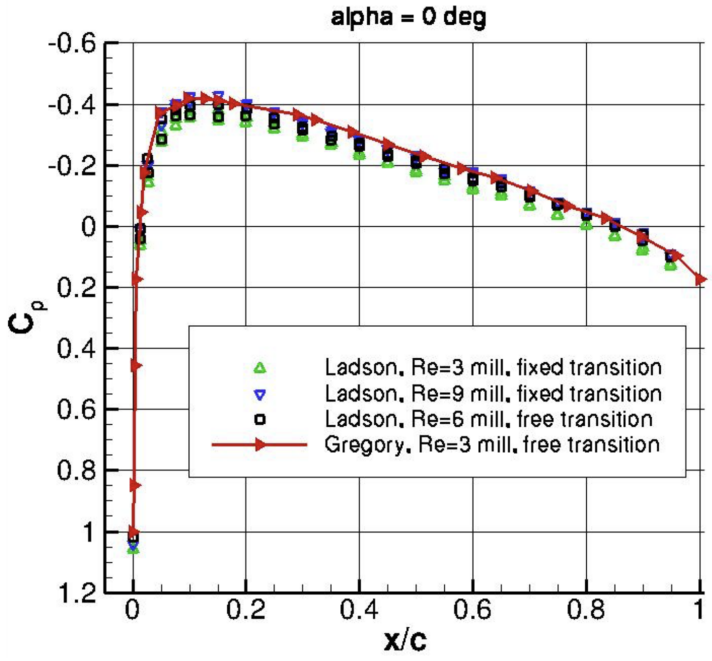

Figure 2.10: C_p relative to positions along the foil for $\alpha = 0$ (NASA, 2022)

NASA has also gathered CFD results for the NACA0012 airfoil with a Reynolds number 6 million (NASA, 2023). The $k - \omega$ SST model is used for the CFD simulations. A comparison of the CFD results with the experimental data from Charles L. Ladson (1988) is presented in Figure 2.11. Very good agreement between the experimental data and the CFD simulations is shown in this study, especially at low angles of attack.

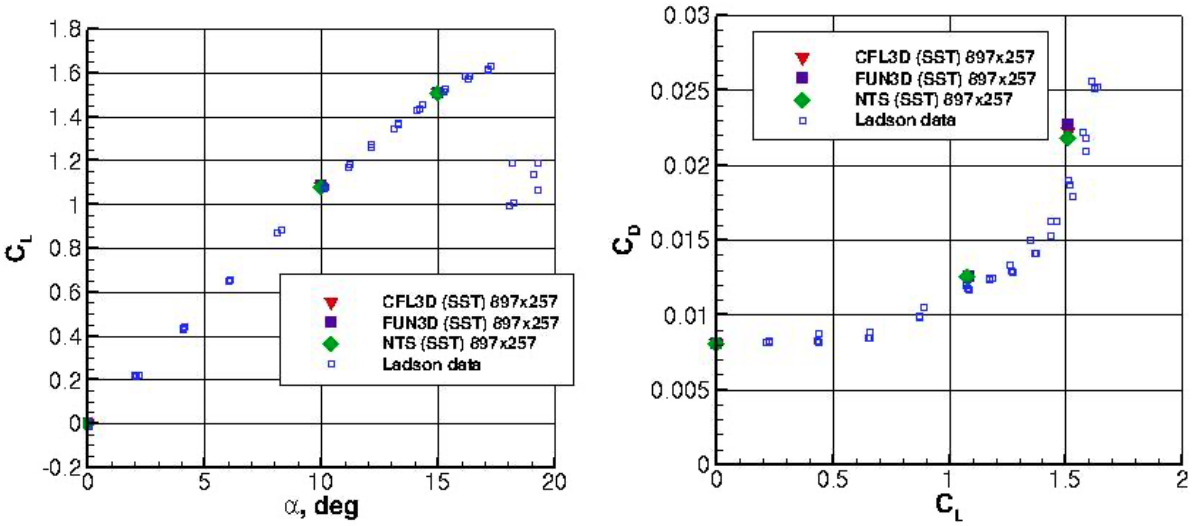

(a) C_L relative to α

(b) C_D relative to C_L

Figure 2.11: CFD results lift and drag coefficient of a NACA 0012 profile at different angles of attack α (NASA, 2023)

2.3.2 Streamwise Corner Flow

The stream wise corner flow has attracted much attention during the past 50 years due to the similarity to the flow conditions between a wing and a body. The corner flow is inherently 3D in character because of the viscous interaction between the meeting boundary layers. The meeting boundary layers create a secondary flow with components in the plane perpendicular to the main flow. There are two kinds of secondary flows. The first arises due to development of the mean vorticity, running along the flow and induced by the flow skewness in the mean shear plane (Kornilov, 2017). The second type of secondary flow is caused by the gradient of the Reynolds stresses in the stream wise corner perpendicular to the flow direction. Examples of a secondary flow profiles is shown in Figure 2.12. Numerous attempts to describe the flow patterns both analytically and numerically have been carried out most of them with limited success due to complicated flow pattern of the merging boundary layers. Detailed examination of the problem revealed high sensitivity of the experimental set up to be a major problem. Hence a clear view on how the exact flow should be developed is difficult to achieve and thus the reason why no flow solutions, but only a summary of important solutions will be presented in this literature review.

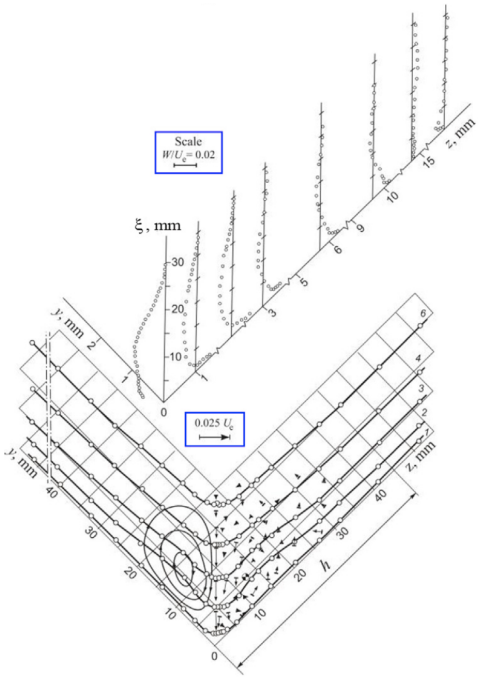

Figure 2.12: Experimental streamwise velocity contours, secondary velocity vector in the yz cross-section of streamwise corner (bottom) and z-component of mean velocity profiles (top) at $Re = 1.75 \cdot 10^6$ (Kornilov, 2017)

The problem was first investigated mathematically by Carrier (1947). The solution suggested involved a split of the continuity equation. The solution has later been criticised as the cross-plane vorticity equation remained unsatisfied. Rubin (1966) was the first study which systematically formulated the corner layer equations for a corner using the method of matched asymptotic expansions. Later, several attempts of numerically solving the corner layer equations have been tested. One of these attempts were done by Ghia who obtained the numerical solutions by an alternating direction implicit scheme (Ghia, 1975). All the numerical solutions showed some differences on velocity and secondary flow pattern due to differences associated with boundary condition treatment and the numerical method chosen.

Several experimental studies of flow over a stream wise corner have been performed. An interesting one was performed by Zamir and Young (1970), who later in Zamir (1981) pointed out the large deviations between the different experimental results. The experimental studies were not able to give a unified picture of the stream wise corner flow with high variations in flow field, indicating an extremely sensitive laminar flow in the corner region. Factors like shape of the leading edge, angle of the corner model and others all slightly alter the flow and thus influence the experimental data and results dramatically. This instability was also shown and investigated by Alizard et al. (2009). Zamir (1981) also predicted the corner layer under a zero pressure gradient only to be stable for a Reynolds number from the leading edge of about 10^4, which is one order lower than the Schlichting disturbance in a two-dimensional Blassius boundary layer (Parker and Balachandar, 1999). Further experiments on flow over a stream wise corner are done by Park et al. (2010). In this study the experimental analysis is approached by changing the measurement technique from a conventional hot-wire anemometer to a particle image veloci-

metry (PIV). The benefit of PIV measurement is that no disturbance in the desired flow field is created. However, their boundary layer results did not show any significant difference from the previous experiments other that those expected according to the instability of the corner flow.

2.3.3 Flow over Wing Body Junction

The flow over a wing body junction inherits the same complex 3D character as the corner flow because of the meeting boundary layers. An extensive experimental study of the wing body junction flow has been carried out by Fleming et al. (1993). They measured the flow around a 3:2 semi-elliptic nose/NACA0020 tail section attached to a flat plate. A mean and fluctuating velocity adjacent to the wing and up to 11.56 chord lengths downstream was measured. The results show that the dominating flow characteristic is the mean secondary flow structure known as the horseshoe vortex. The horseshoe vortex is visualised in Figure 2.13. The vortex flow structure is created from the skewing and stretching of the transverse vorticity present in the incoming turbulent boundary layer as it passes the wing, combined with the rolling up of the incoming fluid along the centerline due to large adverse pressure gradient created by the wing geometry (Fleming et al., 1993). The measurements show elliptical shape of the horseshoe vortex flow, with $\partial W/\partial Y$ creating the main component of the of the stream wise vorticity. Where W is the velocity in the z-direction.

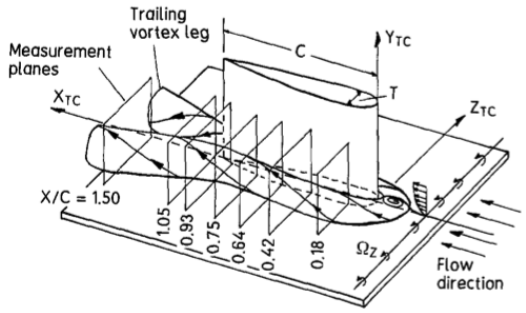

Figure 2.13: Wing body junction with characteristic horseshoe vortex (Fleming et al., 1993)

Apsley and Leschziner (2001) performed a numerical modelling study with focus on different turbulence models for Reynolds Averaged Navier Stokes (RANS). The study was carried out by use of the same 3:2 semi-elliptic nose/NACA0020 tail section geometry which was used in Fleming et al. (1993). Modelling junction flows of this type introduce several difficulties. Firstly, due to the curvature of the wing careful attention to the grid quality and numerical resolution are needed in order to correctly represent the highly strained flow close to the surface (Apsley and Leschziner, 2001). Secondly, a lot of the important flow aspects happen close to the wall, hence the near wall region needs to be resolved in detail. Lastly, the high curvature and strong normal straining of the flow in the stagnation region will create anisotropy of the turbulent normal stresses and thus, it's interaction with the other strain components becomes influential and needs careful examination and modelling (Apsley and Leschziner, 2001). Apsley and Leschziner (2001) investigated the predictive performance of 12 different turbulence models. The turbulence models tested can be divided into three main categories: linear Eddy-viscosity models (EVM),

non-linear Eddy-viscosity formulations (NLEVM) and differential stress ('Second-moment closure') models (DSM). The turbulence models which have been tested by Apsley and Leschziner (2001) are listed in Table 2.1.

Table 2.1: Turbulence models tested in study by Apsley and Leschziner (2001)

Model	Type	Transport equations
Launder and D. B. Spalding (1974)	EVM	k, ε
Launder and Sharma (1974)	EVM	k, $\tilde{\varepsilon}$
Wilcox (1988b)	EVM	k, ω
Kalitzin et al. (1996)	EVM	k, g
F. R. Menter (1994)	EVM	k, ω
Gatski and Speziale (1993)	NLEVM	k, ε
Apsley and Leschziner (1998)	NLEVM	k, ε
Lien et al. (1998)	NLEVM	k, ε
Gibson and Launder (1978)	DSM	$\overline{u_i u_j}$, ε
Speziale et al. (1991)	DSM	$\overline{u_i u_j}$, ε
Jakirlic and Hanjalic (1995)	DSM	$\overline{u_i u_j}$, ε
Wilcox (1988a)	DSM	$\overline{u_i u_j}$, ω, k^U

The results of their study show clearly that for this type of complex 3D flows the second moment close turbulence models seem to have predictive advantages over the other models, although they are far from perfect, as shown when comparing the results with the experimental data from Fleming et al. (1993). Other models which perform reasonably well are the SST (F. R. Menter, 1994) and the $k - g$ (Kalitzin et al., 1996), but only in simulating the mean-flow features. According to Bradshaw (1987) are the turbulence models originally developed for 2-dimensional flows struggling when extended into 3-dimensional flows. As mentioned initially, the wing body junction inherits complex 3-dimensionality because of the meeting boundary layers. The simulation results of the secondary flow W with different turbulence models compared with experimental results are shown in Figure 2.14. Results for the pressure coefficient along the wing surface for some EVM turbulence models and some DSM turbulence models are shown in Figure 2.15a. Presented in Figure 2.15b is the contour plot of the pressure coefficient at the bottom wall from the simulations with $k - \omega$ SST in Apsley and Leschziner (2001).

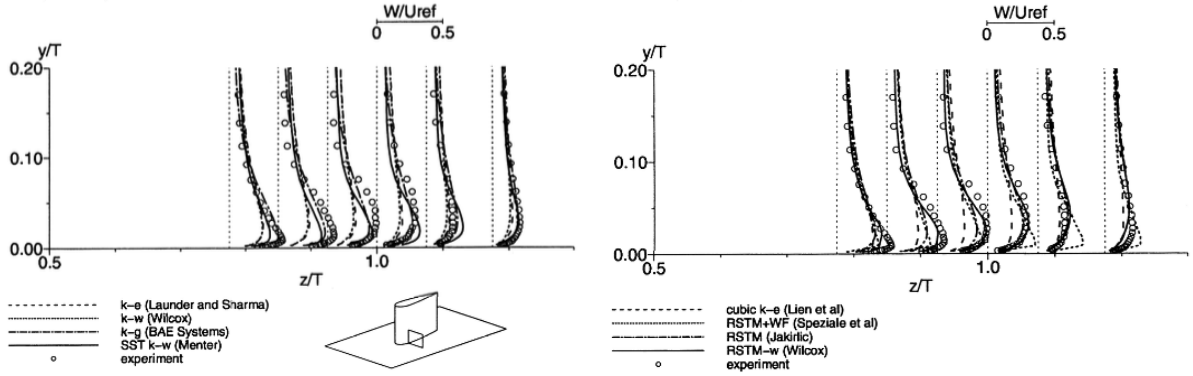

(a) W/U for EVM turbulence models (b) W/U for DSM turbulence models

Figure 2.14: W/U at $x/T = 0.75$ for different turbulence models (Apsley and Leschziner, 2001)

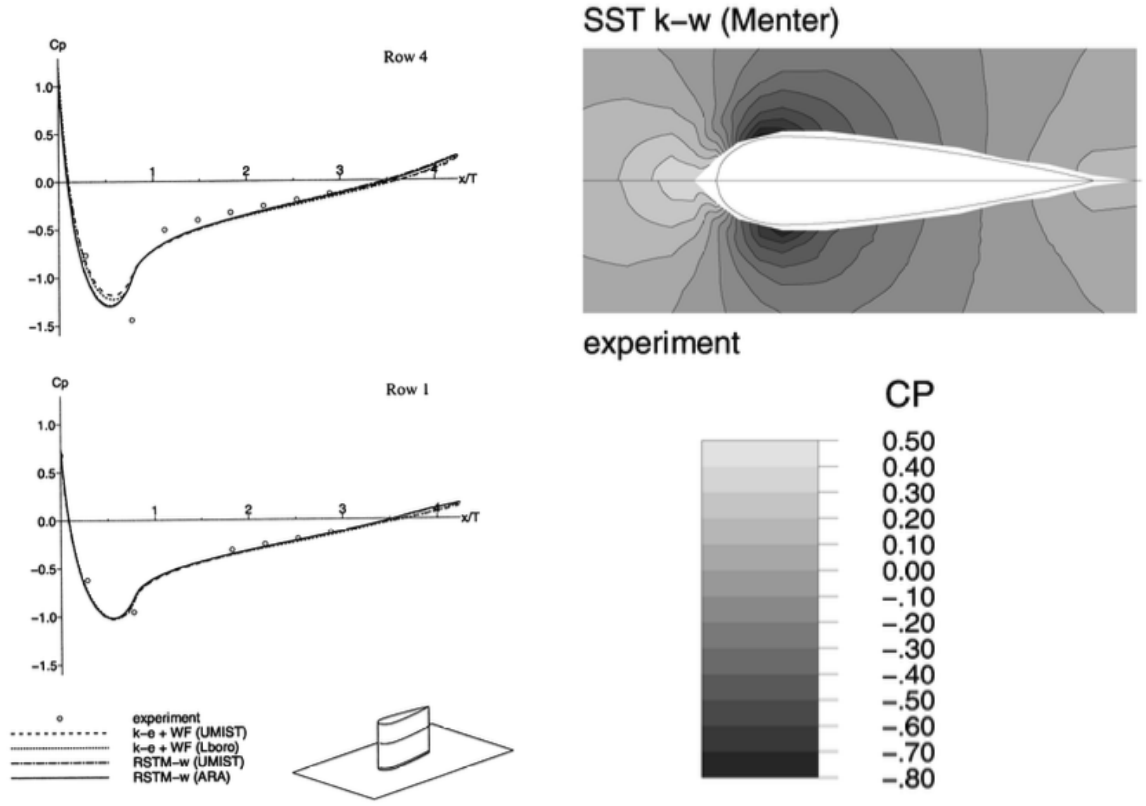

(a) C_p along the wing surface (b) C_p contour at the bottom wall

Figure 2.15: Pressure coefficient along the wing surface and at the bottom wall (Apsley and Leschziner, 2001)

A numerical study comparing results from numerical simulations with different turbulence models was also performed by Jones and Clarke (2005), but here the focus was mostly on the flow structures in front of the wing. Gand et al. (2010) investigated the flow around a wing body junction including both wind tunnel tests and large Eddy simulations (LES). The geometry tested is a NACA0012 wing profile on a flat plate and the Reynolds number is $Re_c = 2.8 \cdot 10^5$. The LES simulations agree fairly well with the experimental data on the simulated mean flow

and second-order statistics around the junction. The LES also capture the behaviour of the horseshoe vortex at the nose of the junction. The strength of the horseshoe vortex suction side leg appears to be underestimated. When comparing the LES results with RANS results, the LES seem to be quite capable simulating these complex 3D turbulent flows.

Methods to Suppress the Secondary Flows

The horseshoe vortex created by the wing junction flow is in most cases undesirable. The vortex can create large scale low frequency unsteadiness which may lead to unwanted vibrations and noise. The vortex also tends to bring high momentum free stream fluid in contact with the surface which gives increases drag and surface shear stresses. The horseshoe vortex may also persist far downstream of the junction which may affect the flow around other objects downstream. Due to these undesirable effects from the horseshoe vortex, attempts to counteract the creation of the vortex in the wing body junction have been performed. W. J. Devenport et al. (1990) tried using a fillet with a fillet radius of 0.53T, shown in Figure 2.16. The results show that the fillet fail to prevent the formation of a horseshoe vortex and unsteadiness related to noise generation. The size and strength of the horseshoe vortex legs along with the unsteadiness in the wake increased.

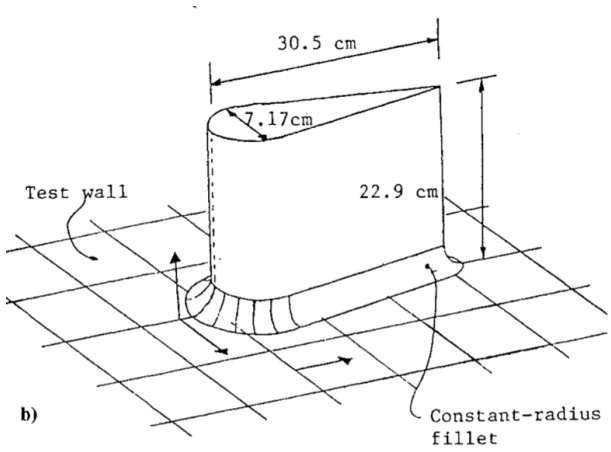

Figure 2.16: Wing body junction with fillet (W. J. Devenport et al., 1990)

In a later study William J. Devenport et al. (1992) introduces a leading edge fillet instead in order to prevent the development of the horseshoe vortex. The air foil wall junction with the leading edge fillet is shown in Figure 2.17. The results are promising and prevent to some extent development of the horseshoe vortex in front of the nose. Vortex legs still develop downstream, but in a smaller magnitude than before.

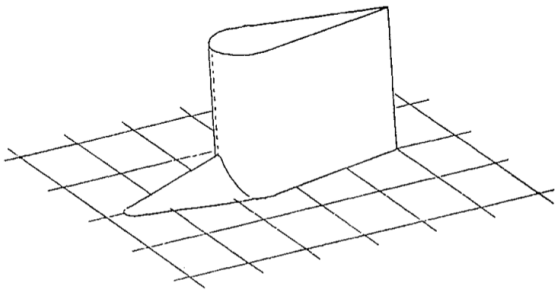

Figure 2.17: Wing body junction with leading edge fillet (William J. Devenport et al., 1992)

With the positive results from William J. Devenport et al. (1992) in mind Theberge and Ekmekci (2017) tested the performance of a triangular leading edge plate at the base of the wing plate junction. The experimental set up is shown in Figure 2.18. The leading edge triangles varied in size and thickness. All the different triangles tested decrease the circulation strength of the horseshoe vortex, but to different degree. Those with higher Reynolds number are large plates needed to keep the same effect on the horseshoe vortex. The thicker plates give worse vortex mitigation, especially at higher Reynolds numbers. Still, generally all the results show that the triangular plate counteract the development of the horseshoe vortex.

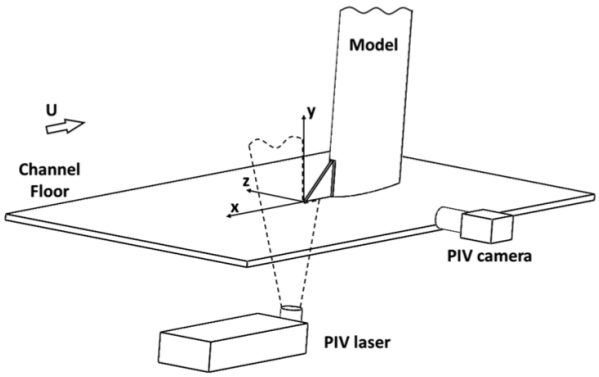

Figure 2.18: Triangular leading edge plate on wing wall junction (Theberge and Ekmekci, 2017)

2.3.4 Simulations using EBRSM Turbulence Model

CFD analysis of several complex flow configurations using the EBRSM turbulence model are presented in Lardeau and Manceau (2014). The most relevant case for the hydrofoil junctions to be tested in this thesis are be the Wing-tip vortex for NACA 0012 with a 10 degrees angle of attack. The configuration is shown in Figure 2.19a. Although clear differences compared to the hydrofoil junctions, some information about the EBRSMs performance on vortex development are highly relevant. The EBRSM model outperforms the two EVMs models in maintaining the tip vortex through the domain and simulates the stream wise velocity on the vortex centerline. This can be seen from the graph in Figure 2.19b.

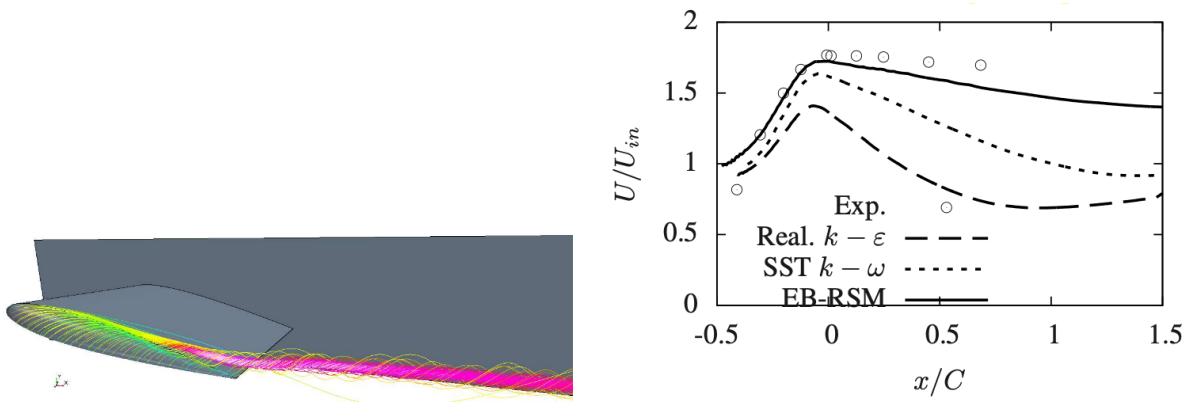

(a) Flow configuration

(b) Streamwise velocity on the vortex centerline

Figure 2.19: Simulations of tip vortex (Lardeau and Manceau, 2014)

Stollinger et al. (2015) applied the EBRSM to different cases. One of the cases tested is the flow around a 2-dimensional NACA 0012 wing profile at a Reynolds number of 10^6. The Reynolds stress model predictions for lift and drag are, similarly to the k-omega SST results presented in Subsection 2.3.1, in close agreement with the experimental values for most angles of attacks. For large angles of attack with flow separation, the EBRSM turbulence model has better agreement with experimental data. Plots of the experimental and CFD results for lift and drag are shown in Figure 2.20a and 2.20b. It should be noted that the simulation were performed with quite low order schemes. Momentum conservation equation discretized by Gamma scheme with 20% upwinding limit and the convective terms in the Reynolds stress and dissipation rate equations are discretized by $1st$ order upwind scheme.

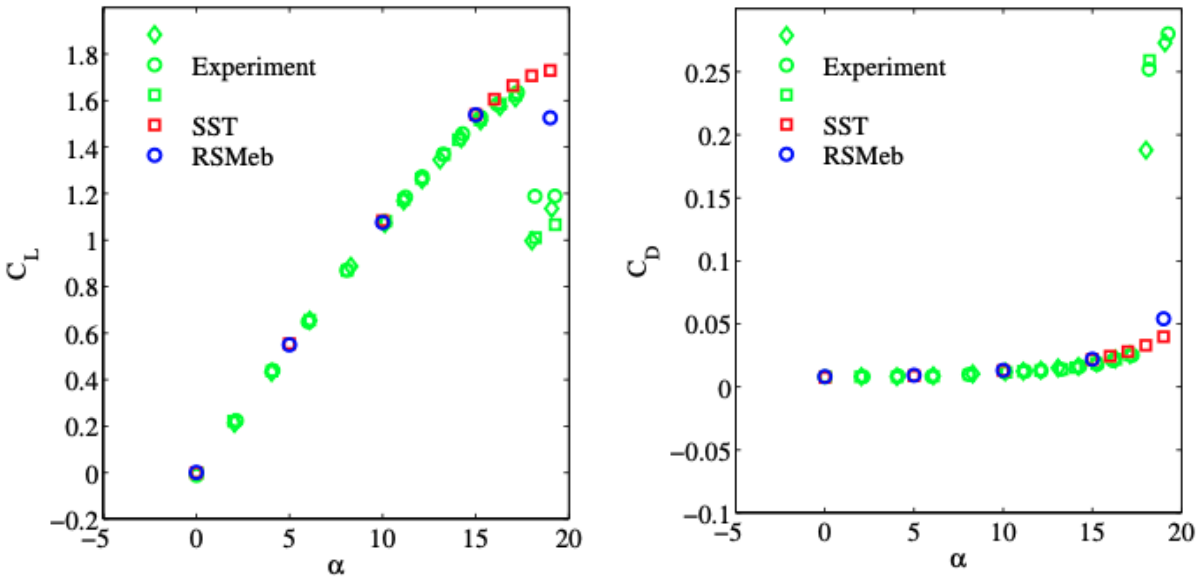

(a) C_L relative to α

(b) C_D relative to α

Figure 2.20: CFD results with EBRSM for NACA 0012 (Stollinger et al., 2015)

Chapter 3

Numerical Tools and Method

3.1 Structural Modelling

In this thesis, the strut-hydrofoil designs are developed by Lift Ocean. However, the structural modeling has been performed for the validation cases, namely the 2D NACA 0012 airfoil and the wing-body junction. To carry out the structural modelling for these cases, the software used is Onshape, which is a free CAD software that operates within a web browser.

After the structural modelling is completed in Onshape, is Blender utilised for further processing. Blender is a free and open-source 3D computer graphics software that offers a wide range of applications. In this particular thesis, Blender is employed for tasks such as marking specific parts of the designs or adding planes, which are subsequently used in the meshing process. To distinguish different parts of the design are various materials are assigned to each component in Blender. This allows for easier identification and manipulation of specific elements during subsequent stages of the analysis. More detailed information about this process can be found in Subsection 3.2.1 of this thesis.

3.2 General CFD Setup

The Computational Fluid Dynamics (CFD) library OpenFOAM is utilised for the simulations. OpenFOAM is a free open source CFD software developed by OpenCFD ltd. The version v2206 was used in this project.

OpenFOAM is a $C++$ toolbox which uses several plain text input files to configure the simulations. The necessary file structure is:

- `system/`
  - `controlDict`
  - `fvSchemes`

  - `fvSolution`
  - `Other dictionaries`
- `constant/`
  - `polyMesh/`
  - `Other dictionaries`
- `0/`
  - `Different field files`

The system folder must contain the `controlDict`, `fvSchemes` and `fvSolution` files. The `controlDict` file controls the simulations and specifies important parameters like simulation time, times step etc. The `fvSchemes` file contains information about numerical schemes for the differential terms in the solution. The `fvSolution` file includes information about the solution algorithms. The constant folder must contain a `polyMesh` folder which contains information about the mesh which is used for the simulations. The other dictionaries which may be included in the constant folder is for instance flow properties. The 0 folder contains the initial conditions of the flow. These can typically include boundary conditions on the velocity and pressure.

By utilising this file structure, OpenFOAM provides a flexible and modular approach for configuring and running CFD simulations, allowing users to customise various aspects of the simulation setup and easily analyse the results at different time steps.

3.2.1 Meshing

The meshing process of all the cases in this thesis are conducted using the integrated meshing in OpenFOAM. This is utilised through dictionary files `blockMeshDict` and `snappyHexMeshDict` located in the system folder described in Section 3.2. The meshing is then based on two main steps. Initially, the background mesh is created with the `blockMeshDict`. Secondly, the mesh is refined in the desired areas and geometry implemented with the help of `snappyHexMeshDict`. SnappyHexMesh creates hexhedra and split-hexahedra meshes and wall layers may be included (OpenFOAM, 2023b). In this thesis are specific parts of interest in the design assigned own patched with the help of Blender. These patches are then loaded by `snappyHexMesh` and used to control layer termination and refinement regions. Refinement planes were also created in Blender and used in `snappyHexMesh` to define refinement regions.

3.2.2 Solver

The OpenFOAM solver used for the steady state CFD analysis is the simpleFoam solver. The simpleFoam solver is a solver for steady state, incompressible and turbulent flows (OpenFOAM, 2022). With simpleFoam being a steady state solver is the time step and end time controls in `controlDict` changed to deciding the number of iterations. OpenFOAM includes two variants of

the SIMPLE algorithm, standard SIMPLE and its consistent formulation, SIMPLEC (Doormaal and Raithby, 1984) . In this study the SIMPLEC algorithm is used which should result in a more robust solution and faster convergence (OpenFOAM, 2023c). The strut-hydrofoil junction design which was just straight T-junction showed unsteady behaviour and hence the transient solver pimpleFoam is utilised. The pimpleFoam solver uses a combination of PISO (Issa et al., 1986) and SIMPLE (Patankar and D. Spalding, 1972) algorithm.

The parameters used for the simpleFoam and pimpleFoam solvers are tabulated in Table 3.1. The run time for the transient simulations are decided based on observing when the forces starts to experience more stable oscillations. Firstly, was a more common approach of defining run time based on the flow velocity and foil length implemented. However, this was seen to be too short for the flow to properly develop. The pimpleFoam solver is run with 50 simple loops for each time step. This is implemented because of stability problems with a Courant number above 4 without the simple loops. For further explanation on Courant number see Subsection 2.2.8. The maximum Courant number of the simulations is 40. The relaxation factors are slightly lower in the simple loops of the pimpleFoam solver than in the simpleFoam simulations. This is because the SIMPLEC algorithm is used in the simpleFoam simulations, which can have larger relaxation factors than the general SIMPLE algortihm which is utilised as part of the transient simulations. The maximum number of iterations for the steady state simulations are either 6000 or 10000 dependent on whether wall function is used or the boundary layer is fully resolved.

Table 3.1: Parameters for each solver

	pimpleFoam	simpleFoam
Simulation time	1 s	6000 or 10000 iterations
Relaxation U	0.3	0.7
Relaxation p	0.3	0.5
Relaxation ω	0.3	0.7
Relaxation k	0.3	0.7
Max Courant number	40	
Max number of simple loops	50	

3.2.3 Numerical Schemes

The numerical schemes employed in OpenFOAM for the convection of turbulence variables utilise the linear upwind scheme. However, for the convective term in the velocity, the scheme LUST (Linear Upwind and Central Difference) is utilised. The LUST scheme combines the characteristics of linear upwind and central difference interpolation, employing a constant blending factor of 0.25 for linear upwind and 0.75 for central difference interpolation.

The decision to use the LUST scheme is based on the results from Kramer and Steen (2021). In the validation study with the 2D NACA 0012, presented in Subsection 4.2.1, are both the more common linear upwind scheme and the LUST scheme utilised. The results showed consistently slightly more accurate results with the LUST scheme. Hence this scheme is used for the final simulations.

The numerical scheme used for the time integration in the transient simulations is Euler scheme. Which is an implicit scheme hence maximum Courant number above 1 may be used, see Subsection 2.2.8.

3.2.4 Turbulence Model

The strut-hydrofoil junctions has, if compared with Pope (2000) examples of turbulent flows of various levels of computational difficulty, three directions of statistical inhomogenity and is statistically stationary. The three directions of statistical inhomgenity arises from the meeting boundary layers between the strut and hydrofoil. This three dimensionality is taken into account when choosing appropriate turbulence model. Eddy viscosity turbulence models has as described in Subsection 2.2.4 problems with properly representing strongly 3-dimensional flows, because they are based on the turbulent viscosity hypothesis. Hence eddy viscosity models are expected to struggle with properly represent the flows close to the corner of the strut-hydrofoil junctions. As Reynolds stress models, also further explained in Subsection 2.2.4, eliminates the need for the turbulent viscosity hypothesis are they expected to perform better in strongly 3-dimensional flows.

In Subsection 2.3.3 are simulations results with different turbulence models from the study by Apsley and Leschziner (2001), presented. The turbulence models are tested on a wing body junction which is also a strongly 3-dimensional flow, similar to that of a strut-hydrofoil junction. Their results showed that the Reynolds stress models seemed to have predictive advantages over the other models, although far from perfect. Out of the eddy viscosity models was it $k-\omega$ SST and $k-g$ models which had the best performance, but they only managed simulating mean flow features.

Based on the simulation results from Apsley and Leschziner (2001) and available turbulence models in OpenFOAM are two turbulence models of interest. The $k-\omega$ SST turbulence model is of interest as it performed reasonably well in the wing body junction flow and best of the eddy viscosity models. It is also a well tested turbulence model, which has proved to be easy to handle. Further explanation of the $k-\omega$ SST turbulence model was given in Subsection 2.2.5. The second turbulence model of interest is the Reynolds stress model EBRSM. The Reynolds stress models showed better ability in capturing details of the flow in Apsley and Leschziner (2001). The EBRSM turbulence models performance in cases with some similarities to the strut-hydrofoil junction and wing body junction were presented in Subsection 2.3.4. The model outperformed the two EVM models tested in maintaining a vortex, while it showed as accurate results as $k-\omega$ SST for a 2D foil section at small angles of attack. EBRSM turbulence model is the newest Reynolds stress model implemented in OpenFOAM. The EBRSM turbulence model is also, as mentioned in Subsection 2.2.6, created to make a more robust and industry friendly RST model than previous models. Difficulty in use has been one of the major issues with Reynolds stress turbulence models, especially related to stability.

In this thesis is both the $k-\omega$ SST and EBRSM turbulence models tested, but large stability problems with the EBRSM model prohibited results to be produced with that model. A thorough investigation into the stability problems was performed by testing different schemes, meshes and

solvers. The only solution which stabilised the solutions was not letting `snappyHexMesh` create layers. This implies that the layer generation process of `snappyHexMesh` was not accurate enough for the EBRSM model. Ashton and Stoellinger (2023) noted that they struggled with numerical instabilities for the EBRSM model with too large stretching of the cells. Therefore decreasing the number of layers could have stabilised the solution, but with a target $y^+ < 5$ was this not feasible with the computational power used in this thesis. Stability problems is also a likely reason for the low order schemes used in Stollinger et al. (2015), commented in Subsection 2.3.4. Because of the stability issues with the EBRSM model is the $k - \omega$ SST turbulence model used for the simulations results presented in this thesis.

3.3 Specific CFD Cases

There are three different CFD cases in this study and their specific set up is explained in this section. The 2D NACA 0012 foil profile and the wing body junction simulations are later used as validation of the numerical simulations. While the strut-hydrofoil junctions are the main simulation cases in this thesis.

3.3.1 2D NACA 0012 Foil Profile

As the simulation results from the 2D NACA 0012 foil profile are compared with the experiments from Charles L. Ladson (1988) is the goal of the structural modelling to get it as similar to the experiments as possible. The NACA 0012 profile, shown in Figure 3.1, is created in Onshape with an open airfoil profile script. Blender is then used to create a finite thickness at the trailing edge of about $2mm$. Making the foil section more realistic as well as helping the meshing at the trailing edge. In Charles L. Ladson (1988) is it not given any thickness of the foil hence it could be slight differences.

The Reynolds number based on chord length of the simulations is 6 million, corresponding to the Reynolds number in Charles L. Ladson (1988). The flow properties used for the simulations are listed in Table 3.2, with units as shown in Nomenclature.

Figure 3.1: NACA 0012 foil profile

Table 3.2: Flow properties of 2D NACA 0012 foil profile

	U	ν	ρ
Value	6.831	$1.14 \cdot 10^{-6}$	999.1

Boundary Conditions

The computational domain for the 2D NACA 0012 simulations are enclosed by the inlet, outlet, top, bottom, front and back. The length and position of the boundaries are shown in Figure 3.2. The domain lengths are defined based on the foil chord length c. The domain is 2-dimensional by creating only one cell into the plane of thickness $1c$.

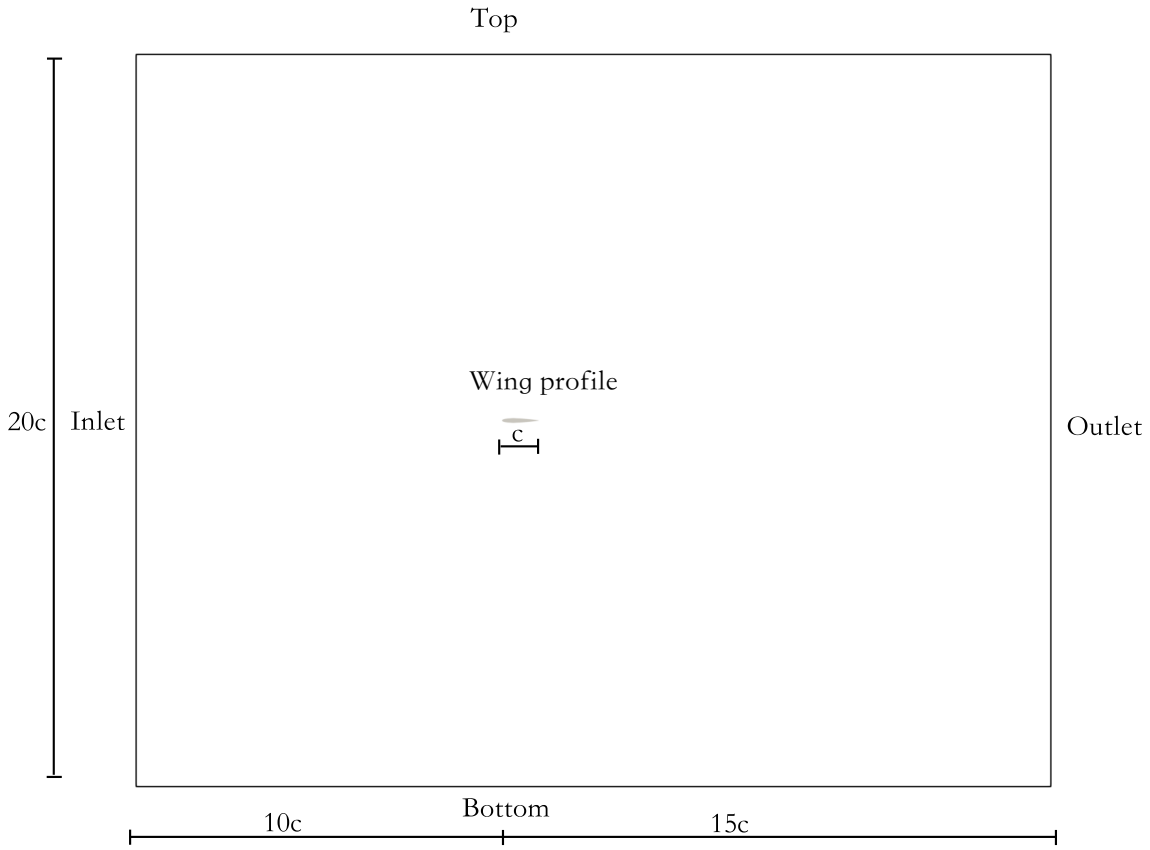

Figure 3.2: Computational domain of the NACA 0012

The boundary conditions of each boundary is tabulated in Table 3.3. The variables U, p, nut, k and omega refers to the fields used in the simulations. U describes the velocity field and is set with no slip conditions at the wing. The velocity is set with the flow velocity at the inlet and zero gradient condition at the outlet. The variable p describes the pressure and is set with a zero gradient at the wing and inlet, while a fixed value is placed on the outlet. The variables nut, k and omega describes the turbulent viscosity, turbulent kinetic energy and specific rate of dissipation, respectively. Continuous wall functions are used for the set up where the boundary layer is not resolved i.e. they can manage cells in the viscous sub-layer and buffer boundary layer mentioned in Subsection 2.2.7. Wall functions are also used when the boundary layer is fully resolved for the same reason, to manage cells outside the viscous sub-layer. The only difference in wall functions is that when the boundary layer is fully resolved is the low Reynolds wall function used for nut. The wall functions for omega are set up with exponential blending. As the domain is 2-dimensional are the boundary conditions on the front and back patches set as empty. The top and bottom patches have slip conditions.

Table 3.3: Boundary conditions for two-dimensional foil with wall functions

	U	p	nut	k	omega
Inlet	fixedValue	zeroGradient	calculated	fixedValue	fixedValue
Outlet	zeroGradient	fixedValue	calculated	zeroGradient	zeroGradient
Wing	noSlip	zeroGradient	nut.[1]	kLowRe.[2]	omega.[3]
Top	slip	slip	slip	slip	slip
Bottom	slip	slip	slip	slip	slip
Front	empty	empty	empty	empty	empty
Back	empty	empty	empty	empty	empty

[1] nutkWallFunction or nutLowReWallFunction

[2] kLowReWallFunction

[3] omegaWallFunction

Meshing

The main meshing parameters of the 2D NACA 0012 case are tabulated in Table 3.4. They are divided into simulations with wall functions and with resolved boundary layer (BL). The parameters of the mesh are the utilised values after the convergence study presented in Subsection 4.1.1. Hence the approximate number of cells is very influenced from the results of the convergence study. The background cell size is set to not be too coarse so it would influence the results, but neither be too small which would greatly increase the number of cells. Therefore, the simulations with wall function have more total cells than with resolved boundary layer which contrary to the usual trend. The feature cell size is important to be small enough to capture the details of the flow changes along the foil chord. The wake cell size is decided in order to get the details of the wake behind the foil section. Trailing edge cells size is set low enough to get enough cells one the thickness of the trailing edge to capture it. The values are to a large extent based upon the simulation parameters for the 2D foil in Kramer et al. (2018), with some adjustments.

Table 3.4: Parameters for meshing of 2D NACA 0012

Parameter name	2D wing with wall func.	2D wing resolved BL
Background cell size / c	0.08	0.14
Feature cell size / c	0.002	0.0011
Wake refinement cell size / c	0.01	0.018
Trailing edge cell size / c	0.00015	0.00028
Number cells between layers	5	5
Number of wall layers	5	15
Layer expansion	1.3	1.3
Target y^+	60	1
Approx. number of cells	250 000	120 000

In Figure 3.3 is specific parts of the mesh for the 2D NACA 0012 foil profile shown. The wake

refinement is defined as a box which stretches from 1c in front to 6c behind the leading edge of the foil section and 1c above and below the nose-tail line, shown in Figure 3.3a. Figure 3.3b show the meshing near the wing profile and Figure 3.3c shows the meshing at the trailing edge. The further refinement at the trailing edge and termination of layers are done by assigning a different material to the trailing edge as well as a plane through it, in Blender, which is later used by `snappyHexMesh`. This process was further explained in Subsection 3.2.1.

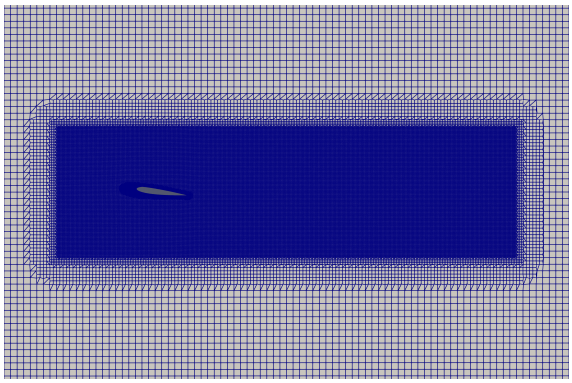

(a) Overview of the refinement

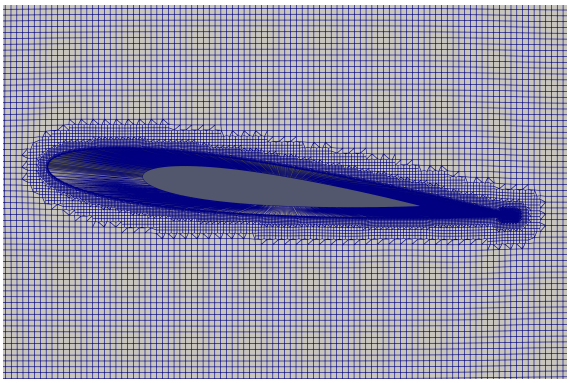

(b) View of foil profile

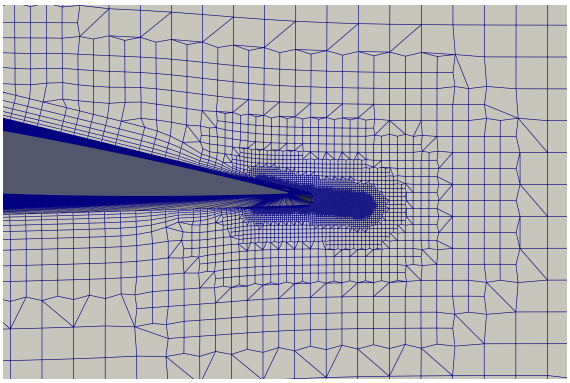

(c) View of trailing edge

Figure 3.3: Illustrations of the different parts of the mesh for 2D NACA 0012 foil profile

3.3.2 Wing Body Junction

The wing body junction validation case is compared with the experimental results from Fleming et al. (1993), hence the wing shape is a replication of the experiments. The 3:2 elliptic nose with a NACA 0020 tail joined at the widest point, shown in Figure 3.4, is created with Onshape by the help of coordinates of a NACA 0020 profile from airfoil tools (Airfoiltools, 2023). The tail is slightly altered afterwards with Blender to create a finite thickness at the trailing edge of about 2 mm. Simulations are run for both fully resolved boundary layer and with wall functions in accordance with the explanation in Subsection 2.2.7.

The flow properties in the experiments by Fleming et al. (1993) had certain deviations between different measurements. However, the flow properties in this thesis is maintained stable through every simulation and are tabulated in Table 3.5.

Figure 3.4: 3:2 elliptic nose with NACA 0020 tail

Table 3.5: Flow properties of wing body junction

	U	ν	ρ
Value	27.606	$1.691 \cdot 10^{-5}$	1.089812

Boundary Conditions

The patches enclosing the computational domain of the wing body junction can be seen in Figure 3.5. In Figure 3.6 is the position of the boundaries when looking from the top shown. The lengths are defined based on the maximum thickness of the wing profile. The height of the domain, which is not included in Figure 3.5, is 3T. Positioning of the inlet relative to the leading edge of the wing profile and the parameters of the wing profile corresponds to the experiment by Fleming et al. (1993). The position of the other boundaries corresponds with the set up from the numerical study by Apsley and Leschziner (2001) presented in Subsection 2.3.3.

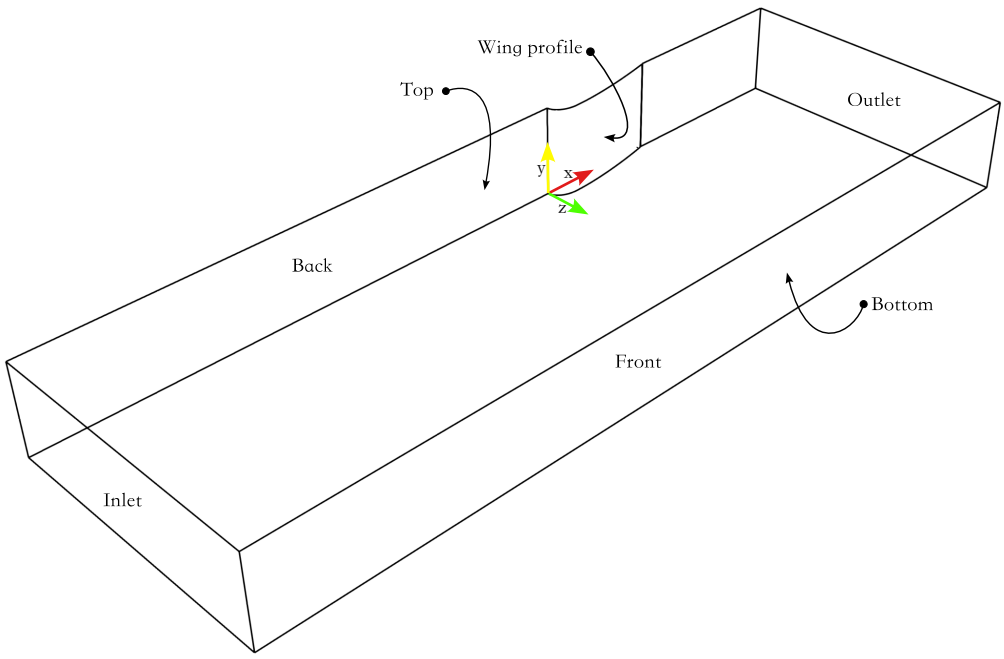

Figure 3.5: Isometric view of the domain for wing body junction

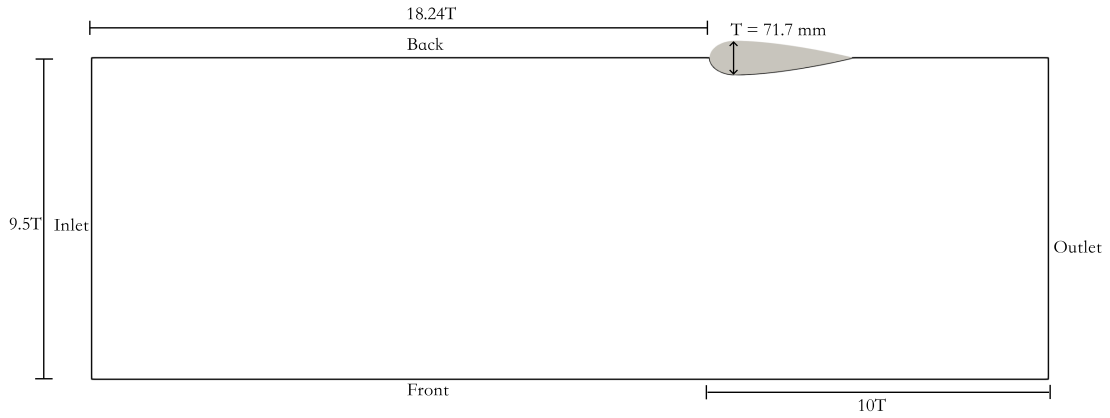

Figure 3.6: Top view of domain of wing body junction

The boundary conditions used for the different patches in the simulations are tabulated in Table 3.6. The symmetry of the experiment by Fleming et al. (1993) is taken advantage of through a `symmetryPlane` conditions at the back patch. The inlet is set with the OpenFOAM boundary condition `timeVaryingMappedFixedValue`, which is used to introduce the inflow conditions from Fleming et al. (1993). The top patch is set with zero-stress boundary conditions which is not the same as the experiments by Fleming et al. (1993), but equal Apsley and Leschziner (2001). In the experiment by Fleming et al. (1993) was a gap left between the top of the wing and the wind-tunnel ceiling to prevent formation of a second junction vortex. While in the numerical simulations by Apsley and Leschziner (2001) was it not a gap between the wing and the top wall, instead slip conditions of the top wall were introduced. The wall patches, Wing profile and Bottom were specified with no slip conditions. The turbulence parameters were set with continuous wall functions. The nut wall functions were changed between `nutkWallFunction` or `nutLowReWallFunction` depending on whether the boundary layer was not fully resolved or fully resolved.

Table 3.6: Boundary conditions for wing body junction

	U	p	nut	k	omega
Inlet	timeVar.[1]	zeroGradient	calculated	fixedValue	fixedValue
Outlet	zeroGradient	fixedValue	calculated	zeroGradient	zeroGradient
Wing	noSlip	zeroGradient	nut.[2]	kLowRe.[3]	omega.[4]
Top	slip	slip	slip	slip	slip
Bottom	noSlip	zeroGradient	nut.[3]	kLowRe.[3]	omega.[4]
Front	zeroGradient	fixedValue	calculated	zeroGradient	zeroGradient
Back	symmetry.[5]	symmetry.[5]	symmetry.[5]	symmetry.[5]	symmetry.[5]

[1] timeVaryingMappedFixedValue

[2] nutkWallFunction or nutLowReWallFunction

[3] kLowReWallFunction

[4] omegaWallFunction

[5] symmetryPlane

Meshing

The main meshing parameters for the wing body junction are shown in Table 3.7. They are divided into two columns, simulation with wall functions and simulations with fully resolved boundary layer (BL). The tabulated values are the chosen values after the mesh convergence study in Subsection 4.1.1. The background cell size, feature cell size, wake refinement cell size and trailing edge cell size are based on the same reasoning as described in the meshing part of Subsection 3.3.1.

Table 3.7: Parameters for meshing of wing body junction

Parameter name	Wing body with wall func.	Wing body resolved BL
Background cell size / c	0.06	0.1
Feature cell size / c	0.008	0.0085
Wake refinement cell size / c	0.008	0.0085
Trailing edge cell size / c	0.002	0.0043
Number cells between layers	5	5
Number of wall layers	3	15
Layer expansion	1.1	1.3
Target y^+	60	1
Approx. number of cells	3 mill.	3 mill.

Illustrations of the mesh are shown in Figure 3.7. In Figure 3.7a the mesh is shown on the top boundary patch. A refinement box is stretching $0.15m$ (half a chord length) in front and on the side of the wing until the end of the domain. The red square corresponds to the positioning of the cut plane illustration of the mesh shown in Figure 3.7b. In Figure 3.7c is the mesh from the back patch of the domain shown. It can be seen that a refinement zone is stretching from the inlet of the domain all the way to the outlet of the domain. With a width in z-direction of $0.15m$ and a height of $0.01m$. This refinement zone is to ensure that the boundary layer thickness of the bottom wall is correctly represented at the position of the wing profile.

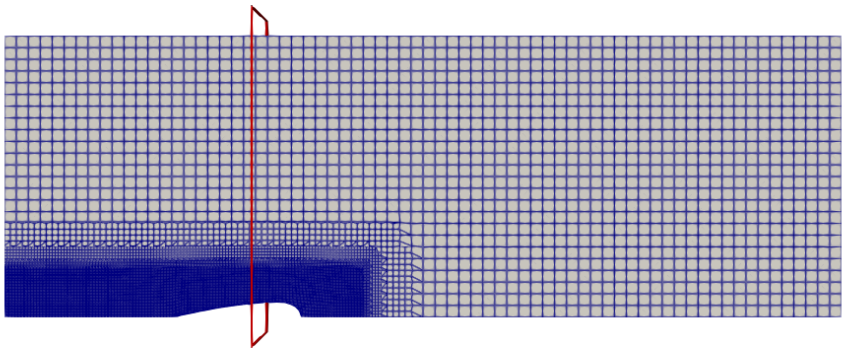

(a) Top view

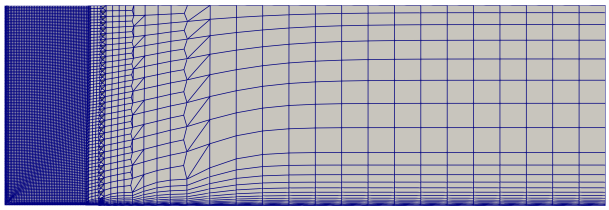

(b) Mesh cut plane

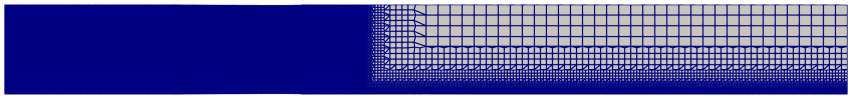

(c) Back view

Figure 3.7: Mesh from top, cut plane and back view

In Figure 3.8, a perspective view of the wing is presented. The boundary layers are depicted, and it can be observed that they terminate at the 90° corner, as indicated by the example shown just in front of the leading edge of the wing profile. The decision to terminate the layers at the corner was made to avoid creating highly skewed cells by keeping the layers through the corner.

However, even with the termination of the layers in the corner, some skewed cells are still present in that region. Skewed cells refer to cells in the computational mesh that have distorted or elongated shapes, which can potentially affect the accuracy of the simulation results.

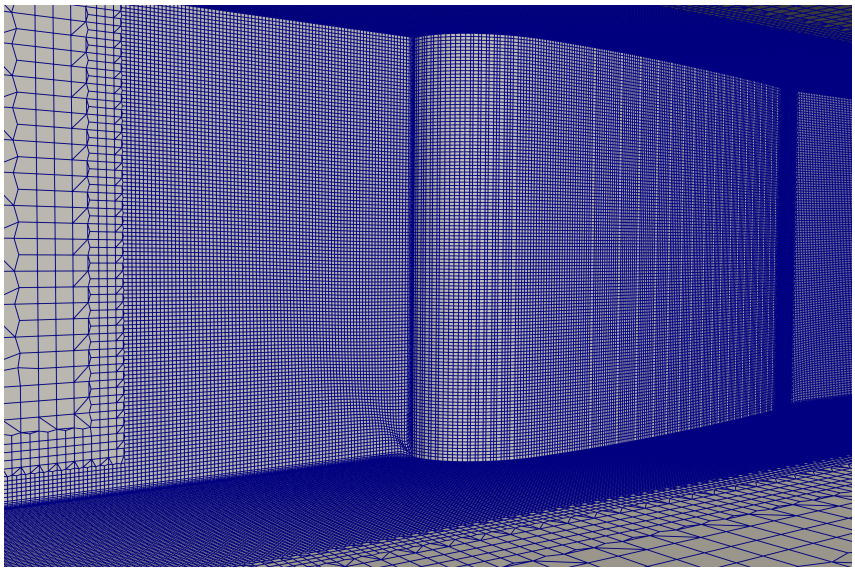

Figure 3.8: Perspective view of the wing meshing

3.3.3 Strut-Hydrofoil Junctions

The strut-hydrofoil junctions are, as mentioned in the introduction, designed by Lift Ocean. The designs are generic designs rather than designs which are used by Lift Ocean. Still, the designs are created quite close to a strut-hydrofoil design which could have been used in order to make it realistic. The different designs of the strut-hydrofoil junctions are shown in Figure 3.9, 3.10 and 3.11. The length of the strut and chord length is $1.5m$ for all the designs with a taper ratio of 0.28. The tip and the root chord of the foil is $0.1m$ and $0.36m$, respectively. These dimensions are shown in Figure 3.9b. The strut hydrofoil design with a fillet has a fillet radius of $0.042m$, which is equal to the strut thickness. The width of the bulb is $0.1m$ and the length at the longest point is $0.6m$ presented in Figure 3.11a and 3.11b, respectively.

The flow properties used in the simulations of the strut-hydrofoil junctions are tabulated in Table 3.8.

Table 3.8: Flow properties of strut-hydrofoil junction

	U	ν	ρ
Value	12.86	$1.14 \cdot 10^{-6}$	999.1

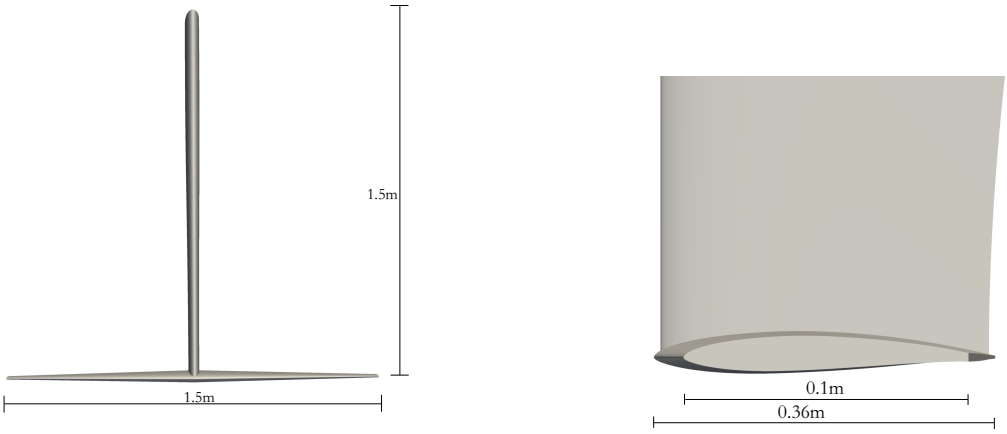

(a) Front view (b) Side view

Figure 3.9: Dimensions design of plane T-junction

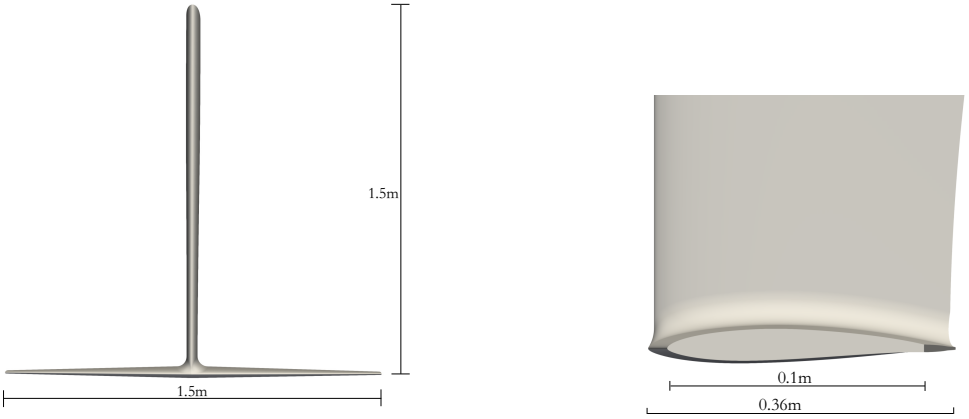

(a) Front view (b) Side view

Figure 3.10: Dimensions design of T-junction with fillet

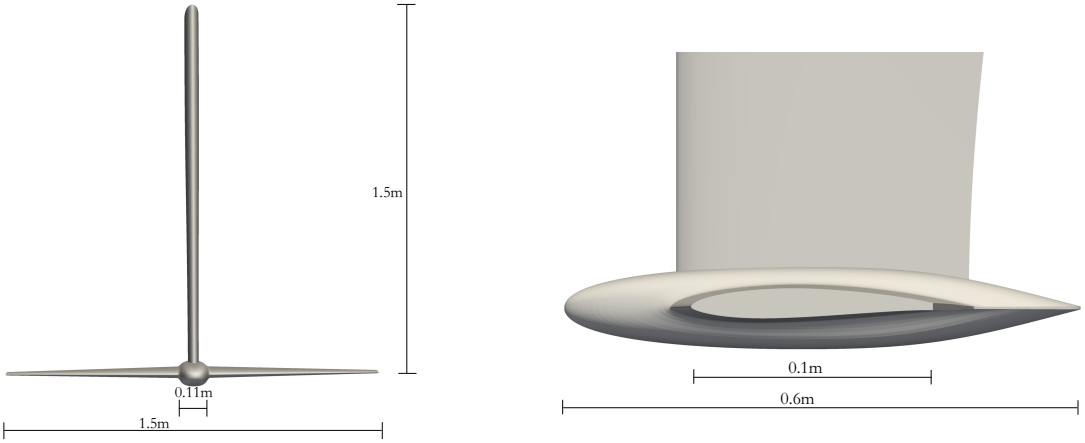

(a) Front view (b) Side view

Figure 3.11: Dimensions design of T-junction with bulb

Boundary Conditions

The computational domain of the strut-hydrofoil junctions can be seen in Figure 3.12. The given lengths are based on the constant c which is the root chord of the plain T-junctions, shown in Figure 3.9, and is equal to $0.36m$. The width and height of the domain is $10c$, while the length of the domain is $23c$. From the inlet to the hydrofoil it is $10c$, and $13c$ from the hydrofoil to the outlet. The domain is enclosed by the inlet, outlet, front, back, top and bottom patches.

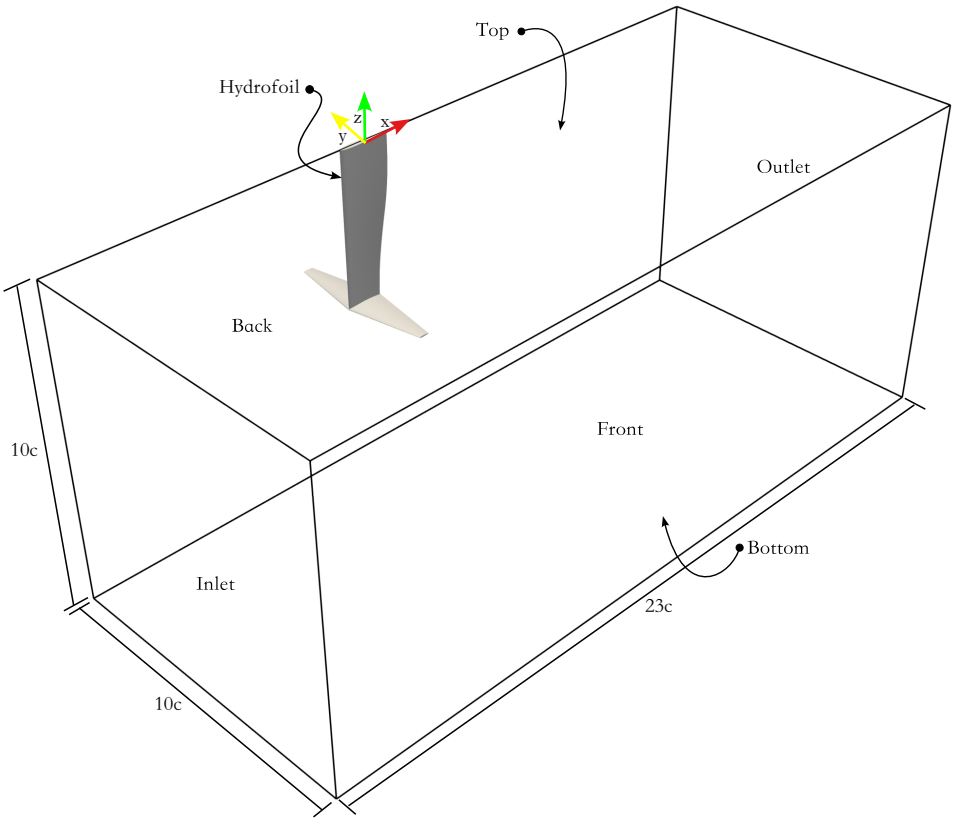

Figure 3.12: Isometric view of the domain for Strut-hydrofoil junction

The boundary conditions corresponding to each of the strut-hydrofoil domain patches are tabulated in Table 3.9. It can be seen that the back patch is given a symmetry plane condition, similar to the wing body junction, to take advantage of the symmetry of the problem. This reduces the needed size of the computational domain and hence the computational time. The inlet and outlet are set up similar to the 2D NACA 0012 case and the walls of the domain have slip conditions. The hydrofoil is set with no slip conditions on velocity, zero gradient on pressure and wall functions on the turbulence parameters. The wall functions used are the same as used in the 2D NACA 0012 and wing body junction cases when not fully resolving the boundary layer.

The decision to run the case with wall functions instead of fully resolving the boundary layer is based on the observation of very similar results obtained with wall functions and resolving the

boundary layer for the wing body junction validation case. This finding will be further explained and demonstrated in Section 4.2. By comparing the results obtained using wall functions with those obtained by fully resolving the boundary layer, it was observed that the differences between the two approaches were minimal. This suggests that employing wall functions provides an accurate representation of the flow behaviour in the boundary layer without the need for the computational cost associated with fully resolving it.

Table 3.9: Boundary conditions for strut-hydrofoil junctions

	U	p	nut	k	omega
Inlet	fixedValue	zeroGradient	calculated	fixedValue	fixedValue
Outlet	zeroGradient	fixedValue	calculated	zeroGradient	zeroGradient
Hydrofoil	noSlip	zeroGradient	nut.[1]	kLowRe.[2]	omega.[3]
Top	slip	slip	slip	slip	slip
Bottom	slip	slip	slip	slip	slip
Front	slip	slip	slip	slip	slip
Back	symmetry.[4]	symmetry.[4]	symmetry.[4]	symmetry.[4]	symmetry.[4]

[1] nutkWallFunction
[2] kLowReWallFunction
[3] omegaWallFunction
[4] symmetryPlane

Meshing

The main meshing parameters for the simulations of strut-hydrofoil junction chosen after the mesh convergence study in Subsection 4.1.1 are tabulated in Table 3.10. The cell size is relative to c which is the same root chord length as used in Figure 3.12 of $0.36m$. The mesh is slightly coarser than the 2D NACA 0012 calculations due to limited computational resources. The background cell size, feature cell size, wake refinement cell size and trailing edge cell size are based on the same reasoning as described in the meshing part of Subsection 3.3.1.

Table 3.10: Parameters for meshing of strut-hydrofoil junction

Parameter name	Strut-Hydrofoil junction
Background cell size / c	0.14
Feature cell size / c	0.0043
Wake refinement cell size / c	0.0173
Trailing edge cell size / c	0.0011
Number cells between layers	5
Number of wall layers	4
Layer expansion	1.3
Target y^+	60
Approx. number of cells	14 mill.

Figure 3.13 show illustrations of different parts of the mesh for the strut-hydrofoil junction design with bulb. The same `snappyHexMesh` parameters have been used for the straight T-junction and the fillet design, so the only difference is the geometry. In Figure 3.13a is the mesh shown from the back patch in accordance with Figure 3.12. There is a refinement region based on the distance from the hydrofoil as well as a refinement box stretching behind the foil as a wake refinement. Figure 3.13b shows the trailing edge of the bulb from the same back view. The trailing edge is more refined than the other parts which is done by assigning an own material and running a refinement plane through the trailing edge in Blender. This is also done for the trailing edge of the wing profile which is shown in Figure 3.13d. Figure 3.13c shows an isometric view of the hydrofoil from inside the mesh. There it can be seen how there is further refinement at the connection between the strut and hydrofoil and the leading edge of the wing profile. This was specified in the meshing process by letting the level of refinement increase by up to two levels in places with large curvature which helped to capture details and not deform these regions. There were some issues with getting `snappyHexMesh` to create layers along the whole wing profile. Hence, the layering process is changing a little for the strut-hydrofoil cases by including a relatively new feature in `snappyHexMesh` where adding the layers are divided into different parts. The layering process is here divided into three parts which solved the problem with layers terminating too early.

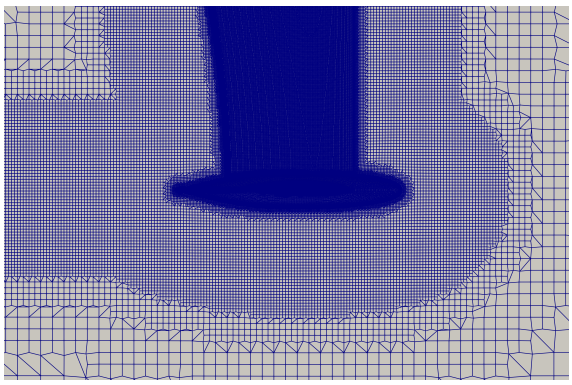

(a) Back View

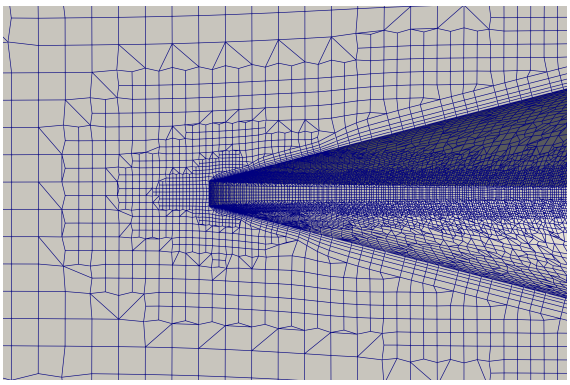

(b) Back view of trailing edge

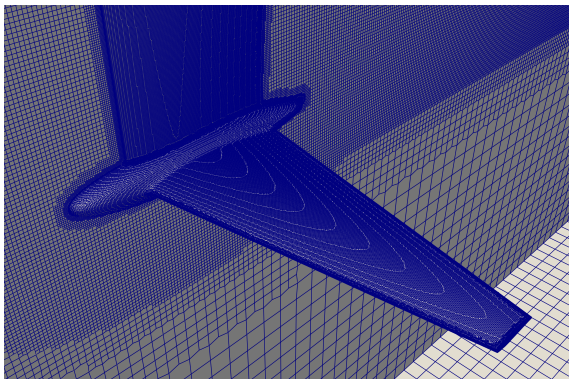

(c) Isometric view inside mesh

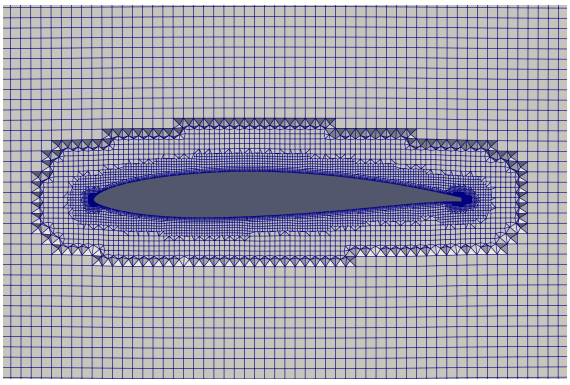

(d) Wing profile view

Figure 3.13: Illustrations of the different parts of the mesh for strut-hydrofoil junction

3.4 Computational Resources

The computational resources which are used changed during the thesis. In the beginning is two Intel Xenon Gold 6146 CPU with a total of 24 cores used. Then later in the study are a AMD EPYC 7543 32-Core Processor utilised, in order to get more computational power. The OpenFOAM simulations are run in parallel on a maximum of 20 and 30 cores as using every core could create issues with the machine. The meshing process is decomposed using the simple method, while the simulations are decomposed using the scotch method. The scotch method attempts to minimise the number of processor boundaries.

3.5 Post-Processing

Post-processing of the simulation results from OpenFOAM are done with both Paraview and Matlab. Paraview is used for visualisation of the results with the geometry while Matlab is used for plotting graphs. An example of the post processing code in Matlab is shown in Appendix B.

Chapter 4

CFD Verification and Validation

4.1 Uncertainty Analysis

The uncertainty is estimated using the general procedure recommended for convergence studies in International Towing Tank Conference (2017). These procedures are strongly based on the work presented in Eça et al. (2010). In this study an unstructured mesh is utilised which leads to variability in the meshes. Therefore, the least square approach is used for the uncertainty analysis. The least squares method requires at least four solutions to perform an initial curve fit of Equation 4.1.

$$S_i = S_0 + \alpha h_i^p \tag{4.1}$$

Where i is the grid number from 1 to the number of grids. S_i, S_0 and h_i are the simulation value, converged simulation result and grid size ratio, respectively. From the initial curve fit the value for S_0, α and p is found. The converged condition is then determined based on the observed order of accuracy, p. With $p > 0$ indicating monotonic convergence and $p < 0$ indicating monotonic divergence. Oscillatory convergence is defined as being when the solution is alternately above and below the converged simulation result.

For monotonic convergence, if the value of p is between 0.5 and 2 after the initial curve fit with Equation 4.1, is the initial curve fit kept as the model function. If the value of p is larger than 2 then the model equation is switched to Equation 4.2. If the value of p is less than 0.5 then the best fit of Equation 4.2 and 4.3 is used. The relative error of the simulations can then be calculated as $\delta_i = (S_i - S_0)/S_0$. The numerical uncertainty is calculated with $U_i = F_S|\delta_i|$, where F_S is a safety factor, which is recommended by ITTC to be 1.25 for a good fit between data and the model. With a good fit defined as $0.5 \leq p < 2.1$. For all other p values should a safety factor of 3 used.

$$S_i = S_0 + \alpha h_i^2 \tag{4.2}$$

$$S_i = S_0 + \alpha_1 h_i + \alpha_2 h_i^2 \tag{4.3}$$

For oscillatory convergence is the simulation error simulated in accordance with Equation 4.4 and 4.5. The numerical uncertainty is again calculated using $U_i = F_S|\delta_i|$, with a safety factor $F_S = 3$.

$$S_0 = Mean(S_i) \tag{4.4}$$

$$\delta = \left(\frac{\max(S_i) - \min(S_i)}{\frac{h_n}{h_1} - 1} \right) / S_0 \tag{4.5}$$

The ITTC procedure for convergence studies is implemented in Matlab and the code can be seen in Appendix B.

4.1.1 Mesh Convergence

In this study, varying the mesh resolution is performed differently depending on whether the boundary layer is fully resolved or not. The approach varies based on the target value of the dimensionless wall distance, denoted as y^+.

For simulations with a fully resolved boundary layer, where the target y^+ value is set to 1, the cell length at each level in the mesh is adjusted by the same factor. No other modifications are made to the mesh, resulting in a decrease in y^+ with increasing mesh refinement and vice versa. A mesh refinement factor of square root of two is used in the mesh convergence study.

On the other hand, for simulations where the boundary layer is not fully resolved, with a target y^+ value of 60, the thickness of the inner wall layer is kept constant. This is achieved by using a mesh refinement factor equal to the wall layer expansion ratio. When changing the mesh refinement, one layer is either added or removed while maintaining the constant thickness of the inner wall layer. In this thesis, a wall layer expansion rate of 1.3 is used, and the same expansion ratio is employed for the mesh refinement factor in cases using wall functions.

The reason for employing different methods for fully resolved and not fully resolved boundary layers lies in the understanding that a lower y^+ value generally leads to more accurate solutions in fully resolved cases. However, in cases utilising wall functions, a decrease in y^+ may result in the first cell being located within the buffer layer, which can lead to less accurate solutions. Further explanation on this topic can be found in Subsection 2.2.7.

2D NACA 0012 Foil Profile

The mesh convergence study for the 2D NACA 0012 with wall functions are shown in Figure 4.1. The mesh convergence is performed at an angle of attack of 6.09 degrees. The lift, plotted in

Figure 4.1a, has oscillatory convergence. Hence the the uncertainty is just a straight line. The analysis of the mesh influence on drag is shown in Figure 4.1b. With these graphs in mind is the default cell length chosen as: Surface cell length / chord = 0.0024. This gives an estimated mesh uncertainty just under 3 percent for the lift coefficient and just under 2 percent for the drag.

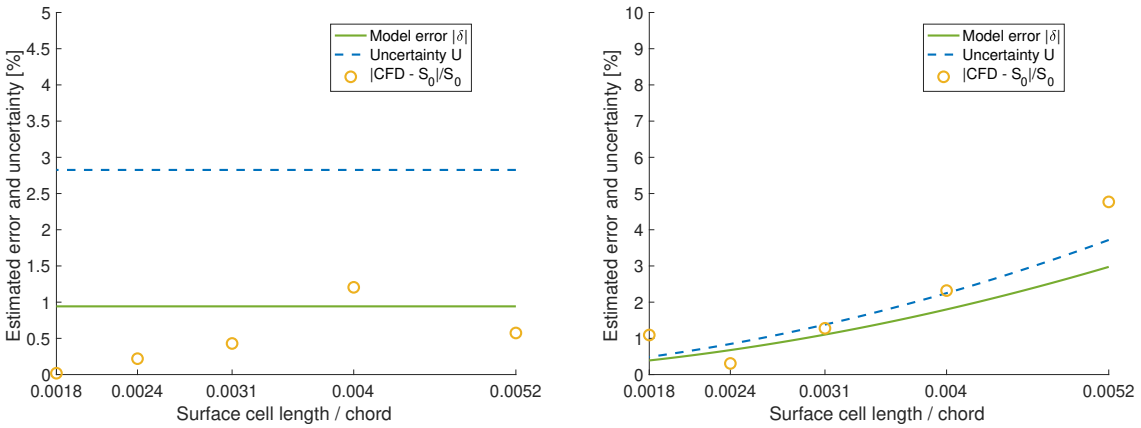

(a) Lift coefficient C_L (b) Drag coefficient C_D

Figure 4.1: Mesh convergence study for NACA 0012 2D with wall functions

In Figure 4.2 is the mesh convergence for the 2D NACA 0012 with a resolved boundary layer shown. Both the lift in Figure 4.2a and the drag in Figure 4.2b have monotonic convergence. Based on the plots is a mesh refinement of: Surface cell length / chord = 0.0011 chosen. This results in an estimated mesh uncertainty of about 3 percent for the lift coefficient and about 1 percent for the drag coefficient.

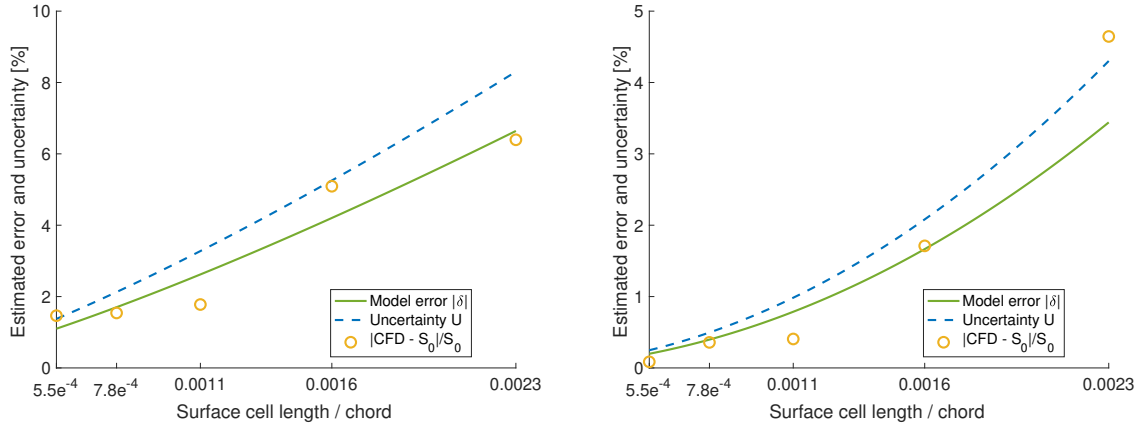

(a) Lift coefficient C_L (b) Drag coefficient C_D

Figure 4.2: Mesh convergence study for NACA 0012 2D without wall functions

Wing Body Junction

The uncertainty related to the mesh size for the wing body junction is estimated based on 4 different refinement levels. The minimum pressure coefficient along the wing surface at $y/T = 0.13279$ is the evaluated value. It is the pressure value along the wing surface which is closest to the corner in the experiment by Fleming et al. (1993). The mesh convergence study is conducted for the simulations with fully resolved boundary layer and is shown in Figure 4.3. Based on the graph is the chosen mesh resolution for further analysis: Surface cell length / chord = 0.0085. For the simulations with wall functions was it experienced difficulties with getting a proper mesh convergence study without lowering the y^+ value too low. Hence these simulations are assumed converged based on comparison with the results from computations with fully resolved boundary layer. This comparison is shown in Figure 4.8, which shows very good correlation of the results with wall function and resolved boundary layer.

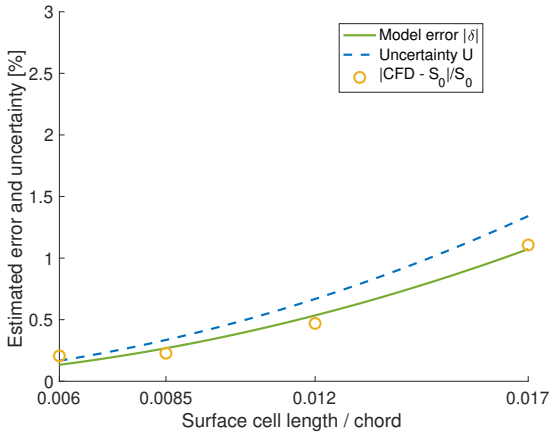

Figure 4.3: Mesh convergence study for wing body junction

Strut-Hydrofoil Junctions

The mesh convergence for the Strut-hydrofoil junctions are done based on the convergence of the total lift and total drag of the designs. The straight T-junction design showed as mentioned in Subsection 3.2.2 unsteady behaviour and hence had to be run with transient simulations. Due to limitations in time and computational power is neither a full mesh convergence study nor a time step convergence study performed. This is not optimal, however the mesh convergence study of the two other strut-hydrofoil designs, presented underneath, should be a good indication towards needed mesh refinement of this design. Also, results for the three middle refinement levels used in the convergence study for fillet and bulb is presented in the results, Section 5.1.

The uncertainty related to the mesh for the strut-hydrofoil junction with a fillet is presented in Figure 4.4. Based on the convergence graphs for lift and drag is a surface cell length / chord = 0.0043 chosen for further simulations. This gives an estimated mesh uncertainty of approximately 1 percent for lift and 3 percent for drag.

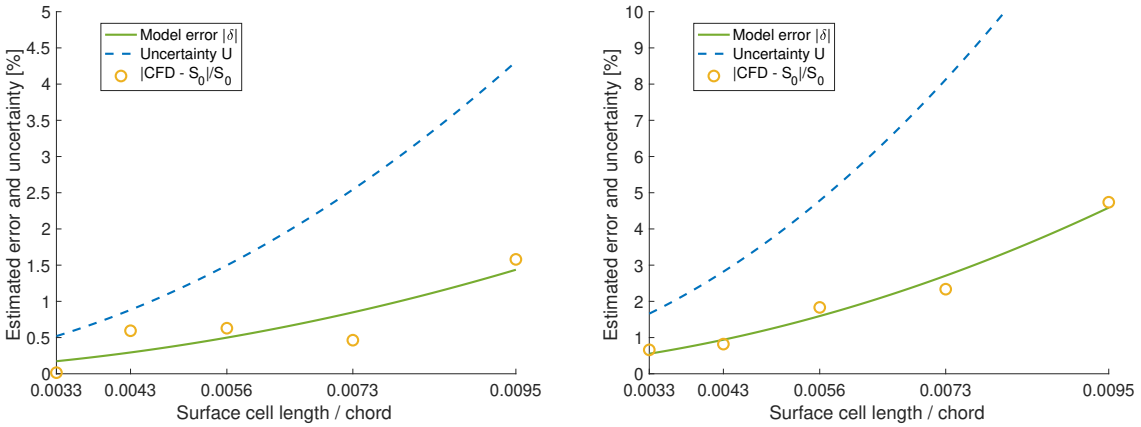

(a) Lift force (b) Drag force

Figure 4.4: Mesh convergence study for strut-hydrofoil junction with fillet

In Figure 4.5a and 4.5b are the mesh convergence of lift and drag for the hydrofoil-strut junction with a bulb presented. From the convergence graphs is it chosen a mesh refinement which gives: surface cell length / chord = 0.0043. Resulting in a mesh uncertainty of about 2 percent for the lift and 2.5 percent for drag.

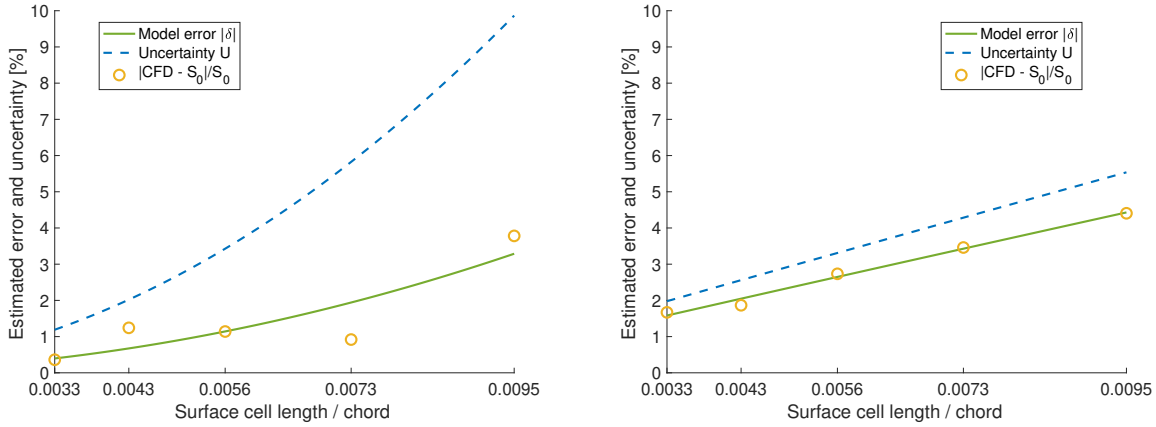

(a) Lift force (b) Drag force

Figure 4.5: Mesh convergence study for strut-hydrofoil junction with bulb

4.2 Validation Results

In the literature study section (Section 2.3), it is mentioned that there is a limited availability of publicly available validation cases specifically focused on strut-hydrofoil junctions. Due to this limitation, the focus of this thesis has been shifted to the aeronautical industry, where more literature is available.

To gain insights into the accuracy and limitations of the numerical setup used for the strut-hydrofoil simulations, two different cases have been selected as validation cases: the 2D NACA

0012 foil profile and the wing-body junction. Although these cases differ from the strut-hydrofoil junction, they provide valuable information about the performance and limitations of the numerical model.

The 2D NACA 0012 foil profile serves as a validation for the calculated lift and drag forces along the wing span of the hydrofoil, as well as the pressure distribution along the chord length of a wing section. By comparing the simulated results with experimental data, the expected accuracy of the calculated forces can be assessed.

The wing-body junction simulations, on the other hand, are used as a validation for the accuracy of flow representation in the vicinity of the corner of the strut-hydrofoil junctions. This area is of particular interest due to the interference between the meeting boundary layers. The pressure distributions and flow patterns obtained from the simulations will be compared with experimental data to evaluate the accuracy of the numerical model in capturing these features.

While neither the 2D NACA 0012 case nor the wing-body junction case directly replicate the conditions of a strut-hydrofoil junction, together they provide valuable insights into the accuracy and limitations of the numerical setup used in the simulations. These validations help in assessing the reliability of the results obtained from the strut-hydrofoil simulations.

4.2.1 2D NACA 0012 Foil Profile

In Figure 4.6, the results of CFD simulations are compared with experimental data obtained from Charles L. Ladson (1988). The experimental data used for comparison were based on a NACA0012 airfoil tripped with 80 grit, as shown in Figure 2.9. The percentage difference between the CFD simulations and the experimental results, plotted in Figure 4.6, is tabulated in Table 4.1 and 4.2.

The CFD simulations are categorised into three cases:

1. Resolved boundary layer with LUST scheme
2. Wall function with LUST scheme
3. Wall function with linear upwind scheme

The distinction among these cases lies in the treatment boundary layer treatment as mention in Subsection 2.2.7 and treatment of the convective term in the velocity, mentioned in Subsection 3.2.3.

Overall, all three CFD simulations exhibit relatively close agreement with the experimental results for the lift coefficient, particularly at 4 and 6 degrees angle of attack. However, at 2 degrees angle of attack, there is a slightly greater difference between the CFD simulations and the experimental data. When comparing the simulations with and without fully resolved boundary layer using the LUST scheme, they demonstrate very similar agreement with the experimental results for the lift coefficient. On the other hand, the lift coefficient results from

simulations using the linear upwind scheme deviate slightly further from the experimental results for every angle of attack.

The simulation results for the drag coefficient exhibit more disagreement to the experimental results compared to the lift, particularly at higher angles of attack. One noticeable difference is that the simulations consistently show a larger increase in drag relative to lift compared to the experimental results. One hypothesis for the discrepancy was that cutting the trailing edge had slightly altered the geometry of the airfoil. To test this hypothesis, simulations were performed without creating a finite thickness at the trailing edge. However, the resulting drag curve was similar to the simulations with finite thickness, suggesting that the trailing edge modification was not the cause of the deviation. Another explanation for the difference in drag at high angles of attack could be the mesh being too coarse which might move the position of flow separation forward. When performing the mesh convergence study, both for the case with resolved boundary layer and without, where the drag coefficient decreasing with further refinement. Too course mesh could hence explain some of the deviation between the experimental results and CFD simulations. The results from the CFD simulations presented in Figure 2.11 Subsection 2.3.1 also show larger deviations on drag between CFD and experiment at higher angles of attack, but it is smaller deviation and at larger angles of attack.

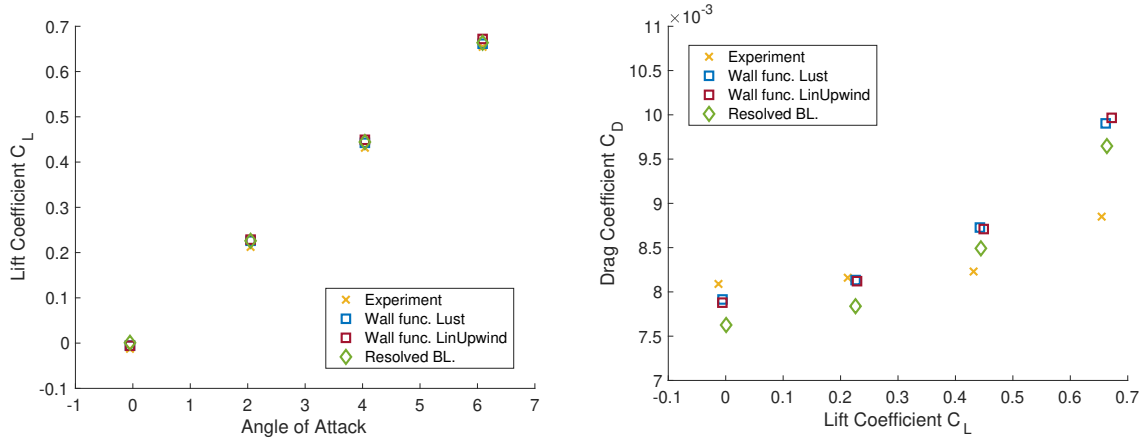

(a) Lift coefficient C_L relative angle of attack α

(b) Drag coefficient C_D relative to C_L

Figure 4.6: Plot of lift and drag coefficient for NACA0012 at different angles of attack

Table 4.1: Percent difference of C_L between CFD and experiment

Parameter name	$\alpha = 2.05$	$\alpha = 4.04$	$\alpha = 6.09$
Wall function LUST	6.2	2.5	1.1
Wall function linear upwind	7.3	4.0	2.6
Without wall function	6.2	2.9	1.4

Table 4.2: Percent difference of C_D between CFD and experiment

Parameter name	$\alpha = -0.05$	$\alpha = 2.05$	$\alpha = 4.04$	$\alpha = 6.09$
Wall function LUST	-2.2	-0.3	5.9	11.2
Wall function linear upwind	-2.7	-0.5	5.7	11.9
Without wall function	-5.9	-4.0	3.1	8.6

Figure 4.7 show comparison of the pressure distribution along the wing chord between the CFD simulations and the experimental data presented in Figure 2.10. The results are at an angle of attack of 0 degrees. The CFD results and experimental data exhibit very close agreement in terms of the pressure distribution. However, there is a slight discrepancy at the leading edge of the airfoil profile, where the experimental data shows slightly higher pressure compared to the CFD simulations. This correlation with the larger drag observed in the experimental results at 0 degrees angle of attack suggests that the leading edge behaviour might play a role in the drag discrepancy between the simulations and experimental data.

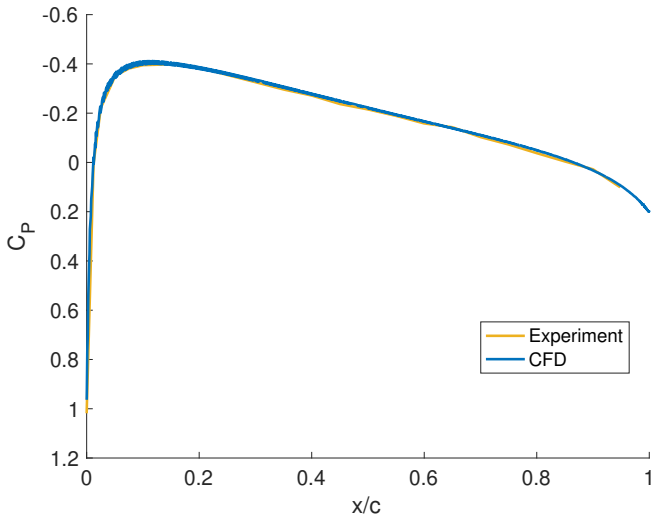

Figure 4.7: Comparison between CFD and experiment for Pressure coefficient C_p at $\alpha = 0$

4.2.2 Wing Body Junction

In this section, the CFD simulations for the wing-body junction are compared with the experimental results conducted by Fleming et al. (1993). It is important to note that deviations between the simulation results and experimental data are expected, as indicated by the literature study in Subsection 2.3.3.

The literature study presented in Subsection 2.3.3 included two studies that utilised RANS simulations: Apsley and Leschziner (2001) and Jones and Clarke (2005). Both of these studies demonstrated clear deviations between the experimental data and the simulation results. However, some of the turbulence models tested were able to simulate the mean flow feature. Among them the $k - \omega$ SST model which is used for the results presented in this section.

In Figure 4.8, the pressure coefficient (C_p) along the wing surface for the wing-body junction is presented. The plots correspond to different y positions, starting from the bottom wall along the wing, as defined in Figure 3.5. The comparison includes experimental results as well as CFD simulations with wall functions and resolved boundary layer. The CFD results with wall functions and resolved boundary layer, as mentioned in Subsection 4.1.1, exhibit a good correlation with each other. However, when comparing the CFD results with the experimental data, a larger discrepancy is observed. Specifically, the position of the minimum pressure point is consistently further forward in the CFD results for each plot at different y values. Additionally, the experimental measurements indicate lower minimum pressure at every position except at $y/T = 0.13279$.

The difference between the experimental and CFD results of the shape and minimum value for the pressure coefficient curve are similar to the findings of Apsley and Leschziner (2001) using the $k-\omega$ SST turbulence model, as presented in Subsection 2.3.3 Figure 2.15a. Interestingly, the discrepancy between the CFD simulations and the experimental data increases as the distance from the corner increases. This behaviour was also observed in the simulations performed by Apsley and Leschziner (2001). They determined that these results were not due to grid-dependent solutions and concluded that the most likely cause was the difference between the simulation and experimental flow conditions at the top boundary. In the experiments was a gap left between the top of the wing and the upper tunnel wall, while in the simulations is the wing extended to touch the upper surface. This explanation was later deemed unlikely by Jones and Clarke (2005) as the difference in pressure profile between CFD and experiment are similar $y/T = 1.4607$ and $y/T = 1.7263$.

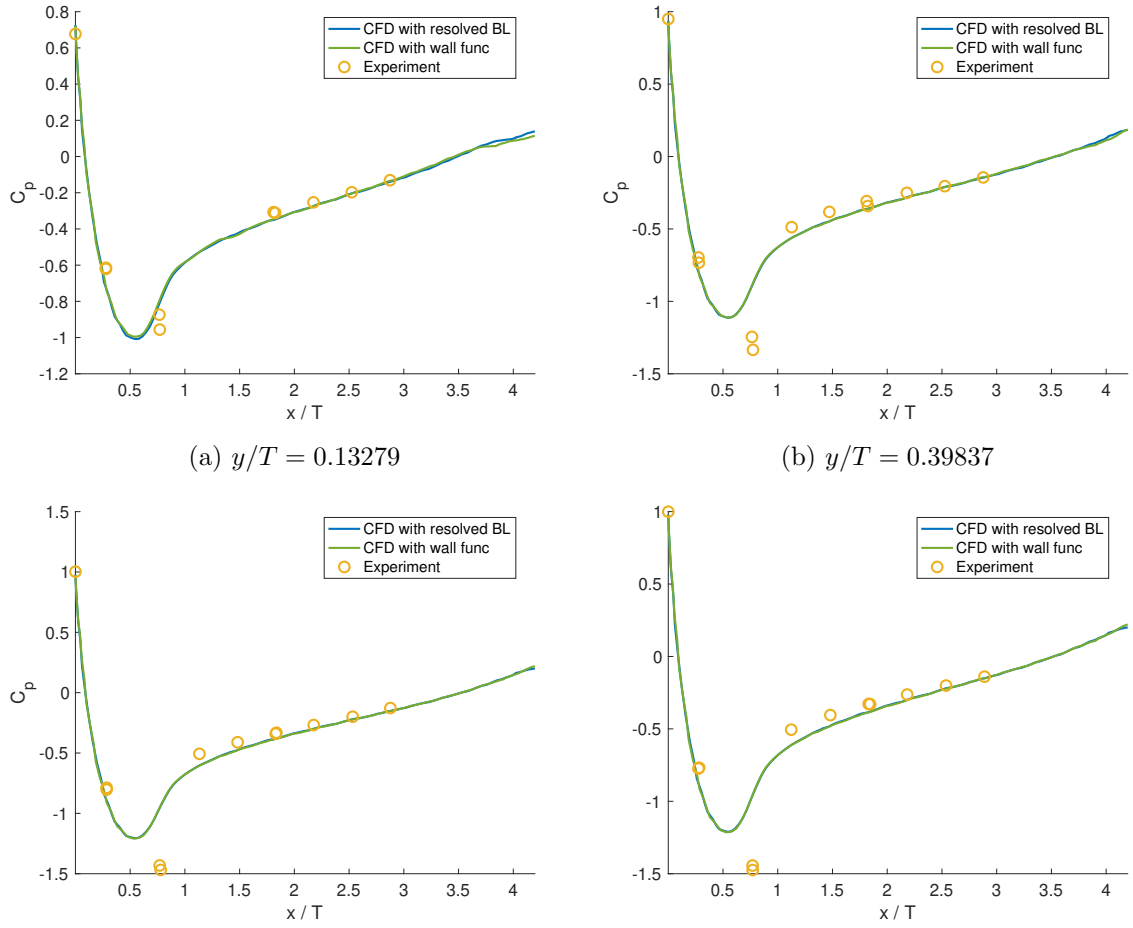

(a) $y/T = 0.13279$

(b) $y/T = 0.39837$

(c) $y/T = 1.4607$

(d) $y/T = 1.7263$

Figure 4.8: Comparison between CFD and experiments of the pressure coefficient C_p at different points along the wing chord on the wing wall

In Figure 4.9, are contour plots of the pressure coefficient (C_p) on the flat plate where the wing is mounted displayed. The experimental results are shown in Figure 4.9a, while the CFD simulations are presented in Figure 4.9b.

The contour plots demonstrate a close agreement between the CFD simulations and the experimental data, particularly in the middle of the wing profile. However, there are some differences observed at the nose and tail regions. Similar to what was observed in Figure 4.8, the lowest pressure point is slightly further forward in the CFD simulations compared to the experimental data. This behaviour aligns with the findings of Apsley and Leschziner (2001), as presented in Figure 2.15b in Subsection 2.3.3.

Another discrepancy between the simulation results in this study and the experimental data from Fleming et al. (1993) is the shape difference in the pressure contour ahead of the low-pressure point. This shape difference was not observed to the same extent in the simulations conducted by Apsley and Leschziner (2001), suggesting a potential grid dependency. It is worth noting that Apsley and Leschziner (2001) used a more structured mesh compared to the unstructured mesh employed in this study. As mentioned in the meshing section of Subsection 3.3.2, some skewed

cells were created in the corner, which may have influenced the results. Apsley and Leschziner (2001) also tested more turbulence models showing that the sensitivity of the junction pressure field to turbulence modelling is weak.

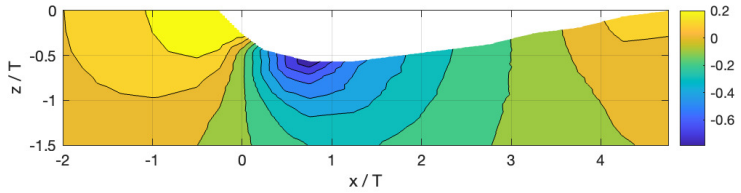

(a) C_p experiment

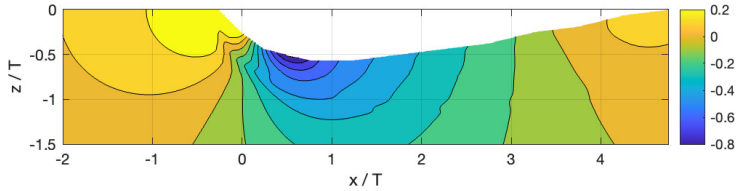

(b) C_p CFD

Figure 4.9: Contour plot of the pressure coefficient at the bottom wall $y = 0$ for experiment and CFD simulations

In Figure 4.10, profile plots of the secondary flow (W) are presented. These results are obtained from the z-y plane located at $x/T = 0.75$ or $x/C = 0.18$, as referenced in Figure 2.13. This position corresponds to the widest point of the wing surface and is close to the point of minimum pressure.

As explained in Subsection 2.3.3 is the dominating flow characteristic of the wing body junction the mean secondary flow structure known as the horseshoe vortex. The experiments by Fleming et al. (1993) show elliptical shape of the horseshoe vortex flow, with $\partial W/\partial Y$ creating the main component of the stream wise vorticity. Hence the secondary flow plots give an indication of the simulations accuracy in representing the corner vortex.

Clear differences are observed between the secondary flow patterns obtained from the simulations and the experimental results. While the general shapes of the graphs are relatively similar, the peak values are both underestimated and overestimated depending on the position in the plane. When comparing the plots of different z positions is it no clear indication that the secondary flows are worse represented close to the wing profile, rather the opposite is the case. The secondary flow results in Figure 4.10 show close similarity with the $k - \omega$ SST results in Figure 2.15a by Apsley and Leschziner (2001). Hence the difference between simulations and experiment are likely due to limitations in the numerical model used rather than mistakes in the numerical set up.

Additional plots of the secondary flow can be found in Appendix A, providing further insights into the representation of the secondary flow in the wing-body junction.

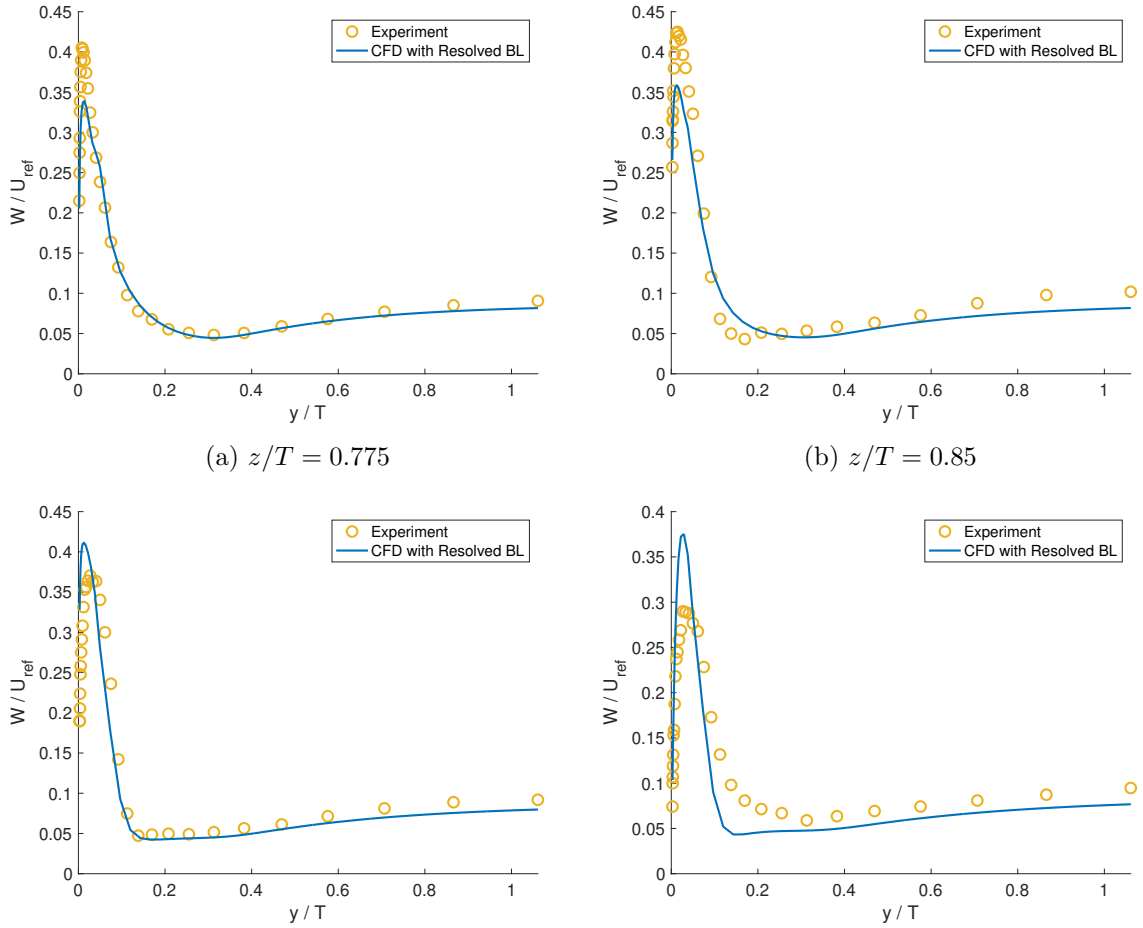

(a) $z/T = 0.775$

(b) $z/T = 0.85$

(c) $z/T = 0.925$

(d) $z/T = 1$

Figure 4.10: Comparison between CFD and experiments of the secondary flow W/U_{ref} at $x/T = 0.75$

The simulated results for the primary flow U, at same the z-y plane located at $x/T = 0.75$, are presented in Figure 4.11. Presented is the comparison between CFD and experiments of the velocity profiles at the points closest to the wing. The CFD simulations are plotted against the velocity profile measured in the experiments by Fleming et al. (1993).

There are clear differences in the velocity profiles especially at the points of abrupt change in the gradient of the flow profile. These abrupt changes coincide with the peak of the secondary flow shown in Figure 4.10 which is due to the vortex motion of the fluid. Hence the simulations show to have problems correctly representing the corner vortex.

Additional plots of the primary flow is included in Appendix A, providing more insight into the flow details further away from the wing profile.

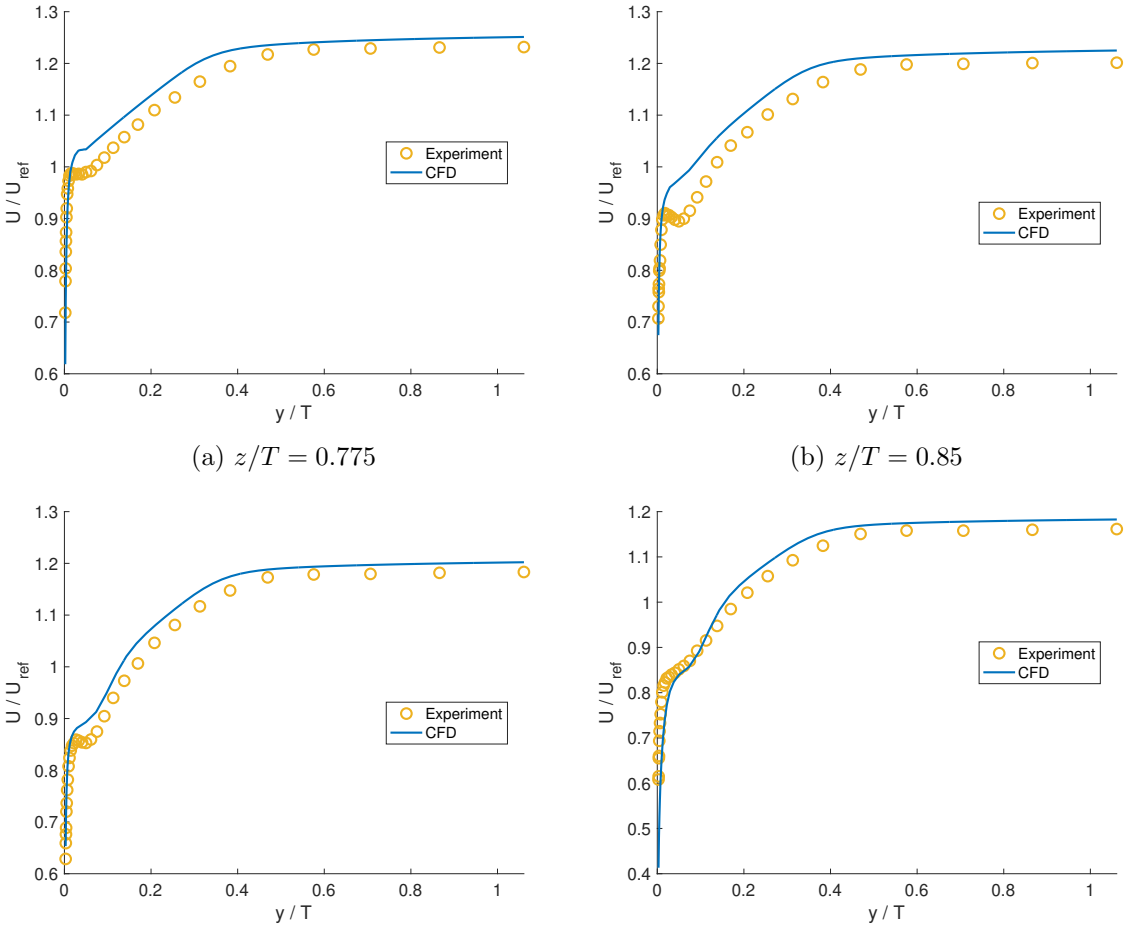

(a) $z/T = 0.775$ (b) $z/T = 0.85$

(c) $z/T = 0.925$ (d) $z/T = 1$

Figure 4.11: Comparison between CFD and experiments of the secondary flow U/U_{ref} at $x/T = 0.75$

In Figure 4.12, contour plots of the primary flow U in a cross-flow plane located at $x/T = 4.46$ (corresponding to $x/C = 1.05$ in Figure 2.13) are presented. The point is just behind the foil profile and the flow features should hence be influenced by the upstream development. Figure 4.12a displays the experimental results from Fleming et al. (1993), while Figure 4.12b shows the results from the CFD simulations in this study.

Comparison of the two figures show that the CFD simulations overestimates the the boundary layer thickness coming from the corner. Similar behaviour was seen for the $k-\omega$ SST simulations in Apsley and Leschziner (2001), pointing to the turbulence model causing the difference to experimental results. The $k-\omega$ SST turbulence model which is employed in these results cannot resolve anisotropy and has been specifically developed and calibrated to handle adverse pressure gradients that induce separation. That the $k-\omega$ SST turbulence model is rather too sensitive at provoking separation is a quite typical remark from simulations. The overestimation of the boundary layer thickness in the corner indicates a potential overestimation of the interference drag, as the interference is a results of boundary layer thickening from meeting boundary layers. Both the experimental results and simulations show a thickening of the boundary layer at $z/T \approx 1$, which is attributed to the transverse vortex motion lifting the boundary layer fluid toward

the free stream (Apsley and Leschziner, 2001).

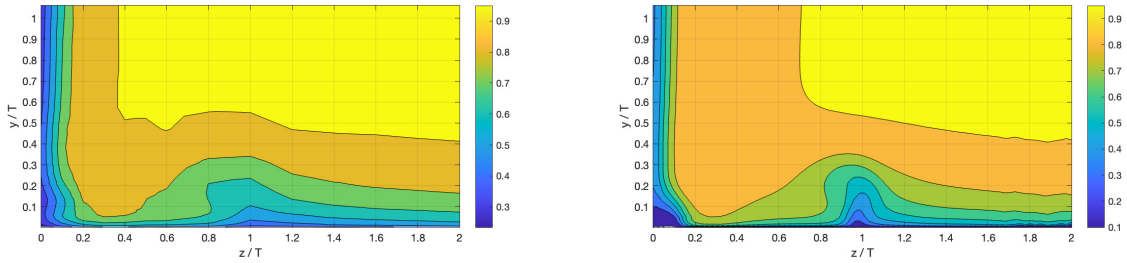

(a) U/U_{ref} experiment

(b) U/U_{ref} CFD

Figure 4.12: Contour plot of the axial mean velocity U/U_{ref} in a cross flow plane at $x/T = 4.46$ for experiment and CFD simulations

4.2.3 Concluding Thoughts from the Validation Study

In this validation study, the objective was to assess the accuracy and limitations of simulations for strut-hydrofoil junctions. The results for 2D NACA 0012 foil profile simulations indicated reasonably good accuracy for lift, with most results showing less than a 5 percent difference from experimental data. However, there was slightly more deviation in the drag results, especially at larger angles of attack. Since the strut-hydrofoil junction has a 0 angle of attack, the results were deemed acceptable.

For the wing body junction simulations, the focus was on the pressure distribution and flow representation near the corner of the strut-hydrofoil junction. The simulations indicated that the lowest pressure points on the wing body junction were slightly more forward on the wing profile compared to experimental results. This suggests that the location of the lowest pressure point in the strut-hydrofoil junction cannot be expected to be entirely accurate. Additionally, the simulations slightly underestimated the minimum pressure value on the wing profile. These inaccuracies in the pressure field at the corner are expected to impact the evaluation of cavitation inception for the strut-hydrofoil junctions. However, these differences were not significant and are likely to be more pronounced in the straight T-junction design.

One notable problem identified in the simulations was the incorrect representation of the corner vortex in terms of its position and strength. As mentioned, is the $k - \omega$ SST turbulence model not able to resolve anistropy. Therefore, the simulations are not expected to accurately represent every flow detail in the junction between the strut and hydrofoil, but rather to predict the mean flow features.

Overall are the simulations demonstrating reasonably good accuracy for lift and drag of a wing profile, and mean flow features in a corner. There are some limitations of the representation of the flow details in the corner especially regarding the corner vortex.

Chapter 5

Results and Discussion

The simulation results for three three strut-hydrofoil designs are presented in this chapter. As described in Subsection 3.3.3 are symmetry condition used for all the designs. Hence the forces presented in this chapter will be half of those for the whole strut-hydrofoil designs. All the forces and plot positions are defined in accordance with the coordinate system included in Figure 3.12.

5.1 Strut-Hydrofoil Junction with Straight T-junction

The results of the mean forces, on the strut hydrofoil junction with straight T-junction, relative to time is presented in Figure 5.1. The plotted time is from $0.35s$ to $1s$. Where $0.35s$ is chosen based on then the force oscillations started showing repeating behaviour and $1s$ in order to cover some oscillations. From the graph, it appears that the simulations may have required additional runtime to fully capture the behaviour of the forces. However, due to limited computational resources, extending the simulations beyond $1s$ was not feasible.

The total forces are plotted for the three middle refinement levels used in the convergence studies of the strut-hydrofoil designs with fillet and bulb. The orange plot of; surface cell length / chord = 0.0043 corresponds to the chosen mesh resolution of the fillet and bulb simulations. The dotted line is the mean forces over plotted time for this mesh resolution. Refinement of the mesh does not show a clear correspondence with smaller oscillations. The coarsest mesh clearly has largest oscillations, but the finest mesh has larger oscillations than the mesh with one level coarser mesh. There is a significant jump in mean lift force (9 percent) from the middle refinement level to the finest refinement level, which indicates a considerable sensitivity to mesh resolution. Unfortunately, further mesh refinement was not possible due to computational limitations. Considering this, the uncertainty associated with the total forces due to the mesh is likely substantial.

The force plots makes the unsteadiness of the flow quite clear through the changing oscillations. This unsteadiness correlates well with the theory of corner flows presented in Subsection 2.3.2. Corner flows has shown difficulty in describing as results of complicated flow pattern due to merging of the boundary layers with high sensitivity to the experimental set up. Hence it is not

surprising that the results are very unsteady and show large mesh sensitivity.

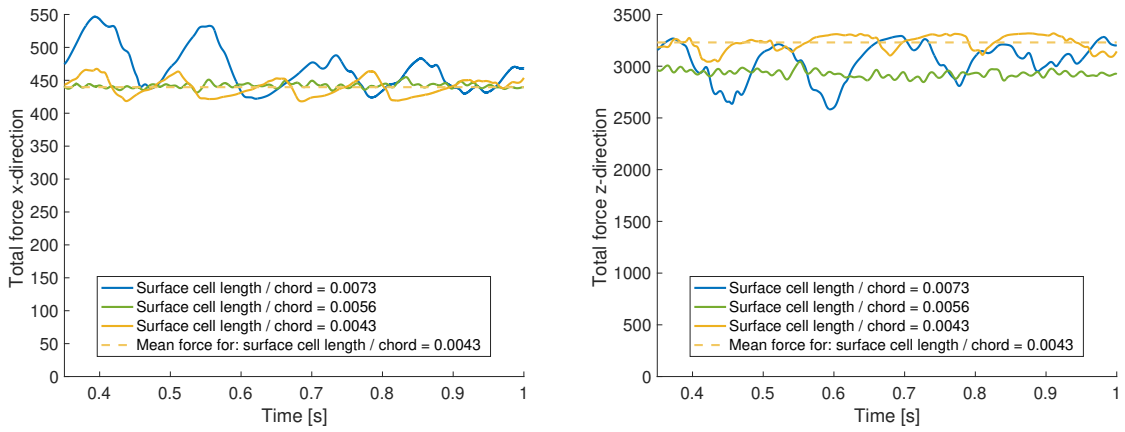

(a) Total drag force

(b) Total lift force

Figure 5.1: Total forces from $t = 0.35s$ to $t = 1s$ for transient simulations

In Table 5.1 are the different force components together with the lift and drag coefficients tabulated. Further explanation of theory behind these components, see Subsection 2.1.2. The forces are divided into a pressure and a viscous component. The lift and drag coefficients are calculated based on the projected area of the bottom hydrofoil. It can be seen that the viscous force is the main part of the resistance, accounting for 65 percent of the total resistance. While the pressure force accounts for 35 percent of the total resistance. The total lift and drag values gives a lift to drag ratio of 7.35.

Table 5.1: Forces on strut-hydrofoil junction straight T-junction

Force component	x-direction	z-direction
Mean total force [N]	$4.395828 \cdot 10^2$	$3.2297 \cdot 10^3$
Mean pressure force [N]	$1.560102 \cdot 10^2$	$3.2297 \cdot 10^3$
Mean viscous force [N]	$2.835727 \cdot 10^2$	$2.98 \cdot 10^{-2}$
Lift Coefficient C_L		0.2247
Drag Coefficient C_D	0.0306	

In Figure 5.2 are steady state simulations of the total forces relative to the last 2500 iterations plotted. This is included in this report as more of a curiosity. The forces clearly show unsteady behaviour which was the reason for changing to transient simulations. However, comparison of the mean values of the total lift and drag forces between the transient and steady state simulations for the finest mesh show only a 1.5% and 2.5% difference, respectively.

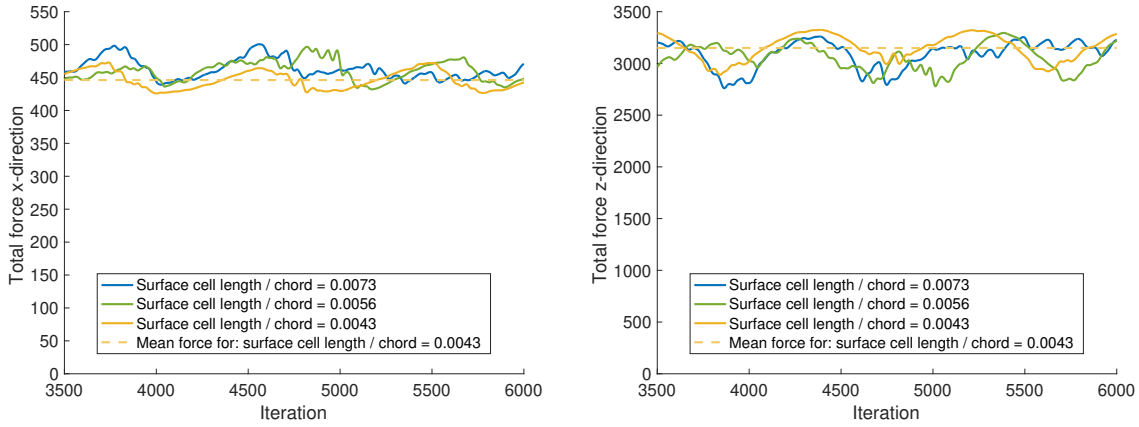

(a) Total drag force

(b) Total lift force

Figure 5.2: Total forces of last 2500 iterations of steady state simulations

In Figure 5.3a, a contour plot of the pressure coefficient at time $t = 1s$ (the end time) is shown. It can be seen that the pressure coefficient is decreasing towards the junction at the middle part of the hydrofoil section. Behind the middle part, close to the straight corner junction, are there local pressure peaks and troughs. These peaks are created by vortex development in the corner. The size and strength of this vortex is varying with time, which can be seen by comparing the pressure contour at $t = 1s$ and the pressure contours at $t = 0.95s$ and $t = 0.9s$, shown in Figure 5.3. It can be seen that at $t = 0.9s$ are the local pressure peaks and troughs less pronounced before they develop through $t = 0.95s$ to $t = 1s$. Similar oscillating behaviour in the intensity of the local pressure peaks and troughs was observed in earlier time steps as well.

The changes in pressure on the wing surface close to the corner are connected with the force oscillations seen in Figure 5.1. Examining the forces at similar times to the pressure contour plots, it can be seen that when the local pressure peaks and troughs are more pronounced, at $t = 1s$, the lift force reaches a minimum. Regarding the drag force, it is more challenging to discern a clear indication from the figures presented here. However, by comparing contour plots from additional time instances (included in Appendix A) with the drag force at similar times, it becomes evident that more distinct pressure peaks and troughs correspond to a larger drag force.

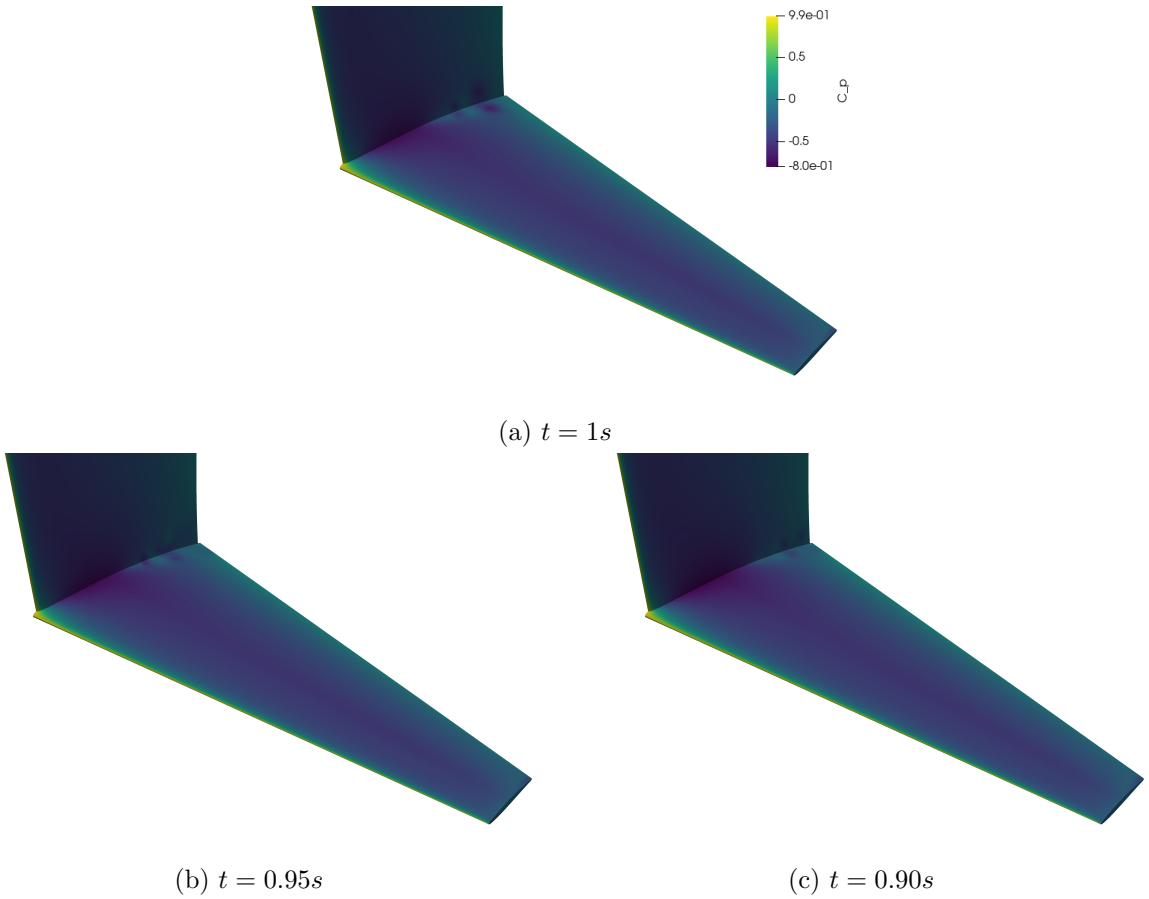

(a) $t = 1s$

(b) $t = 0.95s$

(c) $t = 0.90s$

Figure 5.3: Development of the pressure coefficient C_p for the straight T-junction design over time

In Figure 5.4, the pressure coefficient is plotted relative to the wing position divided by the local chord length. The two plots in Figure 5.4a represent the pressure coefficient at different positions along the hydrofoil span. The point at $y = -0.023m$ is located next to the corner, while the point at $y = -0.375m$ is in the middle of the hydrofoil. Differences in the shape of the pressure profile between these positions are expected due to the hydrofoil's increasing thickness towards the junction.

The focus lies on the variation in the pressure profile on the suction side of the foil between the point close to the corner and middle of the wing. It is evident that the pressure coefficient is lower closer to the corner, with the minimum pressure coefficient occurring around $x/C = -0.2$ with a value of $C_p = -0.7519$. In the validation results for the wing body junction, it was found that the CFD simulations predicted the lowest pressure point to be slightly further forward compared to the experimental results, shown in Subsection 4.2.2. Hence similar limitations regarding the accuracy of the position of the lowest pressure point could be observed here. However, the difference in position of the lowest pressure point between experiment and simulations for the wing body junction was relatively small. The absolute magnitude of the lowest pressure coefficient closest to the corner, for the wing body junction validation, had very good correlation between CFD and experiment. Giving some confidence in the accuracy of the minimum pressure in Figure 5.4a.

In Figure 5.4b, the visual representation illustrates the endpoint of pressure oscillations caused by the corner vortex. Specifically, the oscillations come to an end between the positions $y = 0.06m$ and $y = 0.07m$. It is important to note that the exact position of this endpoint varies over time, alongside changes in the size and strength of the corner vortex. Nevertheless, it provides valuable insight into the extent of the corner vortex's influence, indicating how far its effects reach from the corner. Notably, for this particular wing with a span of $0.75m$, the corner vortex induces pressure oscillations along the aft part of the foil for more than 9 percent of the wing span.

The change in pressure distribution with time at $y = 0.023m$ is shown in Figure 5.5. The plots shows large changes at the aft half of the foil section. However, the global minimum values keeps relatively stable over time.

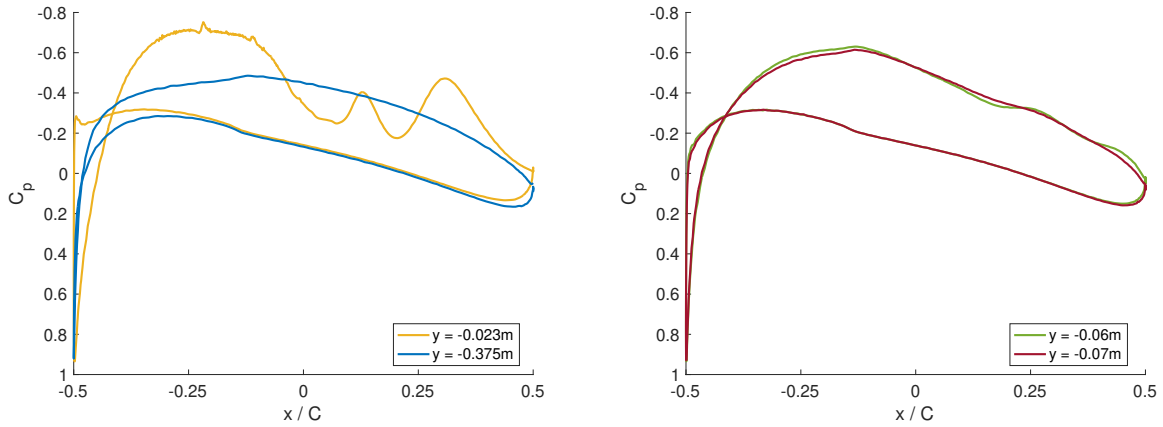

(a) C_p at $y = -0.023$ and $y = -0.375$

(b) C_p at $y = -0.06$ and $y = -0.07$

Figure 5.4: Pressure coefficient relative to the wing position divided by local chord length for $t = 1s$

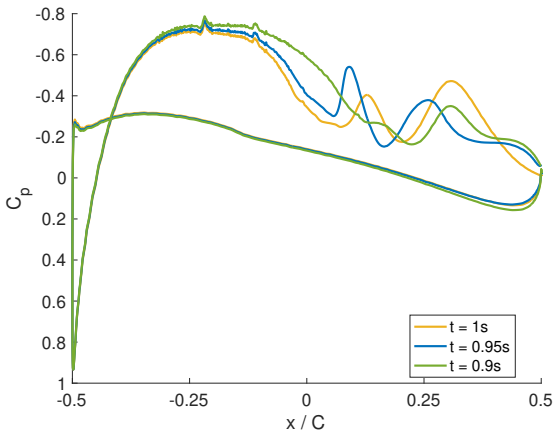

Figure 5.5: Development of pressure coefficient in corner over time at $y = -0.023m$

Contour plots of the of the primary flow U_x at various positions along the hydrofoil is presented in Figure 5.6. The x-coordinate is normalised by the root chord length $C_{root} = 0.36m$. The

point $x/C_{root} = 0$ is the middle of the hydrofoil while $x/C_{root} = 0.5$ is at the trailing edge.

The contour plots reveal a thickening of the boundary layer in the corner starting from $x/C_{root} = 0$. his observation aligns well with the theoretical principles outlined by Hoerner (1965), Subsection 2.1.2, where the pressure gradients of two foils combine to retard the boundary layer. The thickening of the boundary layer, as seen in Figure 5.6, leads to interference drag. However, when comparing velocity contour plots between experimental and CFD results for the wing body junction in Figure 4.12, it is evident that the CFD simulations exhibit a greater thickening effect. This discrepancy has been attributed to the turbulence model, as discussed in Subsection 4.2.2. The overestimation of boundary layer thickening in the CFD simulations consequently results in an overestimation of interference drag, leading to an overestimation of the total drag.

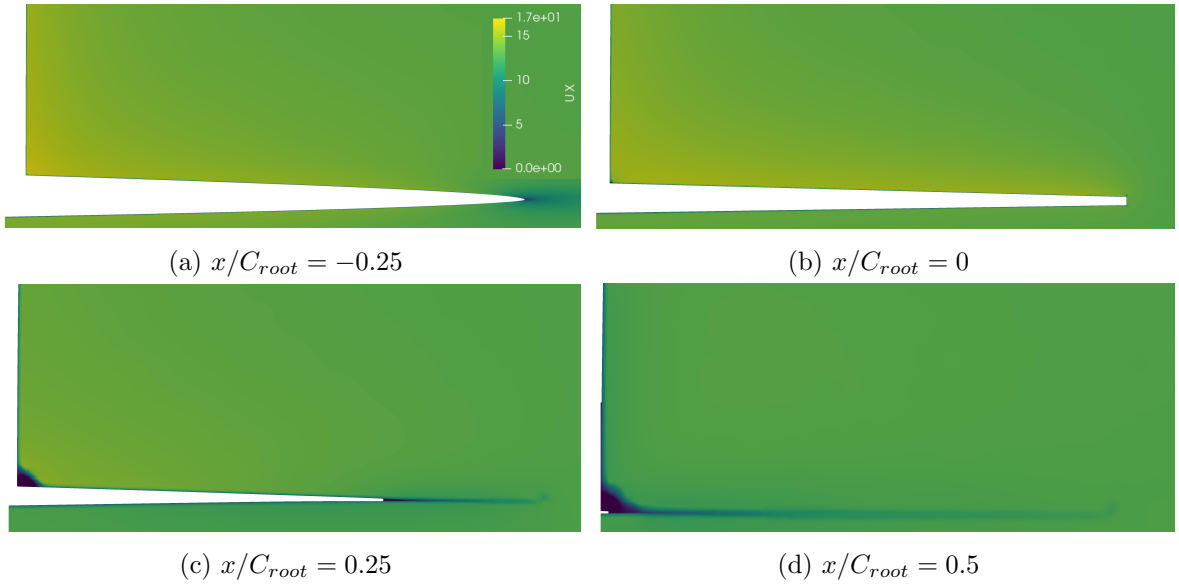

(a) $x/C_{root} = -0.25$ (b) $x/C_{root} = 0$

(c) $x/C_{root} = 0.25$ (d) $x/C_{root} = 0.5$

Figure 5.6: U_x at different x positions along the foil root chord at $t = 1s$

In Figure 5.7 are contour plots of the secondary flow U_y shown. It can clearly be seen how a corner vortex behind the middle point of the hydrofoil is developed. Based on the validation results for the secondary flow of the wing body junctions, shown in Figure 4.10 is it clear limitations to the simulations accuracy in representing the position and strength of the secondary flow in the corner.

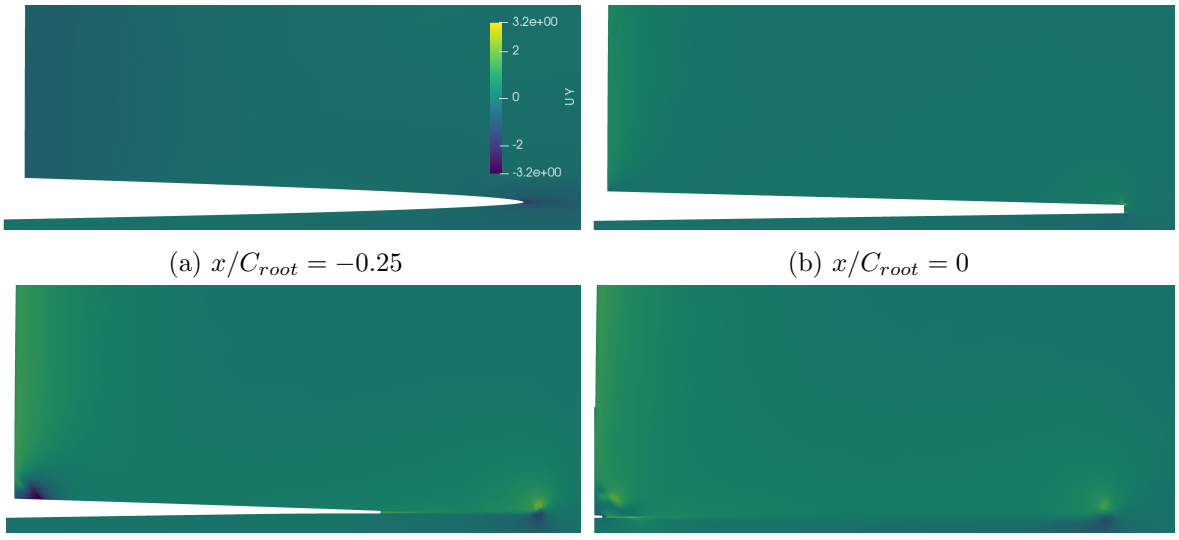

(a) $x/C_{root} = -0.25$ (b) $x/C_{root} = 0$

(c) $x/C_{root} = 0.25$ (d) $x/C_{root} = 0.5$

Figure 5.7: U_y at different x positions along the foil root chord at $t = 1s$

5.2 Strut-Hydrofoil Junction with Fillet

The strut-hydrofoil junction with a fillet was simulated using steady state. The computed forces acting on the hydrofoil are tabulated in Table 5.2. The lift and drag coefficients are calculated based on the projected area of the bottom hydrofoil. The total lift and drag forces are $3.415143 \cdot 10^3 N$ and $4.272723 \cdot 10^2 N$, respectively. This gives a lift to drag ratio of 8. The pressure drag is $1.453521 \cdot 10^2 N$ accounting for about 34% of the total drag force. The remaining percent of the total drag force is the viscous drag of $2.819202 \cdot 10^2 N$.

Table 5.2: Forces on strut-hydrofoil junction with fillet

Force component	x-direction	z-direction
Total force [N]	$4.272723 \cdot 10^2$	$3.415143 \cdot 10^3$
Pressure force [N]	$1.453521 \cdot 10^2$	$3.415672 \cdot 10^3$
Viscous force [N]	$2.819202 \cdot 10^2$	$-5.287745 \cdot 10^{-1}$
Lift Coefficient C_L		0.2376
Drag Coefficient C_D	0.0297	

The contour of the pressure coefficient on the hydrofoil surface is shown in Figure 5.8a. The pressure contours close similarity along the span, with high pressure at the leading edge and low pressure just ahead of the middle of the chord length.

In Figure 5.9 is the pressure coefficient over the local chord length plotted for $y = -0.038m$ and $y = -0.375m$. The point $y = -0.038m$ is the point with the lowest minimum pressure coefficient on the hydrofoil. This point is located on the fillet, as the fillet stretches to $-0.063m$. The point $y = -0.375m$ corresponds to the middle point of the hydrofoil wing span. From the plots can it be seen how the lowest pressure coefficient is a lot lower close to the corner. The minimum

pressure coefficient of the graph at $y = -0.038m$ is located between $-0.2 < x/C < -0.1$ with a value of $C_p = -0.7409$.

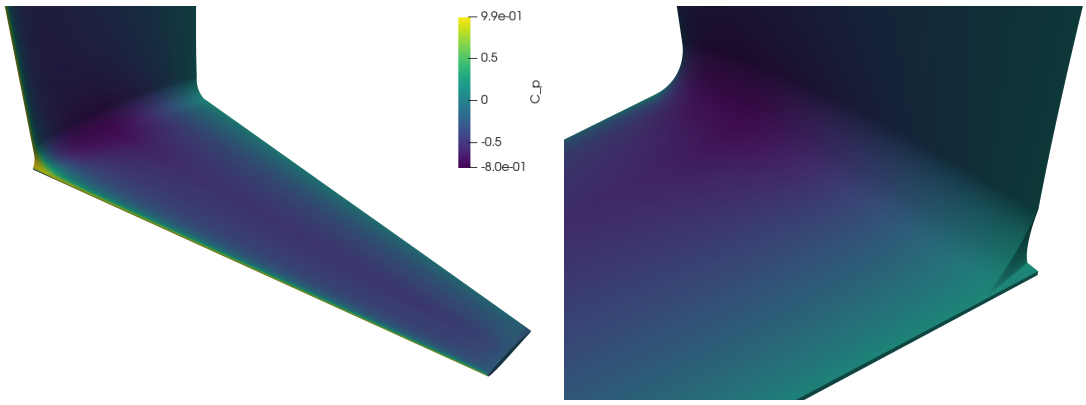

(a) C_p from the front (b) C_p from trailing edge

Figure 5.8: Pressure coefficient of the fillet design

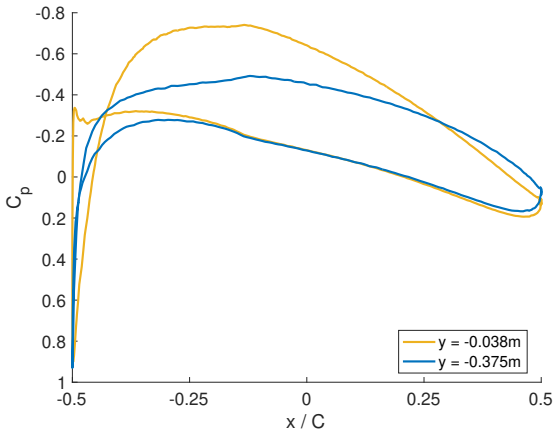

Figure 5.9: Pressure coefficient at $y = -0.038m$ and $y = -0.375m$

In Figure 5.10 are the velocity contours of the primary flow U_x presented. They show no visible thickening of the boundary layer in the corner for the points in front and middle of the chord length, Figure 5.10a and 5.10b, respectively. In Figure 5.10c is it a very slight thickening of the boundary layer in the corner. While it in Figure 5.10d, which is at the trailing edge, is a clear point with very low velocity in the corner. However, this point does not arise because of the interaction of the boundary layers of the strut and the hydrofoil, but rather because the fillet design does not have a tapering towards the end. Thus ending quite abrupt right before the trailing edge, which is what causes the corner with very low fluid velocity in x-direction. The design with pressure contours can be seen in Figure 5.8b. This also increases the pressure drag which was enlisted in Table 5.2. Similar contour plots of the secondary flow U_y for the fillet design is included in Appendix A.

The fillet counteracting the development of vortex development in the corner is in contrary to the results attained by W. J. Devenport et al. (1990), presented in Subsection 2.3.3. They

used a fillet to round the corner of the wing body junction, used for the validation study in Subsection 4.2.2, with a fillet radius of 0.53T. Their results show an increase in the size and strength of the vortex with the fillet design. However, the fillet design utilised in this study has a fillet radius equal to the thickness of the strut, which likely changes the influence from the fillet. These results indicates a strong sensitivity in the effect by fillet from the fillet radius.

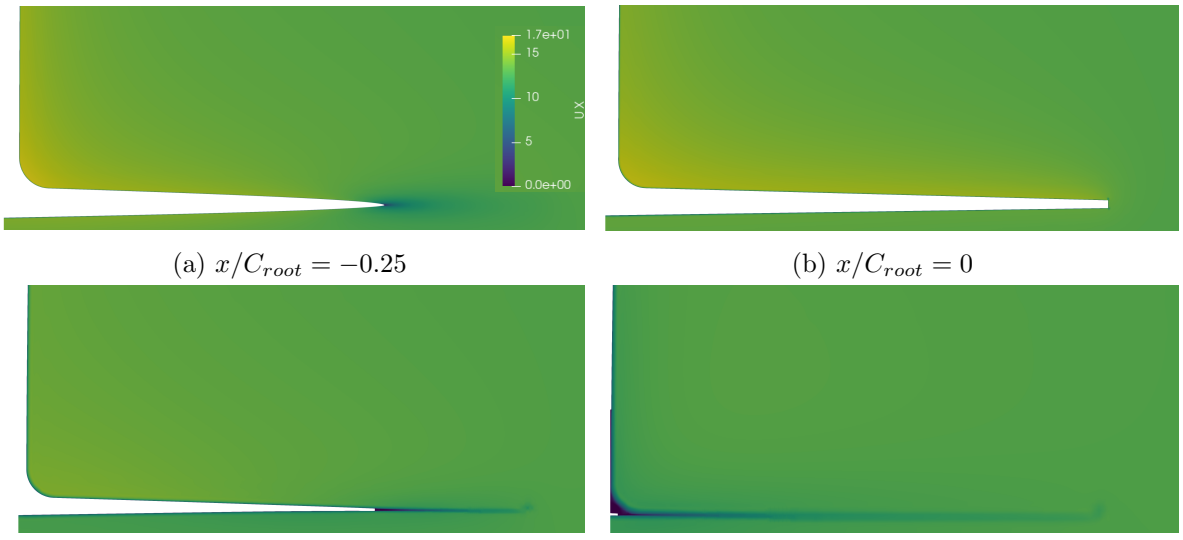

(a) $x/C_{root} = -0.25$ (b) $x/C_{root} = 0$

(c) $x/C_{root} = 0.25$ (d) $x/C_{root} = 0.5$

Figure 5.10: U_x at different x positions along the foil root chord for design with fillet

5.3 Strut-Hydrofoil Junction with Bulb

The forces acting on the strut-hydrofoil junction with bulb calculated with CFD simulations are tabulated in Table 5.3. The total lift force is $3.109112 \cdot 10^3 N$, while the total drag force is $4.227510 \cdot 10^2 N$, giving a lift to drag ratio of 7.35. The pressure drag is $1.328939 \cdot 10^2 N$ accounting for 31% of the total drag. While the remaining 69% is the viscous drag of $2.898571 \cdot 10^2 N$. The lift and drag coefficients are calculated based on the projected area of the bottom hydrofoil with straight corner. With this reference area is the lift and drag coefficients 0.2163 and 0.0294, respectively.

Table 5.3: Forces on strut-hydrofoil junction with bulb

Force component	x-direction	z-direction
Total force [N]	$4.227510 \cdot 10^2$	$3.109112 \cdot 10^3$
Pressure force [N]	$1.328939 \cdot 10^2$	$3.109701 \cdot 10^3$
Viscous force [N]	$2.898571 \cdot 10^2$	$-5.889776 \cdot 10^{-1}$
Lift Coefficient C_L		0.2163
Drag Coefficient C_D	0.0294	

In Figure 5.11 are the pressure coefficient contours on the hydrofoil surface shown. It is not any clear areas towards the corner with lower pressure. However the pressure distribution on the

bulb is clearly different to the rest of the hydrofoil section.

Figure 5.12a shows plots of the pressure coefficient relative to the local chord length at the points $y = -0.07m$ and $y = -0.375m$. The point $y = -0.07m$ is just when the bulb is ending and is the point with the lowest minimum pressure coefficient on the hydrofoil surface. The minimum pressure coefficient is $C_p = -0.6026$ and takes place around $x/C = -0.1m$. In Figure 5.12b is the pressure coefficient along the bulb right on top of it plotted. The minimum pressure at this position is $C_p = -0.5883$ which is nearly as low as at $y = -0.07m$.

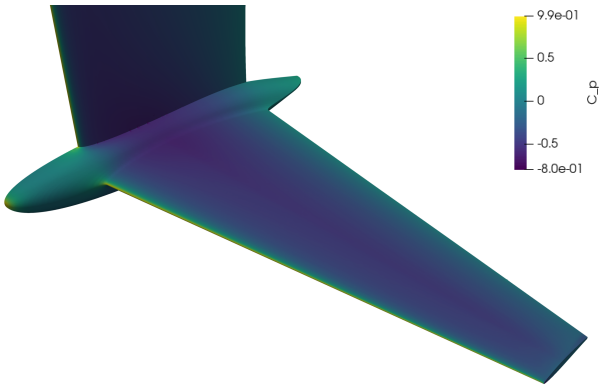

Figure 5.11: Pressure coefficient C_p for the bulb design

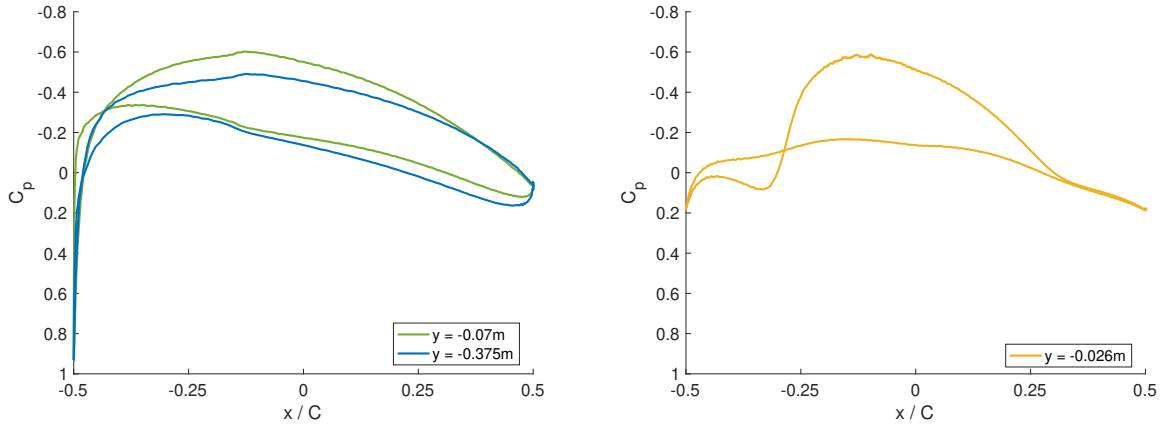

(a) C_p at $y = -0.07m$ and $y = -0.375$

(b) C_p on top of bulb

Figure 5.12: Pressure coefficient relative to the wing position divided by local chord length for bulb design

In Figure 5.13 are velocity contours for the bulb design presented. They show that it is a thickening of the boundary layer at the point of the bulb with the most curvature, for point along the chord length, though very small. This could be due to the curvature creating some separation. For the two points furthest back on the hydrofoil can it also be seen a slight thickening in the corner created between the top of the bulb and the vertical strut. However, these changes in the thickness of the boundary layers are relatively small. Similar contour plots of the secondary flow U_y for the bulb design is included in Appendix A for further assessment of the corner flows.

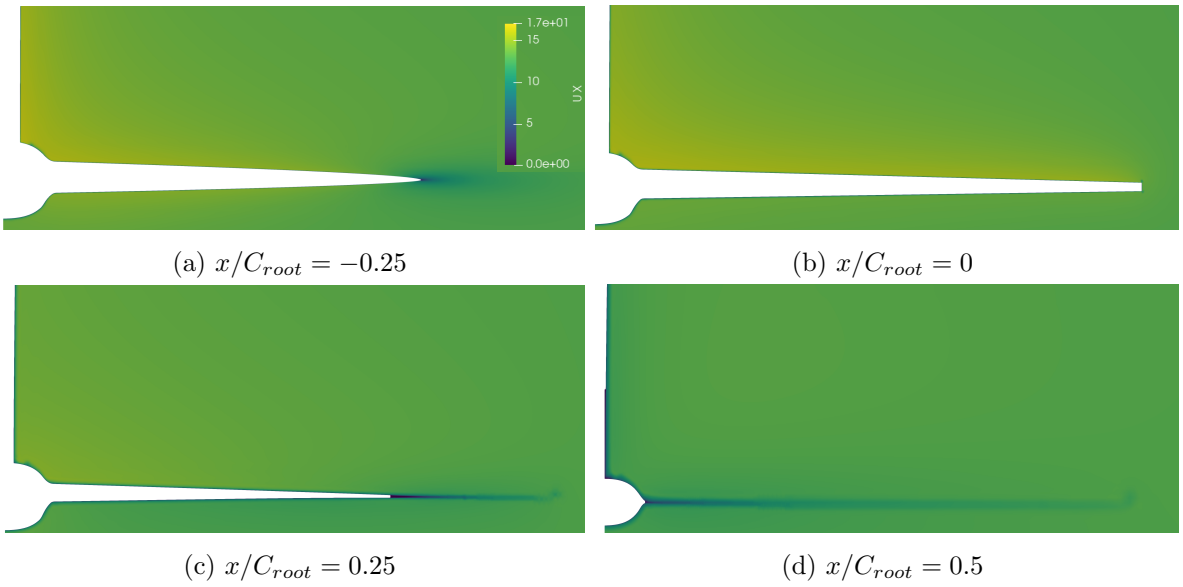

(a) $x/C_{root} = -0.25$ (b) $x/C_{root} = 0$

(c) $x/C_{root} = 0.25$ (d) $x/C_{root} = 0.5$

Figure 5.13: U_x at different x positions along the foil root chord for design with bulb

5.4 Comparison between the Designs

The three different strut-hydrofoil designs will be compared based on drag and likelyhood of cavitation inception.

Having a high lift-to-drag ratio is desirable for hydrofoil designs. Among the three designs, the fillet design achieved a lift-to-drag ratio of 8, while the other two designs had a ratio of 7.35. When studying the viscous resistance, it is observed that the bulb design has the highest viscous resistance, about 3 percent and 2 percent higher than the fillet and straight T-junction designs, respectively. However, the bulb design has the lowest pressure resistance, which is approximately 8.5 percent lower than the fillet design and 15 percent lower than the straight T-junction design.

The pressure drag provides an indication of the interference drag. Referring back to Figure 2.3 in Subsection 2.1.2. Using a fairing radius divided by chord length of 11 percent, which the fillet in this study has, it can be seen that the results of a 7 percent decrease in pressure resistance corresponds well with the plots in Figure 2.3. In the study by Hoerner (1965) is it also mentioned that the interference drag of a straight T-junction could be reduced by up to 10 percent by a fairing, which also corresponds well with the previously presented results. However, as mentioned in Section 5.1 there was indications from the validation study that the CFD simulations overestimated the corner separation in a straight corner, resulting in a larger interference drag. Considering that the fillet design used in this study creates a substantial corner with zero velocity when ending, shown in Figure 5.10d, it is suspected that these two effects may, to some point, counteract each other. Hence, making the difference in interference drag between straight corner and fillet, from the simulations, seem correct if compared to fillet designs causing less pressure drag behind them. This is a theory and not based on conclusive proof.

The bulb design exhibits a 15 percent lower pressure resistance than the straight T-junction. Hoerner (1965) suggests that the interference drag can be further reduced by more than 10 percent with a fillet that extends behind the trailing edge of the foil, which the bulb design in this study incorporates. Considering this, the 15 percent reduction in pressure drag for the bulb design appears reasonable.

The lower lift of the bulb design, approximately 4 percent lower than the straight T-junction and 9 percent lower than the fillet design, is caused by the bulb covering parts of the lifting hydrofoil. It is somewhat surprising that the lift of the straight T-junction is 5 percent lower than that of the fillet design. The reduction in lift for the straight T-junction is caused by an increase in pressure at the aft part of the foil close to the corner. This pressure increase takes place through pressure oscillations as shown in Figure 5.4 and 5.5. These oscillations are effecting the pressure until $y = 0.07m$, which is a similar place to where the bulb ends. Considering this, it seems more reasonable that the lift of the straight T-junction is lower than that of the fillet design. In Hoerner (1985) is it mentioned that for a straight wing strut junction "There is no doubt that strut interference reduces the effective aspect ratio by some 10%". Hence, it is expected to observe a significant reduction in lift from the corner effects. However, the discussion regarding whether the CFD simulations overestimate the separation effect of the meeting boundary layers in a straight corner remains important.

Comparison of the pressure coefficient of the different designs in the place with lowest pressure coefficient is shown in Figure 5.14. Just based on the lift-to-drag ratio, the fillet design performs better than the other two designs. However, the fillet design does not significantly increase the lowest pressure coefficient on the hydrofoil surface, maybe rather increases it from the plots. In contrast, the bulb design provides a 28 percent increase in the lowest pressure coefficient compared to the other two designs. This reduction in the possibility of cavitation inception makes the bulb design favourable in terms of mitigating cavitation effects. Therefore, if reducing the chances of cavitation inception is important in the design process, the CFD simulations performed in this study demonstrate these qualities for the bulb design.

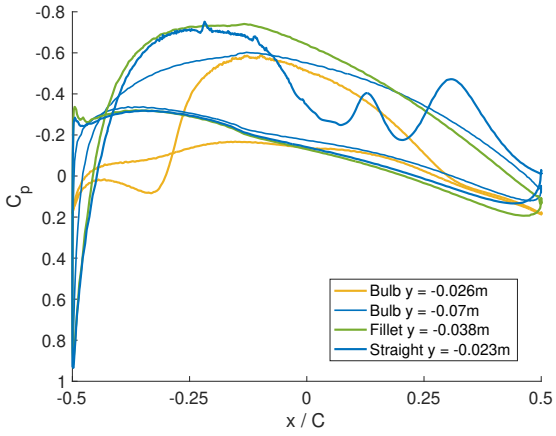

Figure 5.14: Comparison of pressure coefficient for different designs

Chapter 6

Conclusions and Further Work

The objective of the study was to evaluate designs of the junction between the strut and the hydrofoil by means of CFD simulations, keeping a balance between accuracy and computational complexity.

The complex 3-dimensional flow created by the meeting boundary layers in the junction necessitated the selection of appropriate turbulence models for the simulations. Based on the available literature on flows with meeting boundary layers in a corner, two turbulence models, EBRSM and $k - \omega$ SST, were chosen as viable options for simulating the flow over the strut-hydrofoil junction. However, the EBRSM model encountered significant stability issues during the simulations prohibiting results from being produced with this model. The stability issues likely stemming from the layers generated by the integrated mesher, `snappyHexMesh`, in OpenFOAM.

One significant challenge is the lack of publicly available experimental data similar to the strut-hydrofoil junctions, that could be used to validate the CFD simulations. Thus, the validation study of the simulations involved two cases from the aeronautical industry: a 2D NACA 0012 airfoil and a wing body junction. These cases were selected to assess the accuracy of the simulations in terms of profile drag, lift, and flow representation in a corner. The simulation results were compared with experimental data.

For the 2D NACA 0012 case, the simulations demonstrated reasonable accuracy, although there was a slight discrepancy in drag at high angles of attack when compared to experimental data. However, since the strut-hydrofoil junctions were tested at 0 angle of attack, these results were considered acceptable.

In the case of the wing body junction, larger discrepancies between the experimental results and the CFD simulations were observed. This was expected due to the limitations of the chosen simulations and turbulence model. Specifically, the simulation tended to overestimate the corner separation. However, the CFD simulations were able to capture the mean flow features quite well. Similar results were obtained from other CFD studies using the same case and turbulence model, which confirmed that the limitations stemmed from the chosen simulation type and turbulence model rather than mistakes in the computational setup. Overall, the validation study showed reasonably good accuracy for the lift and drag of a wing profile and mean flow

features in a corner junction. However, there were clear limitations in specific flow details such as the corner vortex and over prediction of the corner separation.

In this thesis, three different strut-hydrofoil junction designs were tested: straight T-junction, fillet, and bulb. The fillet design demonstrated the highest lift-to-drag ratio of 8, while the other designs had a ratio of 7.35. The bulb design exhibited the highest viscous drag among the three designs, but it also had the smallest pressure drag. On the other hand, the straight T-junction design had the highest pressure drag, resulting from the interference between the boundary layers of the strut and hydrofoil. Regarding lift, the fillet design achieved the highest value, indicating that the corner interference in the straight T-junction design was reducing its lift performance. In terms of overall lift and drag characteristics, the fillet design displayed the best performance. However, when considering the lowest pressure on the wing surface, which is crucial for avoiding cavitation inception, the bulb design outperformed the other two designs. The fillet design had a very similar lowest pressure coefficient to the straight T-junction, while the bulb design exhibited a significant increase of 28 percent in the lowest pressure coefficient. This suggests that the bulb design has an advantage in reducing the possibility of cavitation inception compared to the other designs.

In conclusion from the results, based on the lift and drag characteristics, the fillet design demonstrated the best performance. However, when focusing on the lowest pressure coefficient on the wing surface and the prevention of cavitation, the bulb design showed superior performance.

Indeed, there were limitations observed in the CFD simulations of the strut-hydrofoil junctions. Some of the discrepancies identified between the experimental data and CFD results in the validation study are likely to be applicable to the strut-hydrofoil designs as well. The overestimation of corner separation is expected to have a more significant impact on the results of the straight T-junction design compared to the fillet and bulb designs. This is because the meeting boundary layer interference is more pronounced in the straight T-junction, where the corner separation plays a crucial role. Consequently, this limitation is likely to influence the results of the straight T-junction design more prominently than the fillet and bulb designs.

In conclusion, despite the mentioned limitations, notable distinctions were observed among the various strut-hydrofoil designs. Consequently, these CFD simulations are regarded as a potential tool for analysing such configurations with a reasonable level of accuracy, while avoiding excessively complex computations. This is particularly applicable to designs where the merging boundary layers do not exert significant effects.

Based on the experience gained from the CFD simulations in this study, here are some suggested areas for further research and improvement:

- As mentioned, one significant limitation is the lack of publicly available experimental data similar to the strut-hydrofoil junctions studied, which could be used to validate the CFD simulations. While experiments of this nature have been conducted by organisations like America's Cup teams, they are typically not accessible to the public. Acquiring accurate experimental results for various generic strut-hydrofoil designs would greatly enhance the confidence in CFD simulations of such configurations.

- Investigating alternative meshing tools: The stability issues encountered with the EBRSM turbulence model were attributed to the layers generated by the `snappyHexMesh` meshing tool in OpenFOAM. It would be beneficial to assess the performance of the EBRSM model using different meshing tools, such as commercial CFD software like Star CCM+, to see if it resolves the stability problems.

- Testing the results of using other solution methods for the Navier-Stokes equations like Large Eddy Simulations (LES) or Improved Delayed Detached Eddy Simulation (IDDES) to assess their impact on the accuracy of flow prediction in the corner. However, it should be noted that these methods will require more computational resources than those employed in the current study.

- Comparing interference drag results: Conducting additional CFD simulations with strut and hydrofoil designs that do not change in shape along the span could allow for a comparison of interference drag results with empirical formulas presented in the literature. This would provide further insights into the accuracy and applicability of these formulas in predicting interference drag for different designs.

Bibliography

Airfoiltools (2023) *NACA 4 digit airfoil generator (NACA 0020 AIRFOIL)*. Available at: http://airfoiltools.com/airfoil/naca4digit?MNaca4DigitForm%5C%5Bcamber%5C%5D=0&MNaca4DigitForm%5C%5Bposition%5C%5D=0&MNaca4DigitForm%5C%5Bthick%5C%5D=20&MNaca4DigitForm%5C%5BnumPoints%5C%5D=150&MNaca4DigitForm%5C%5BcosSpace%5C%5D=0&MNaca4DigitForm%5C%5BcosSpace%5C%5D=1&MNaca4DigitForm%5C%5BcloseTe%5C%5D=0&MNaca4DigitForm%5C%5BcloseTe%5C%5D=1&yt0=Plot (Accessed: 10th May 2023).

Alizard, F., Rist, U. and Robinet, J.-C. (2009) Linear Instability of Streamwise Corner Flow, *Advances in Tubulence XII*, 132, pp. 67–70.

Apsley, D. D. and Leschziner, M. A. (1998) A new low-Reynolds-number non-linear two-equation turbulence model for complex flows, *J. Heat Fluid Flow*, 19, pp. 209–222.

— (2001) Investigation of Advanced Turbulence Models for the Flow in a Generic Wing-Body Junction, *Flow, Turbulence and Combustion*, 67, pp. 25–55.

Ashton, Dr Neil and Stoellinger, Prof. Micheal (2023) *Computation of Turbulent Flow in a Rotating Pipe using and Elliptic Blending Reynolds Stress Model*. Available at: https://www.nas.nasa.gov/assets/pdf/ams/2016/AMS_20160705_Ashton.pdf (Accessed: 19th Apr. 2023).

Bradshaw, Peter (1987) Turbulent Secondary Flows, *Ann. Rev. Fluid Mech.*, 19, pp. 53–74.

Carrier, G. F. (1947) The boundary layer in a corner, *Quarterly of Applied Mathematics*, 4, pp. 367–370.

Charles L. Ladson (1988) *Effects of independent variation of Mach and Reynolds numbers on the low-speed aerodynamic characteristics of the NACA0012 airfoil section*. Technical Memorandum. NASA Langley Reaserch Center Hampton.

Dawson, J. R. (2021) *Viscous Flows and Boundary Layers*.

Devenport, W. J., Agarwal, N. K., Dewitz, M. B., Simpson, R. L. and Poddar, K. (1990) Effects of a Fillet on the Flow Past a Wing-Body junction, *AIAA journal*, 28, pp. 2017–2024.

Devenport, William J., Simpson, R. L., Dewitz, Michael B. and Agarwal, Naval K. (1992) Effects of a Leading-Edge Fillet on the Flow Past and Appendage-Body Junction, *AIAA journal*, 30, pp. 2177–2183.

Doormaal, J. P. Van and Raithby, G. D. (1984) ENHANCEMENTS OF THE SIMPLE METHOD FOR PREDICTING INCOMPRESSIBLE FLUID FLOWS, *Numerical Heat Transfer*, 7(2), pp. 147–163. DOI: 10.1080/01495728408961817. eprint: https://doi.org/10.1080/01495728408961817. Available at: https://doi.org/10.1080/01495728408961817.

Eça, Luís, Vaz, Guilherme and Hoekstra, Martin (Jan. 2010) Code Verification, Solution Verification and Validation in RANS Solvers, vol. 6.

Faltinsen, Odd M. (2005) *Computational Fluid Mechanics and Heat Transfer*. Cambridge University Press.

Fleming, J. L., Simpson, R. L., Cowling, J. E. and Devenport, W. J. (1993) An experimental study of a turbulent wing-body junction and wake flow, *Experiments in Fluids*, 14, pp. 366–378.

Gand, Fabien, Deck, Sebastien, Brunet, Vincent and Sagaut, Pierre (2010) Flow dynamics past a simplified wing body junction, *Physics of fluids*, 22.

Gatski, T. B. and Speziale, C. G. (1993) On explicit algebraic stress models for complex turbulent flows, *J. Fluid Mech.*, 254, pp. 59–78.

Ghia, K. N. (1975) Incompressible Streamwis Flow Along an Unbounded Corner, *AIAA Journal*, 13, pp. 902–907.

Gibson, M. M. and Launder, B. E. (1978) Ground effects on pressure fluctuations in the atmospheric boundary layer, *J. Fluid Mech.*, 86, pp. 491–511.

Hoerner, Sighard F. (1965) *Fluid - Dynamic Drag*. Author.

— (1985) *Fluid - Dynamic Lift*. Author.

International Towing Tank Conference (2017) *Uncertainty Analysis in CFD Verification and Validation, Methodology and Procedures*. Technical Report. International Towing Tank Conference.

Issa, R.I, Gosman, A.D and Watkins, A.P (1986) The computation of compressible and incompressible recirculating flows by a non-iterative implicit scheme, *Journal of Computational Physics*, 62(1), pp. 66–82. ISSN: 0021-9991. DOI: https://doi.org/10.1016/0021-9991(86)90100-2. Available at: https://www.sciencedirect.com/science/article/pii/0021999186901002.

Jakirlic, S. and Hanjalic, K. (1995) A second moment closure for non-equilibrium and separating high and low-Re number flows, *Proceedings of 10th Symposium on Turbulent Shear Flows*, pp. 23.25–23.30.

Jamspali (2022) *SST k-omega model*. Available at: https://www.cfd-online.com/Wiki/SST_k-omega_model (Accessed: 17th Apr. 2022).

John D. Anderson, Jr. (2017) *Fundamentals of Aerodynamics*. McGraw-Hill Education.

Jones, D. A. and Clarke, D. B. (2005) Simulation of a Wing-Body Junction Experiment using the Fluent Code,

Kalitzin, G., Gould, A. R. B. and Benton, J. J. (1996) Application of two-equation turbulence models in aircraft design, *AIAA Paper*, 96.

Kornilov, V. I. (2017) Three-dimensional turbulent near-wall flows in streamwise corners: Current state and questions, *Progress in Aerospace Sciences*, 94, pp. 46–81.

Kramer, Jarle V., Godø, John Martin K. and Steen, Sverre (2018) Hydrofoil simulations - nonlinear lifting line vs CFD,

Kramer, Jarle V. and Steen, Sverre (2021) Simplified test program for hydrodynamic CFD simulations of wind-powered carge ships,

Lardeau, S. and Manceau, Remi (2014) Computations of complex flow configurations using a modified elliptic- blending Reynolds-Stress model, *10th International ERCOFTAC Symposium on Engineering Turbulence Modelling and Measurements*. Marbella, Spain. DOI: hal-01051799.

Launder, B. E. and Sharma, B. I. (1974) Applications of the energy-dissipation model of turbulence to the calculations of flow near a spinning disc, *Heat Mass Transfer*, 1, pp. 131–138.

Launder, B. E. and Spalding, D. B. (1974) The numerical computations of tubulent flows, *Comput. Methods Appl. Mech. Engrg.*, 3, pp. 269–289.

Lien, F. S., Chen, W. L. and Leschziner, M. A. (1998) Low-Reynolds-number eddy-viscosity modelling based on non-linear stress-strain/vorticity relations, *Engineering Turbulence Modelling and Measurements*, 3, pp. 91–100.

LiftOcean (2022) *Lift Ocean*. Available at: https://www.liftocean.no/p/56840/hydrofoil-system (Accessed: 11th May 2022).

Manceau, Remi (2015) Recent progress in the development of the Elliptic Blending Reynolds-stress model, *Journal of Heat and Fluid Flow*, p. 32.

Manceau, Remi and Hanjalić, Kemal (2002) Elliptic blending model: A new near-wall Reynolds-stress turbulence closure, *Physics of Fluids*, 14(2), pp. 744–754.

Menter, F. R. (1994) Two-Equation Eddy-Viscosity Turbulence Models for Engineering Applications, *AIAA*, 32, pp. 1598–1605.

Menter, Kuntz, M. and Langtry, RB (2003) Ten years of industrial experience with the SST turbulence model, *Heat and Mass Transfer*, 4, pp. 625–632.

Mestemaker, Benny, Castro, Bernardete, Blom, Erik van der and Cornege, Henk (2019) Zero emission vessels from a shipbuilders perspective,

NASA (2022) *2D NACA 0012 Airfoil Validation Case*. Available at: https://turbmodels.larc.nasa.gov/naca0012_val.html (Accessed: 17th May 2022).

— (2023) *SSTm Model Results*. Available at: https://turbmodels.larc.nasa.gov/naca0012_val_sst.html (Accessed: 12th Apr. 2023).

OpenFOAM (2023a) *CourantNo*. Available at: https://www.openfoam.com/documentation/guides/latest/doc/guide-fos-field-CourantNo.html (Accessed: 27th May 2023).

— (2023b) *Mesh generation with the snappyHexMesh utility*. Available at: https://www.openfoam.com/documentation/user-guide/4-mesh-generation-and-conversion/4.4-mesh-generation-with-the-snappyhexmesh-utility (Accessed: 20th Apr. 2023).

— (2022) *simpleFoam*. Available at: https://www.openfoam.com/documentation/guides/latest/doc/guide-applications-solvers-incompressible-simpleFoam.html (Accessed: 21st Apr. 2022).

— (2023c) *Solution and algorithm control*. Available at: https://www.openfoam.com/documentation/user-guide/6-solving/6.3-solution-and-algorithm-control (Accessed: 19th May 2023).

Park, Dong-Hun, Park, Seung-O, Kwon, Ki-Jung and Shim, Ho-Joon (2010) PIV Measurment of Laminar Boundary Layer in a Streamwise Corner, *Conference paper Fluid dynamics conference*, 40, pp. 1–13.

Parker, S. J. and Balachandar, S. (1999) Viscous and Inviscid Instabilities of Flow Along a Streamwise Corner, *Theoret. Comput. Fluid Dynamics*, 13, pp. 231–270.

Patankar, S.V and Spalding, D.B (1972) A calculation procedure for heat, mass and momentum transfer in three-dimensional parabolic flows, *International Journal of Heat and Mass Transfer*, 15(10), pp. 1787–1806. ISSN: 0017-9310. DOI: https://doi.org/10.1016/0017-9310(72)90054-3. Available at: https://www.sciencedirect.com/science/article/pii/0017931072900543.

Pope, Stephen B. (2000) *Turbulent Flows*. University Printing House.

Rubin, Stanley G. (1966) Incompressible flow along a corner, *J. Fluid Mech.*, 26, pp. 97–110.

Sheahan, Matthew (2022) *Foiling: the history of the hydrofoiler*. Available at: https://www.yachtingworld.com/features/foiling-the-history-of-the-hydrofoiler-135741 (Accessed: 11th May 2022).

Speziale, C. G., Sarkar, S. and Gatski, T. B. (1991) Modelling the pressure-strain correlation of turbulence: An invariant dynamic systems approach, *J. Fluid Mech.*, 227, pp. 245–272.

Stollinger, Michael K., Roy, Rajib and Ashton, Neil (2015) Application of an Elliptic Blending Reynolds Stress Model in Attached and Separated flows,

T.S.Klein, T.J.Craft and H.Iacovides (2015) Assessment of the performance of different classes of turbulence models in a wide range of non-equilibrium flows, *International Journal of Heat and Fluid Flow*, 51, pp. 229–256.

Tannehill, Anderson and Pletcher (1997) *Computational Fluid Mechanics and Heat Transfer*. Taylor & Francis.

Theberge, M.-A. and Ekmekci, A. (2017) Effects of an upstream triangular plate on the wing-body junction, *Phys. Fluids*, 29.

Wilcox, D. C. (1988a) Multiscale model for turbulent flows, *AIAA J.*, 26, pp. 1311–1320.

— (1988b) Reassessment of the scale-determining equation for advanced tubulence models, *AIAA J.*, 26, pp. 1299–1310.

Wimshurst, Dr. Aidan (2023) *What are Wall Functions and How do they work?* Available at: https://www.fluidmechanics101.com/index.html (Accessed: 27th Mar. 2023).

Zamir, M. (1981) Similarity and stability of the laminar boundary layer in a streamwise corner, *The Royal Society*, 377, pp. 242–246.

Zamir, M. and Young, A. D. (1970) Experimental Investigation of the Boundary Layer in a Streamwise Corner, *Aeronautical Quarterly*, 21, pp. 313–339.

Appendix A

Complementary Results

A.1 Wing body junction

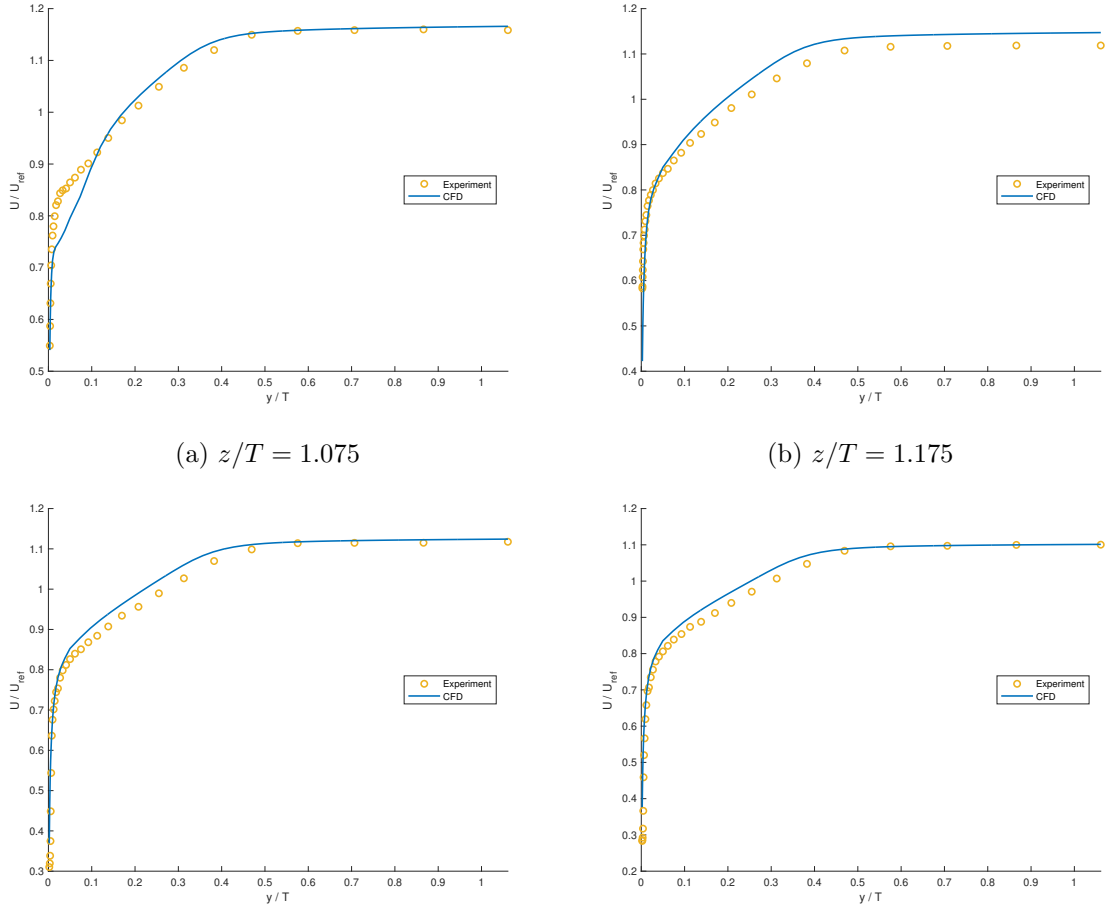

(a) $z/T = 1.075$

(b) $z/T = 1.175$

(c) $z/T = 1.325$

(d) $z/T = 1.525$

Figure A.1: Comparison between CFD and experiments of the secondary flow U/U_{ref} at $x/T = 0.75$

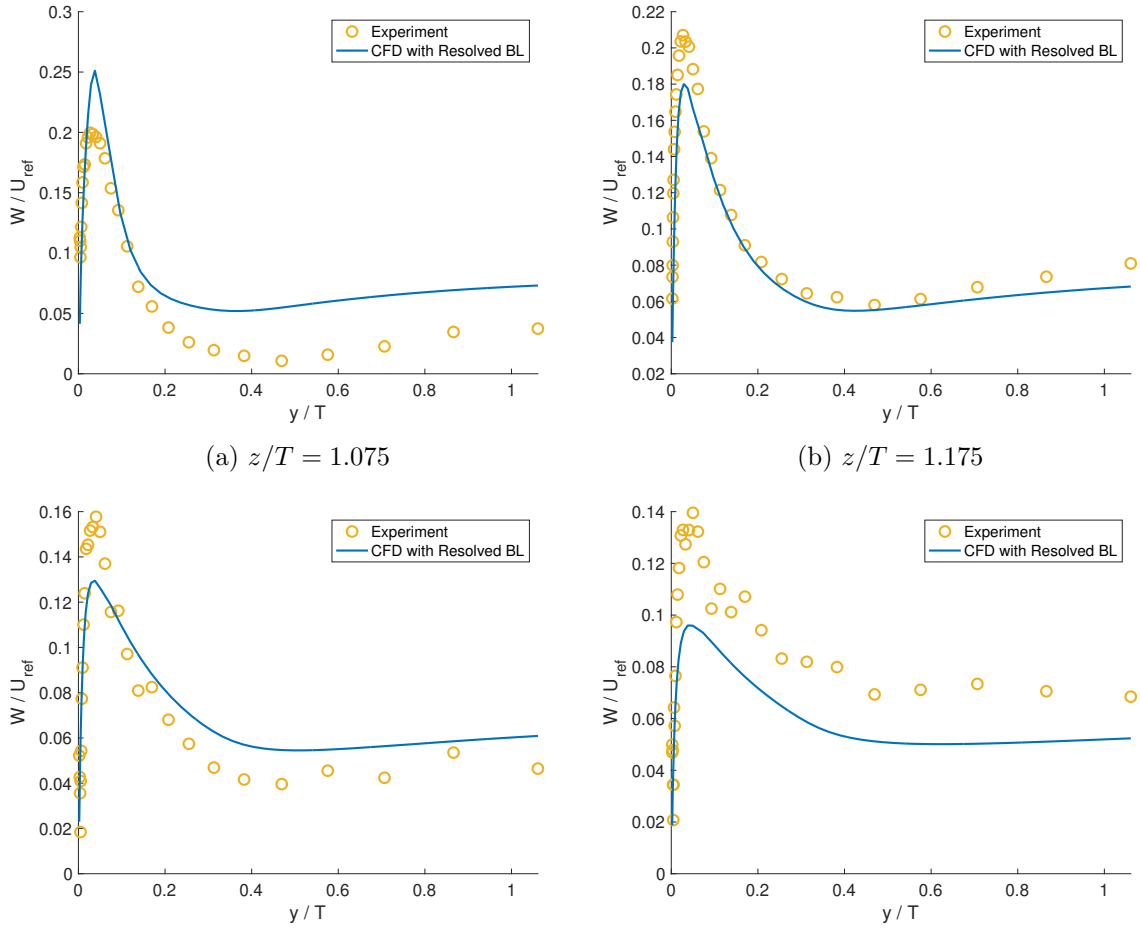

(a) $z/T = 1.075$

(b) $z/T = 1.175$

(c) $z/T = 1.325$

(d) $z/T = 1.525$

Figure A.2: Comparison between CFD and experiments of the secondary flow W/U_{ref} at $x/T = 0.75$

A.2 Strut-Hydrofoil Junctions

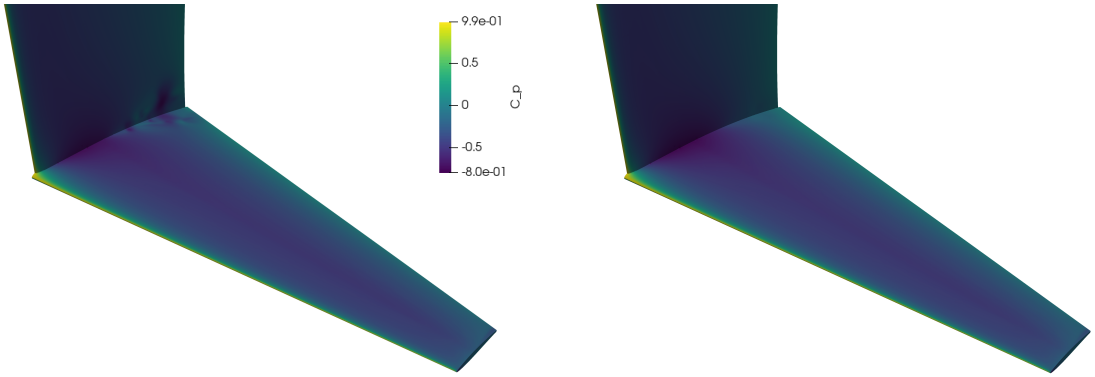

(a) $t = 0.4s$ (b) $t = 0.45s$

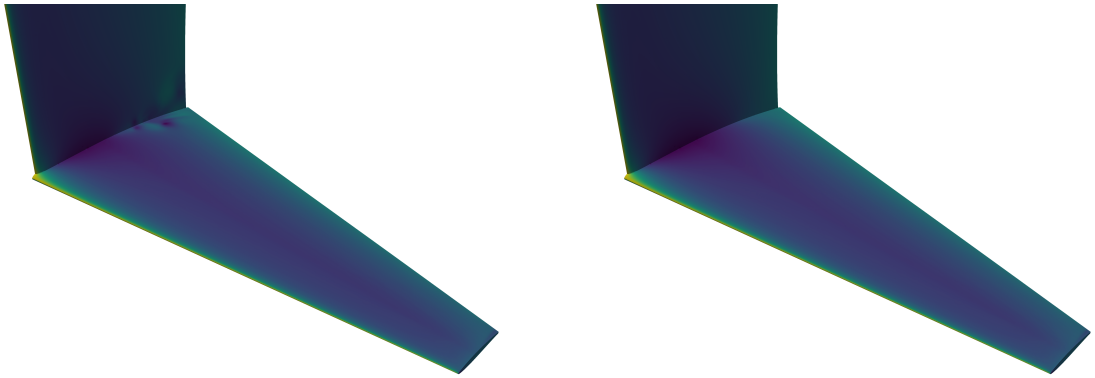

(c) $t = 0.525s$ (d) $t = 0.575s$

Figure A.3: Pressure contour plots for more times for straight T-junction design

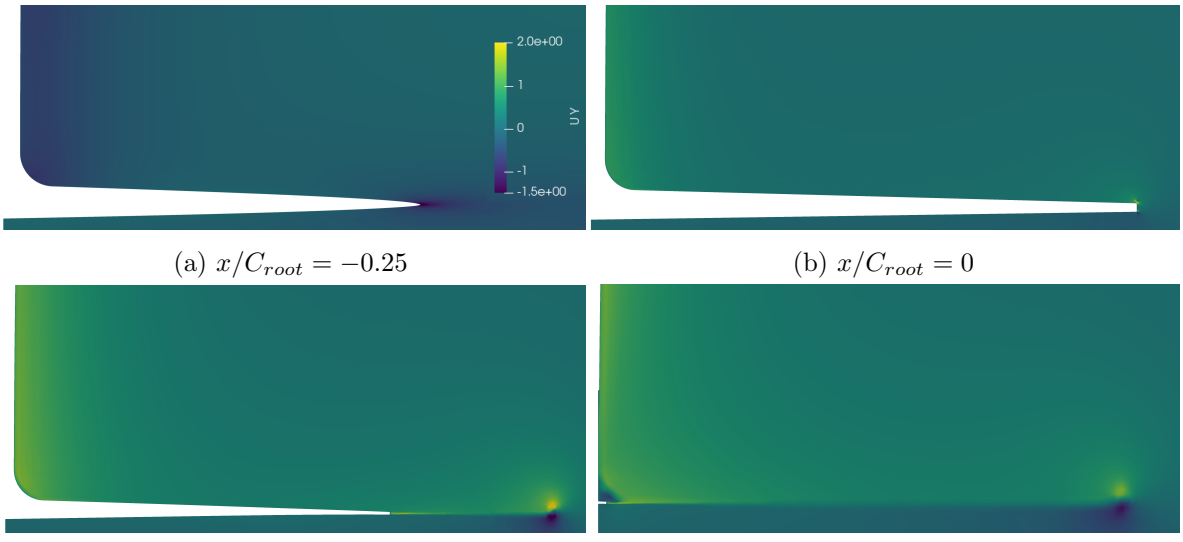

(a) $x/C_{root} = -0.25$ (b) $x/C_{root} = 0$

(c) $x/C_{root} = 0.25$ (d) $x/C_{root} = 0.5$

Figure A.4: U_y at different x positions along the foil root chord for design with fillet

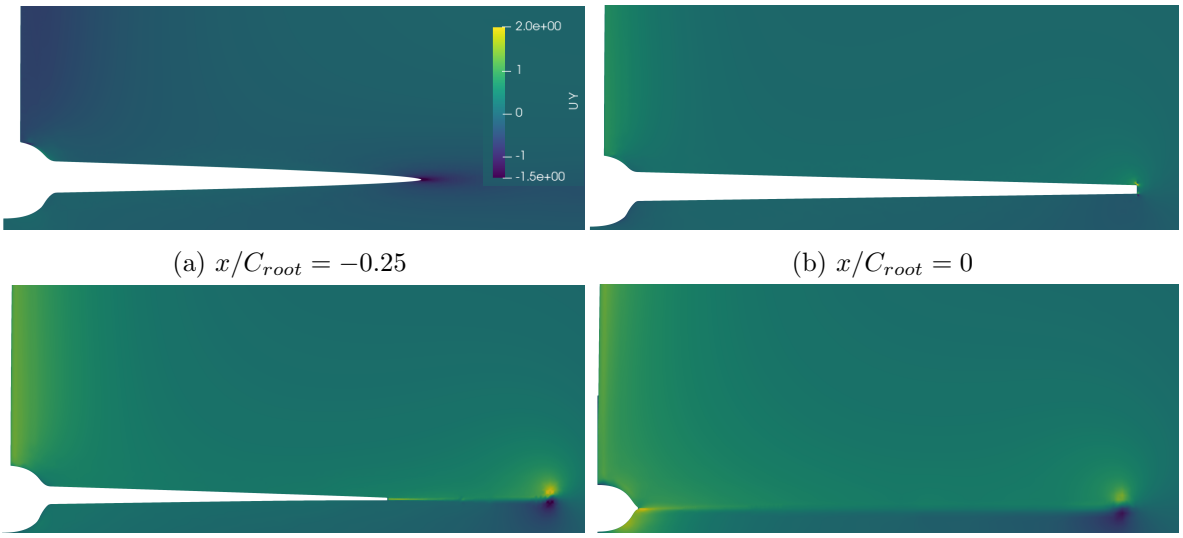

(a) $x/C_{root} = -0.25$

(b) $x/C_{root} = 0$

(c) $x/C_{root} = 0.25$

(d) $x/C_{root} = 0.5$

Figure A.5: U_y at different x positions along the foil root chord for design with bulb

Appendix B

Post-processing Code

B.1 Example post-processing Matlab

```
close all
clear;
clc
T = 0.0717;

% CFD results
fid = fopen('r.csv');
results = [];
while ¬feof(fid)
    fgetl(fid);
    data = textscan(fid, '%f, %f, %f, %f, %f, %f, %f, %f, %f, %f, %f', ...
        'HeaderLines', 0);
    results = [data{:}]; %x y z U:0 U:1 U:2 k nut omega p Cp
end
fclose(fid);

%Experimental results
fid = fopen('wbj-cp-body-27_2.dat');
cMat = [];
while ¬feof(fid)
    fgetl(fid);
    data = textscan(fid, '%f %f %f %f', 'HeaderLines', 0);
    cMat = [data{:}];
end
fclose(fid);


X = cMat(:,1);
Y = cMat(:,2);
Z = cMat(:,3);
Cp = cMat(:,4);

%Creating grid results
```

```
xv = linspace(min(X), max(X), numel(X));
yv = linspace(min(Y), max(Y), numel(Y));
zv = linspace(min(Z), max(Z), numel(Z));

[Xm,Zm] = ndgrid(xv, zv);
Cp_ex = griddata(X,Z,Cp, Xm, Zm);
Cp_CFD = griddata(results(:,1)/T,results(:,2)/T,results(:,3)/T...
    ,results(:,11),Xm,zeros(length(Xm),length(Xm)),Zm,'linear');

%Removing grid cells inside wing
k = boundary(X, Z, 1);
pgon = polyshape(X(k), Z(k),'Simplify',false);
idx = isinterior(pgon,Xm(:),Zm(:));
idx = reshape(idx,size(Xm));
Cp_ex(¬idx) = nan;
Cp_CFD(¬idx) = nan;


figure(1)
contourf(Xm, -Zm, Cp_ex,[-0.8 -0.7 -0.6 -0.5 -0.4 -0.3 -0.2 -0.1 0 ...
    0.1 0.2])
grid on
xlabel('x / T')
ylabel('z / T')
axis('equal')
colorbar

figure(2)
contourf(Xm, -Zm, Cp_CFD,[-0.8 -0.7 -0.6 -0.5 -0.4 -0.3 -0.2 -0.1 0 ...
    0.1 0.2])
grid on
xlabel('x / T')
ylabel('z / T')
axis('equal')
colorbar
```

B.2 ITTC Convergence Study

```
% ITTC - Convergence study

function [CFD_S0, d_i, U_i, r] = ittcMeshConv(x,y,h,i)
r = linspace(x(1),x(length(x)),100);

%Initial guess alpha
a_0 = (y(length(y)-1) - y(length(y)))/(x(length(x)-1)-x(length(x)));

% First fitting to find better initial conditions
f = fittype(@(a,b,x) b+a*x.^2);
options = fitoptions('Method', 'NonlinearLeastSquares','StartPoint',...
    [a_0 y(length(y))]);
fitObject = fit(x',y',f,options);
```

```
Coeffs = coeffvalues(fitObject);
a = Coeffs(1);
b = Coeffs(2);

%First curve fit with initialconditions
f = fittype(@(a,b,n,x)  b+a*x.^n);
options = fitoptions('Method', 'NonlinearLeastSquares','StartPoint',...
   [a b 1.99]);
fitObject = fit(x',y',f,options);
Coeffs = coeffvalues(fitObject);

S_i = Coeffs(2) + Coeffs(1)*r.^Coeffs(3);
Coeff_final = Coeffs;
CFD_S0 = abs(y - Coeff_final(2))/Coeff_final(2);
d_i = abs((S_i - Coeff_final(2))/Coeff_final(2));
U_i = 1.25 * d_i;
initial_a = Coeffs(1);
initial_S = Coeffs(2);
initial_p = Coeffs(3);

if Coeffs(3) > 2 %r > 2
    f = fittype(@(a,b,x) b + a*x.^2);
    options = fitoptions('Method', 'NonlinearLeastSquares',...
         'StartPoint', [initial_a initial_S]);
    fitObject = fit(x',y',f,options);
    Coeff_final = coeffvalues(fitObject);
    S_i = Coeff_final(2) + Coeff_final(1)*r.^2;
    CFD_S0 = abs(y - Coeff_final(2))/Coeff_final(2);
    d_i = abs((S_i - Coeff_final(2))/Coeff_final(2));
    U_i = 1.25 * d_i;
    if initial_p > 2.1
        U_i = 3 * d_i;
    end
end

if Coeffs(3) < 0.5 %r < 0.5
    f = fittype(@(a,b,c,x) b + c*x + a*x.^2);
    options = fitoptions('Method', 'NonlinearLeastSquares',...
         'StartPoint', [0 0 initial_S]);
    [fitObject1, gof1] = fit(x',y',f,options);

    f = fittype(@(a,b,x) b + a*x.^2);
    options = fitoptions('Method', 'NonlinearLeastSquares',...
         'StartPoint', [initial_a initial_S]);
    [fitObject2, gof2] = fit(x',y',f,options);
    if gof2 > gof1 %Best fit of the two fittings
        Coeff_final = coeffvalues(fitObject1);
        S_i = Coeff_final(2) + Coeff_final(1)*r.^2;
    else
        Coeff_final = coeffvalues(fitObject2);
        S_i = Coeff_final(2) + Coeff_final(3)*r + Coeff_final(1)*r.^2;
    end
    CFD_S0 = abs(y - Coeff_final(2))/Coeff_final(2);
    d_i = abs((S_i - Coeff_final(2))/Coeff_final(2));
    U_i = 3 * d_i;
```

```
69 end
```

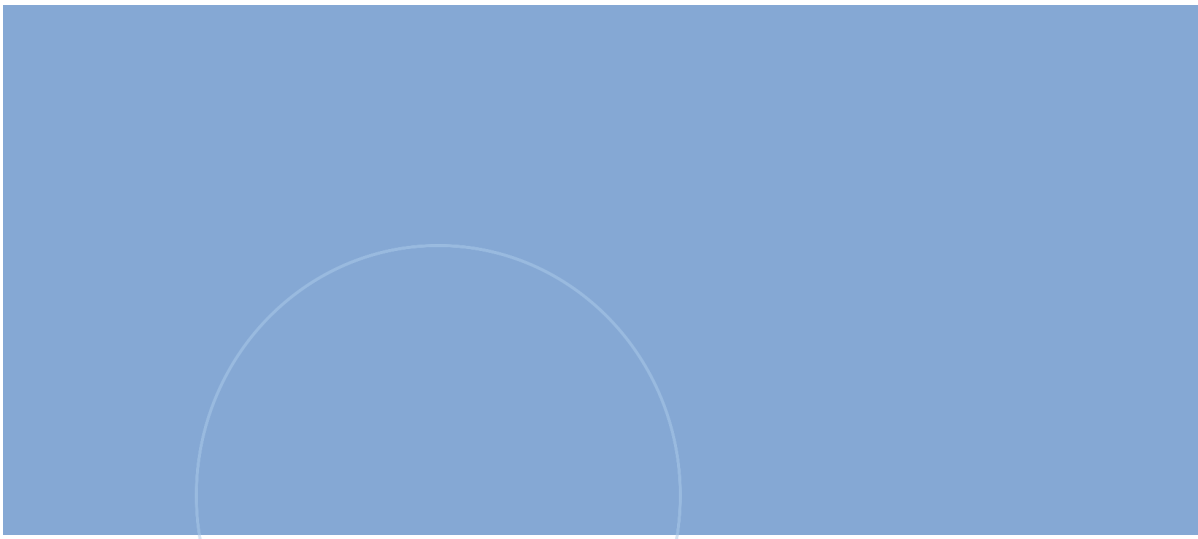

NTNU

Norwegian University of
Science and Technology